UNIVERSITY OF GENOVA

PHD PROGRAM IN BIOENGINEERING AND ROBOTICS

The BrightEyes-TTM: an open-source time-tagging module for fluorescence lifetime imaging microscopy applications

by

Alessandro Rossetta

Thesis submitted for the degree of *Doctor of Philosophy* (34° cycle)
December 2021

Prof. Alberto Diaspro	Supervisor
Dr. Giuseppe Vicidomini	Supervisor
Prof. Giorgio Cannata	Head of the PhD program

Thesis Jury:

Prof. Giulio Caracciolo, *University of La Sapienza, Rome*	External examiner
Dr. Per Niklas Hedde, *University of California, Irvine*	External examiner

Dibris

Department of Informatics, Bioengineering, Robotics and Systems Engineering

I would like to dedicate this thesis to my family and my loving wife.

Declaration

I hereby declare that except where specific reference is made to the work of others, the contents of this dissertation are original and have not been submitted in whole or in part for consideration for any other degree or qualification in this, or any other university. This dissertation is my own work and contains nothing which is the outcome of work done in collaboration with others, except as specified in the text and Acknowledgements. This dissertation contains fewer than 65,000 words including appendices, bibliography, footnotes, tables and equations and has fewer than 150 figures.

Alessandro Rossetta
April 2022

Acknowledgements

I would like to thank Dr. Giuseppe Vicidomini for the support and guidance he provided me during the last three years, and acknowledge Prof. Alberto Diaspro for giving me the wonderful possibility to work at the Italian Institute of Technology in Genoa. This Ph.D. experience helped me to grow both scientifically and professionally, the education I received definitely strengthened both my expertise and technical skills. I am deeply thankful to the the Molecular Microscopy and Spectroscopy group members who largely contributed to this project: Dr. Mattia Donato, Dr. Eli Slenders, Dr. Eleonora Perego, Dr. Giorgio Tortarolo and Dr. Sami Valtteri Koho. I am also extremely grateful to Dr. Marco Crepaldi and Dr. Francesco Diotalevi from the Electronic Design Lab for supporting and sharing the crucial expertise needed within the Ph.D research project. This three-years-long venture would have not been the same without my everyday work-lab collegues: Eleonora Uriati, Sabrina Zappone, Fabio Callegari, Andrea Bucci and Francesco Fersini. I would like also to thank to all the IIT - Nanoscopy and IIT - Electronic Design Laboratory members. Finally I would like to express my gratitute to Prof. Giorgio Cannata and the boards of Professors of DIBRIS department at Unige as well as Mrs. Valentina Scanarotti and Mrs. Roberta Usari.

Abstract

The aim of this Ph.D. work is to reason and show how an open-source multi-channel and standalone time-tagging device was developed, validated and used in combination with a new generation of single-photon array detectors to pursue super-resolved time-resolved fluorescence lifetime imaging measurements.

Within the compound of time-resolved fluorescence laser scanning microscopy (LSM) techniques, fluorescence lifetime imaging microscopy (FLIM) plays a relevant role in the life-sciences field, thanks to its ability of detecting functional changes within the cellular micro-environment. The recent advancements in photon detection technologies, such as the introduction of asynchronous read-out single-photon avalanche diode (SPAD) array detectors, allow to image a fluorescent sample with spatial resolution below the diffraction limit, at the same time, yield the possibility of accessing the single-photon information content allowing for time-resolved FLIM measurements. Thus, super-resolved FLIM experiments can be accomplished using SPAD array detectors in combination with pulsed laser sources and special data acquisition systems (DAQs), capable of handling a multiplicity of inputs and dealing with the single-photons readouts generated by SPAD array detectors.

Nowadays, the commercial market lacks a true standalone, multi-channel, single-board, time-tagging and affordable DAQ device specifically designed for super-resolved FLIM experiments. Moreover, in the scientific community, no-efforts have been placed yet in building a device that can compensate such absence. That is why, within this Ph.D. project, an open-source and low-cost device, the so-called BrightEyes-TTM (time tagging module), was developed and validated both for fluorescence lifetime and time-resolved measurements in general.

The BrightEyes-TTM belongs to a niche of DAQ devices called time-to-digital converters (TDCs). The field-gate programmable array (FPGA) technology was chosen for implementing the BrightEyes-TTM thanks to its reprogrammability and low cost features. The literature reports several different FPGA-based TDC architectures. Particularly, the differential delay-line TDC architecture turned out to be the most suitable for this Ph.D. project as it offers an optimal trade-off between temporal precision, temporal range, temporal

resolution, dead-time, linearity, and FPGA resources, which are all crucial characteristics for a TDC device. The goal of the project of pursuing a cost-effective and further-upgradable open-source time-tagging device was achieved as the BrigthEyes-TTM was developed and assembled using low-cost commercially available electronic development kits, thus allowing for the architecture to be easily reproduced. BrightEyes-TTM was deployed on a FPGA development board which was equipped with a USB 3.0 chip for communicating with a host-processing unit and a multi-input/output custom-built interface card for interconnecting the TTM with the outside world. Licence-free softwares were used for acquiring, reconstructing and analyzing the BrightEyes-TTM time-resolved data.

In order to characterize the BrightEyes-TTM performances and, at the same time, validate the developed multi-channel TDC architecture, the TTM was firstly tested on a bench and then integrated into a fluorescent LSM system. Yielding a 30 ps single-shot precision and linearity performances that allows to be employed for actual FLIM measurements, the BrightEyes-TTM, which also proved to acquire data from many channels in parallel, was ultimately used with a SPAD array detector to perform fluorescence imaging and spectroscopy on biological systems.

As output of the Ph.D. work, the BrightEyes-TTM was released on GitHub as a fully open-source project with two aims. The principal aim is to give to any microscopy and life science laboratory the possibility to implement and further develop single-photon-based time-resolved microscopy techniques. The second aim is to trigger the interest of the microscopy community, and establish the BrigthEyes-TTM as a new standard for single-photon FLSM and FLIM experiments.

Table of contents

List of figures

List of tables

Chapter 1

Introduction

In this introductory Chapter, I will first explain the truly motivations at the basis of this Ph.D. work, then I will provide to the readers the basic microscopy notions requested to understand the real and specific aims of this Ph.D. work.

1.1 Motivations

Fluorescence laser scanning microscopy (FLSM) is a powerful imaging tool for investigating both function and structure of biological systems (1). Indeed, FLSM not only provides sub-cellular spatial resolution, live-cell harmony, and molecular specificity and sensitivity, which are general properties of fluorescence microscopy, but also compatibility with many advanced microscopy techniques. For example, confocal and fluorescence lifetime microscopy, which are two of the most important FLSM synergistic combinations and which represent two topics of this Ph.D. work. Confocal microscopy provides optical sectioning, thus allowing three-dimensional imaging also in relatively thick samples. Fluorescence lifetime microscopy provides the possibility to investigate the functions of different sub-cellular structures and/or to understand their chemical environments.

However, current FLSM implementations suffer from a fundamental limitation: the way how they build an image inevitably lose a series of information encoded in the fluorescence signal. In the following, I will describe how the sample's image is typically formed in a fluorescent laser scanning microscope, and I will explain why this image formation process loses important sample information. In a conventional FLSM experiment, an objective lens focuses an excitation laser beam at a specific position in the sample plane, known as probing (or detection) region. Then, the same objective lens subsequently collects the emitted fluorescence and, together with a tube lens, projects the light onto the sensitive area of a

detector, which is generally constituted by a single element sensor, such as photo-multiplier tube (PMT). Indeed, while the microscope is able to produce an image of the probing region, the sensor integrates all the fluorescence light regardless its spatial distribution: in short, from a three-dimensional light intensity distribution $I(x',y',t)$, the detector generates only a temporal distribution $I(t)$. Successively, the signal is conventionally connected to a data-acquisition (DAQ) system, whose aim is to integrate the light intensity signal collected by the detector along the whole pixel-dwell time, i.e., the time that the microscope maintain stationary the probing region in a specific sample position (pixel). In short, from a temporal light intensity distribution $I(t)$, the DAQ generates a single intensity value I associated to a specific sample position (pixel). The probing region is usually raster-scanned across the sample with the use of a dedicated laser beam scanning device to form the final bi-dimensional (or three-dimensional) digital image. It is clear that, while the optical microscope is able to provide a spatiotemporal light intensity distribution for each specific position of the probing region across the sample, the way how the image is recorded completely cancels out all this information, producing only a single intensity value for probing region (pixel).

The recent introduction of new single-photon detector, such as the asynchronous read-out single-photon avalanche diode (SPAD) bi-dimensional array detector, first developed by our group (2), potentially allows for completely overcoming this limitation. Contrarily to a conventional single-element detector, a SPAD array is constitute of multiple element sensors distributed to sample a bi-dimension surface. Furthermore, each element is capable of giving as a output a single-photon readouts with a precision of few tens of picoseconds. These properties allow for imaging of the probing region of a fluorescence laser scanning microscope with, in principle, unlimited temporal resolution. In other words, this novel class of detector potentially give access to the spatiotemporal light intensity distribution $I(x',y',t)$ for each probing region in the sample. As example of the perspectives open by this novel detector is super-resolution fluorescence lifetime imaging. If a SPAD array detector is used in conjunction with (i) a pulsed laser source to excite the sample, and (ii) a special DAQ to acquire the SPAD array outputs in synchronization with the excitation events (i.e., the delay between the excitation pulse and the photon registration, the so called photon-arrival time), it is possible to implement sub-nanosecond time-resolved measurements. While the images of the single probing regions allows to reconstructed a super-resolution image of the sample, the sub-nanosecond time resolved measurement allows to assign to each pixel of the super-resolved image a fluorescence lifetime value. Another interesting perspectives are the combination of fluorescence fluctuation spectroscopy with fluorescence lifetime analysis: a

technique able to correlate the dynamics properties of a bio-molecule with information about its chemical environment or its structural changes.

However, all these perspectives risk being wasted if SPAD arrays detector are not combined with adequate and specialized DAQ systems, capable of time-resolving, harvesting and handling the high throughput of information generated by the single-photon detector arrays. From the point of view of the DAQ system, SPAD array detectors are made up by multiple element sensors of which the individual output needs to be acquired thus the DAQ system would require many input channels working in parallel. Although different commercial time-tagging devices are already present on the market, they can achieve multi-channel (> 20 input channels) capabilities only when inter-connecting several bulky electronic modules. The instrumentation market precisely lacks a true stand-alone single module DAQ that can all-together handle a multiplicity of input channel. Moreover, the commercially available time-resolved apparatuses implement general-purpose time-tagging functions which are not specifically conceived for fluorescence microscopy applications. In addition, these off-the-shelf instrument solutions focus their performances in yielding time resolutions as low as 1 ps which is admirable but out of the scope of fluorescence lifetime measurements in which a resolution of 100 ps would still perfectly work.

All-in-one solutions, with the DAQ system being integrated into the detector's body, were also developed (3; 4). Although being very compact, such type of solutions, lack flexibility in the sense that if, due to the constant technological progress, a new detector is developed also a new DAQ system will have to be physically re-engineered, to match the new detector's specs. Another important aspect to take into consideration is the fact that time-tagging DAQ devices belong to a niche of evolved/cutting-edge instrumentation and do not have the same price ranges of mass-consumed electronics, this aspect may inhibit the adoption and the widespread of time-tagging devices in FLSM limiting the potentiality of single-photon-based applications and techniques.

Indeed, if, on one hand, lot of investments and developing efforts are placed in fine-tuning the SPAD technology and more in general multi-element single-photon detector solutions, on the other, the lack of a user-customized and open-source DAQ system is felt in the microscopy and spectroscopy community.

In order to fill this gap and, at the same time, overcome the disadvantages/limitations of current DAQ system technology, within this 3-years-long PhD project an open-source multi-channel timetagging DAQ module (TTM) based on a field-programmable gate array (FPGA), that can temporally tag single-photon events as well as synchronisation events was engineered and developed. TTM's strength resides in being an open-source single-board

device that can handle multiple channels in parallel working in a stand-alone modality. The TTM is conceived to work as a passive plug-n-play device that can be connected to any type of detector and fluorescence microscopy setup with eventually minimal hardware modifications. The open-source feature confers TTM the primacy of being a fluorescence microscopy bespoke as well as a cost-effective solution that can be easily built and further upgraded, modified, and customized by the microscopy-makers.

I believe this TTM-DAQ module can unlock the real potential carried along with single-photon information and open up new research lines within FLSM-FLIM applications. TTM-DAQ project will give the possibility of pursuing state-of-the-art time-tagging measurement experiments in many labs and hopefully also establish, with no precedents, an open-source benchmark for time-resolved instrumentation.

1.2 Fluorescence laser scanning microscopy

Apart from its intrinsic morphology and spatial organization, the main and most measured properties of a sample are: optical reflectivity (5), light absorption and emission spectrum (6), light polarization (7) and fluorescence emission (8; 9). Amongst these, notably fluorescence plays a more prominent role. Firstly observed by Herschel in 1845 (10) and subsequently studied by Stokes, who coined the term fluorescence in 1852 (11), fluorescence is the emission of light by a molecule that has absorbed light as consequence of an external excitation process.The detection of fluorescence emission is widely used in the life sciences research world for both structural and functional analysis of biological material.

In FLSM, an object or a sample is scanned point by point by a focused laser beam. In this way, a spatial sampling of the object is performed and the final microscope image is reconstructed in a post-processing phase. The main components of a conventional FLSM setup are (i) a laser illumination source (ii) a scanning system and a (iii) light/photons detector. In a FLSM apparatus, the laser (i.e. the illumination source) is focused to a spot size meanwhile the scanning system allows for raster-scanning the laser light onto the sample and ultimately, the detector collects the back-scattered fluorescence light from the sample. In one of the most basic FLSM setup a single laser source is needed in combination with a single-element detector where the fluorescence light from each scanned location of the sample is registered by the the detector. Usually, optics component (lenses, mirrors and optical filters) are integrated in a FLSM setup in order to achieve higher object magnification, depth of focus and field of view (FOV) (12; 13; 14).

Worth mentioning is the fact that traditional FLSM came of age when new fluorescence laser scanning imaging systems have been developed to overcome some limitations connected with the FLSM techniques (15). For example, increased magnification and numerical aperture (NA) optics have been developed and employed for spatially-resolving the sample features in a more accurate way (16). And, most importantly, the use of a pinhole was also introduced in order to reject out-of-focus light, in respect to the imaging scanning plane, coming from the sample (CLSM) yielding images with higher contrast and resolution (17).

1.3 Fluorescence confocal laser scanning microscopy

In conventional FLSM setup the reconstructed image of the sample is affected by the blurring contribution coming from out-of-focus regions which reduce the contrast of the in-focus light broadening the system point-spread-function (PSF) and ultimately affecting the final image resolution (18). CLSM overcomes this problem by introducing a confocal aperture (such as a pinhole) in the emission beam path to reject the out of focus contribution (19) while also reducing the full-width at half-maximum (FWHM) PSF profile. Similarly to FLSM, in CLSM a point-like laser source is focused by an objective onto a sample. The spatial extension of the focus spot on the sample is determined by the wavelength (λ), the NA of the lens, and the quality of the image formation. Like in FLSM, the image spot is usually focused through the same lens onto a pinhole aperture and ultimately onto a single-element detector. The pinhole aperture is situated at a conjugate focal plane. Fundamentally, the principle used in a CLSM microscope, thanks to the introduction of the confocal aperture, allows to block the light coming from object planes above or below the image focus plane. Consequently, all out-of-focus optical background is removed from the image and the confocal image is an "optical section" of the sample (20).

CLSM turned out to be an indispensable technique for biomedical research being noninvasive, nondestructive and allowing for optical-sectioning of the sample. Furthermore, thanks to the improvements made in artificial fluorescence labelling technology (i.e. the capability of selectively attaching an artificially synthesized fluorophore to a specific biological molecule or structure) CLSM helped to solve a plethora of various and different biological problems (10; 21; 22; 23; 24; 25).

Spatial resolution is another important advantage of CLSM, as shrinking the optical pinhole aperture makes it possible to further reduce the spatial extension of the CLSM PSF by up to a factor of $\sim\sqrt{2}$ (26; 27) with respect to conventional diffraction-limited microscopy thus improving the system lateral-resolution (28). However, the reduction of the PSF does

not always lead to a resolution enhancement, because reducing the pinhole diameter also causes a heavy signal loss, and thus a decrease of the overall signal-to-noise ratio (SNR) (29).

New FLSM-based techniques, in which a squared-shape multi-element detector sensor was used, implemented a laser scanning methodology known as image scanning microscopy (ISM) (30) which overcame the SNR limitations of CLSM effectively obtaining the theoretically $\sqrt{2}$-fold resolution improvement predicted for CLSM without implying the use of a pinhole aperture. Yet, more recently, a new ISM approach based on a SPAD array detector was introduced (31).

1.4 Fluorescence image scanning microscopy

In a nutshell, ISM is a super-resolution microscopy technique that allows to overcome the diffraction barrier by a factor of $\sqrt{2}$ without reducing the overall image SNR. In ISM the single-element photo-detector is replaced by an imaging detector and the pinhole is removed so that each sub-element of the detector effectively acts as a virtual pinhole. This allows all the light to reach the image plane to be collected with a sub-Nyquist sampling (32). Similarly to CLSM, ISM requires an acquisition of the image of the excitation and detection region for each scanning position of the sample. The final ISM image is then obtained by computationally combining the information contained from all the acquired images i.e., after each scanning the microscope produces one confocal image for every element (pixel) of the detector array (33). As said, ISM cannot be accomplished using a single-element detector like photomultiplier tubes (PMTs) (34) or microchannel plates (MCPs) (35), which, so far, despite limitations like fragility, intrinsic deterioration with usage, high cost, bulkiness, and operation complexity, covered a major role in the field of FLSM and CLSM mainly because two advantages (i) large detection area and (ii) high measurement dynamic and spectral range (36; 37; 38).

Until today, ISM system configuration have been mainly implemented using conventional cameras, trading off a low imaging speed due to the limited camera frame rate (30; 39). Recently, the imaging speed limit was addressed by the Airyscan implementation, for which a 2D bundle of optical fibers is coupled to a linear array of GaAsP PMTs (40). However, this solution needs intercalated expensive and bulky electronics for sampling the fluorescence and shows some of the distinctive drawbacks of vacuum-based detectors like fragility and high cost.

De novo, a new kind of photo-detectors, known as SPAD detectors, are gaining ground in ISM applications thanks to their reliability, robustness, ease of operation, high detection efficiency, low timing jitter, and their integratability with read-out circuits, allowing for the development of multi-element arrays (2). The real advantage of SPAD sensors is their compatibility with microelectronic circuits, which allows the integration of dedicated electronics into the same silicon chip for creating mono- as well as bi-dimensional arrays of detectors which practically rules out the need for extra electronics. Moreover, their higher temporal resolution that allows for effectively implementing single-photon imagers with photon-timing capability (41).

However, both for CLSM and ISM, data derived from fluorescence intensity, can be affected by variations in laser excitation intensity, by fluorescent dye concentrations, by photobleaching (i.e. photochemical alteration of a fluorophore molecule such as it is permanently or transiently unable to fluoresce) and instrumental drift effects (focusing issues, detectors gain response, laser misalignment) (42). It is therefore difficult performing quantitative measurements relying only on the fluorescence intensity. Furthermore, it is nearly impossible to distinguish different fluorescent probes with very similar fluorescence spectra (43). In contrast to the limitations of fluorescence intensity another property of the emitted light that can be measured and from which it is possible to derive quantitative biochemical parameters of live cells and tissues, such as oxygen content (44; 45), pH (46; 47), metabolic state (48), viscosity (49), ion concentrations (50), temperature (51) is fluorescence lifetime.

Contrarily to the Airyscan approach, which still holds back the temporal information related to photon arrivals thus preventing the implementation of fluoreescence lifetime imaging microscopy (FLIM) (or similar techniques), SPAD array detectors, with single-photon (SP) asynchronous detection, and picosecond time-resolution ability and fully independent elements readout, are a very effective solution to overcome all the above mentioned limitations, and to implement newly ISM as well as FLIM methodologies.

1.5 Fluorescence lifetime imaging microscopy

Conventionally, fluorescence lifetime (τ_{fl}) is defined as the average time that a fluorophore, after being excited, remains in its excited state By measuring the fluorescence lifetime at different position in the sample (as per FLSM techniques) it is possible to build up images reflecting the spatial variations of the fluorescence lifetime. This method is called fluorescence lifetime imaging microscopy (FLIM) (52; 53). Unlike fluorescence intensity-based measurements, FLIM provides unique advantages as for example it is independent

of fluorophore concentration. FLIM measurements are also immune to light scattering effects that can potentially modify the detected fluorescence intensity. Moreover, FLIM is a self-referenced measurement (i.e., independent of absolute detected intensity), thus FLIM experiments do not require the throughput calibration steps that are needed for intensity based experiments. In addition, fluorescence lifetime is an absolute measurement that can be repeated across numerous device configurations after accounting for the instrument response function (IRF) of that device. Thus, artifacts caused by nonuniform illumination, which would greatly affect intensity measurements, are mitigated by measuring the lifetime.

For these reasons FLIM gained popularity in the bio-scientific community, thanks also to its high sensitivity to changes in molecular environment and molecular conformation of the sample (54; 55; 56). It has been used in autofluorescence molecular imaging (i.e. exploiting the fluorescence response of endogenous fluorophores) the to study cellular metabolism and is gaining momentum being used as a contrast mechanism to image live tissues allowing for fluorescence-guided surgery (57; 58). As well as with endogenous fluorophores, FLIM is also used in conjunction with exogenous fluorescent molecules that are for example capable of monitoring parameters (e.g temperature, ion concentrations, pH etc. etc.). Relying both on exogenous and endogenous fluorophores, FLIM is suitable for monitoring and direct measuring numerous biochemical processes in cells and tissues including also disease progression, drug delivery and vaccines efficacy (59; 60; 61).

Traditional continuous wave laser (CW) sources are not suitable for accomplishing FLIM measurements as continuously illuminating the sample does not allow for discriminating the difference in the change of state (excited vs. ground state) of the fluorophore over time Therefore, in a FLIM setup, optics and scanning components, have to be coupled with (i) pulsed laser sources (PW) for illuminating the sample and (ii) new types of light detection technologies such as avalanche-photodiode (APD)(62), SPAD (63), hybrid detectors (HyD) (64) and superconducting nano-wire detectors (65) which allow for individual (single) photons to be detected. Precisely for this reason, the SPAD array detector, thanks to its single-photons asynchronous readout capabilities, was used, in conjunction with a PW laser, for FLIM measurements, namely implementing super-resolution fluorescence lifetime image scanning microscopy (FLISM) technique (66).

1.5.1 Measuring fluorescence lifetime

With FLIM techniques it is possible to measure the fluorescence decay rate of a fluorophore which falls in the timescale of few picoseconds to hundred of nanoseconds. In order to

accomplish the measurement of such short time intervals LSM setups have to be coupled with PW laser sources, fast response SP detectors and fast DAQ cards able to assess and register the time of arrival of single photons. Talking about fast DAQ electronics card, FLIM measurements can be carried out using a time-domain (TD) (67; 68; 69) or a frequency-domain (FD) (70; 71; 72) (evolved thanks to (73) into digital-frequency-domain (DFD)) approach. State-of-the-art TD fluorescence lifetime measurements use a short laser pulse for exciting the fluorophore and then record, using time-resolved DAQ electronics, photon arrival times (time of flight - ToF) in respect to the excitation pulse. By sampling and collecting several photons together with their arrival time (time-tag), it is possible to build a photon arrival times histogram, known as time-correlated-single-photon-counting (TCSPC) histogram (74) (Fig. 1.1 b). TCSPC histogram is substantially a plot of the fluorescence decay curve (rate) over time: τ_{fl} can ultimately be calculated from the TCSPC histogram using either a fitting procedure (75) or the FLIM-phasor approach (76; 77). In a FLSM-FLIM system the TCSPC histogram is reconstructed as a function of the spatial coordinates (x,y) describing an image (Fig. 1.1 b). The final result of a FLIM measurement is an image in which the pixels are color-coded according to the bi-dimensional colormap that encodes fluorescence lifetime values as shown in Fig. 1.1 c.

On the other hand, DFD uses the same TD measuring setup (short pulses PW laser source and fast SP detectors) but, for DFD, single photons ToF is calculated using an heterodyne principle. In DFD electronics, a digital frequency (known as sampling frequency) that beats with the PW laser repetition frequency rate is generated and used to make a a digital counter (window counter) advance thus creating sliding time windows within the PW laser repetition period. As soon as a photon is detected, the value of the window counter is registered and used as ToF. Similarly to TD, in order to reconstruct the fluorescence decay curve, photons ToFs are used to build the TCSPC histogram (78; 79).

The TD-TCSPC approach is commonly used in LSM-FLIM biological applications as it combines high time resolution and high photon efficiency. In a TD-TCSPC-based FLIM architecture the sample is repeatedly scanned by an high repetition rate (up to 80MHz) PW laser beam, and a detector (or more than one) detects single photons of the fluorescence emission signal returning from the sample. Each detected photons is characterized by its time-tag (i.e. its time of arrival within the laser pulse period) and the coordinates of the laser spot in the scanning area in the moment of its detection. The image recording process creates a distribution of photon ToFs (i.e. the TCSPC histogram) for each of the scanned position: the acquisition results into a 3D image having pixels for the first two dimensions

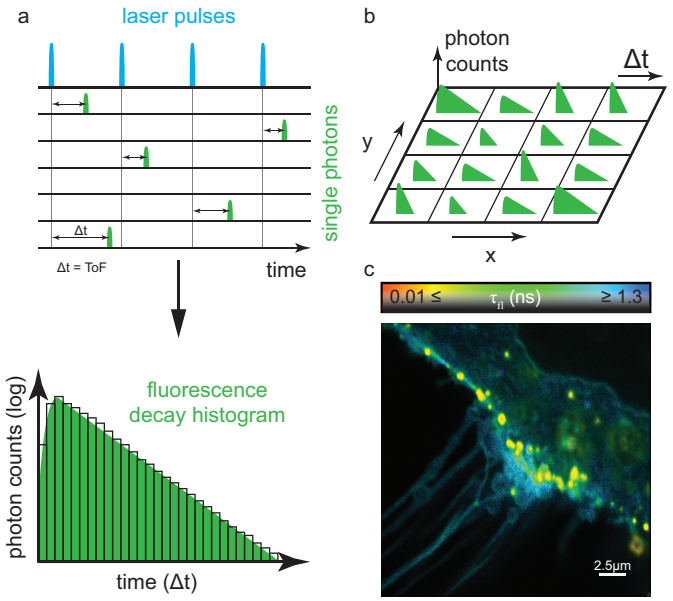

Figure 1.1 **TCSPC histogram and FLIM image**. **a** Principle behind photon arrival timing for TCSPC histogram reconstruction. After exciting the sample with a pulsed laser source and systematically registering the time of arrival of many fluorescence (single-)photons, a histogram, that represents the fluorescence decay is built up; **b** Basic principle of FLIM, where a fluorescence decay TCSPC histogram is reconstructed for every pixel of the image (x-y) leading to a 3D image $(x, y, \Delta t)$, where (x, y) are the spatial coordinates of the beam scanning system, and Δt is the dimension of the TCSPC histogram in each pixel; **c** example of a FLIM image: to each pixel corresponds a lifetime value which is color-coded according to the bi-dimensional colormap (top) and shown in the FLIM image (bottom). Scale bar 2.5 μm.

and containing TCSPC histograms for each pixels along the third dimension over a large number of time channels (80) (Fig. 1.1 b).

1.5.2 DFD-FLIM acquisition systems

The DFD approach is traditionally implemented in a FPGA chip. Within the FPGA, an electronic circuit is synthesized and used to sample and tag fluorescence single-photons. The DFD-FPGA circuit implements a heterodyne sampling architecture in which digital square sampling windows are used to time-gate the incoming photons and register their arrival times. The DFD methodology creates a low frequency replica of a fluorescence decay exploiting the digital time-gating heterodyne principle in combination with the periodicity of the PW laser source. The slow frequency replica is generated by a convolution between the fluorescence single-photon signals and the square digital sampling windows. Thanks to the heterodyne

principle the time-gating (photons sampling) can be accomplish with a $\sim$ 48 ps precision yielding phase-sampling performances comparable to a TD-TCSPC device. If on one hand DFD-FLIM systems are capable of real-time FLIM-phasor analysis and have high-precision phase measurement features, on the other they lack, so far, high temporal resolution ($\sim$ 1.5 ns (79)). The temporal resolution of the acquisition electronics impacts the overall instrument response function (IRF), the lower the temporal resolution the broader the IRF would be. Although a broad IRF is not a crucial parameter for fluorescence lifetime analysis as long as its shape and characteristics are known a priori - as explained in (81) -, TD-TCSPC devices are mostly preferred over DFD ones when dealing with FLIM measurements.

1.5.3 TD-TCSPC FLIM acquisition systems

The core of TCSPC devices is the electronics for the conversion of arrival times of photons into a digital data format. Commonly used TCSPC-FLIM devices implement either a time-to-amplitude-converter-analog-to-digital-converter (TAC-ADC) principle or a time-to-digital converter (TDC) principle (82). The TAC-ADC principle converts the ToF of each single-photon into the amplitude of an analog (voltage) signal and then into a digital data record (83; 84). TAC-ADC circuits are usually developed using application-specific integrated circuit (ASIC) technology. ASIC-based TAC-ADC deliver extremely high time-resolution (< 0.5 ps) and precision (~1 ps). Contrarily to TAC-ADC circuits, the TDC principle it is an all-digital measurement methodology that uses the delay in a chain/line of logic gates as a timing reference for assessing ToF time. The delay chain approach delivers a time resolution down to a few ps yielding measurement precision of tens of picoseconds (85). If TAC-ADC systems can only be implemented on ASICs, TDCs can actually be implemented on special electronics known as field-programmable-gate-array (FPGA) (86).

1.6 Aim of the work

In order to pursue time-resolved fluorescence lifetime-based measurements (and applications) making the most out of SPAD array detectors usage characteristics and performances (multi-element single-photon asynchronous readouts), in this PhD thesis work, I propose an open-source multi-channel time-resolved and standalone DAQ platform. This special DAQ module, named BrightEyes-TTM, is specifically designed to work as TD-TCSPC device implementing a delay chain-based digital TDC approach.

The BrightEyes-TTM can perform multiple photon- and reference-channels time-resolved samplings in order to implement current and future single-photon-LSM & FLIM techniques. The BrightEyes-TTM platform is based on a commercially available and low cost evaluation board, equipped with a state-of-the-art FPGA and a series of I/Os connectors. I/Os connections grant an easy interface of the BrightEyes-TTM board with a FLSM environment, the SPAD array detector and an host processing unit. The FPGA technology was chosen to grant both quick prototyping and versatility, and to meet the future requests from new SP-LSM applications. The current implementation was conceived and designed having in mind the fluorescence applications and the SPAD array detector characteristics, providing a good compromise between cost, photon-timing precision and resolution, temporal range, electronics dead-time and maximum photon-flux. Indeed, BrightEyes-TTM was engineered to operate as a single-board passive standalone platform for two main reasons (i) if in the future new type of the detectors will reach the market the BrightEyes-TTM can still be used, due to its versatility, by simple hooking some connection cables to them (ii) other commercially available time-tagging platforms, in order to achieve multi-channel capabilities, are made up by several bulky modules that need to be interconnected together impacting the ability of such systems to be easily accommodated and integrated in a lab environment. Additionally, the low FPGA resource needed by the current implementation ensures the highly scalability of the architecture, potentially enabling more channels and, in general, new applications.

Chapter 2

FPGA-based time-tagging architectures

The field programmable gate arrays (FPGAs) are semiconductor devices that are based around a matrix of configurable logic blocks (CLBs) connected via re-programmable interconnections. FPGAs can be reprogrammed to achieve and implement desired application or functionality requirements after manufacturing. Originally engineered for electronic devices prototyping, thanks to their low cost and reprogrammability, FPGAs are gaining active momentum and a relevant role in various industrial and research fields as primary used electronic components: fluorescence microscopy is one of those. Indeed, FPGAs are used in FLSM for handling many input channels in a parallel and for, due to the possibility of accessing low level basic silicon components (CLBs), measuring time intervals with picosecond precision by exploiting several configurable architectures known as time-to-digital converters (TDCs).

2.1 FPGAs

In recent years, the development of complex and compact high performance electronic controller systems has changed the world of very large scale integration and electronic design automation techniques (87; 88). The speed and re-programmable performances of new electronic components as well their flexibility for digital designs implementation have created new opportunities in terms of new applications and, consequently, opened up new markets. This is specially true for a specific hardware technology known as FPGAs. FPGAs combine low cost digital electronics development use of convenient software designing, programming tools and, an always growing, integration capability with external peripherals (89; 90; 91). The FPGA technology is being adopted in various fields of applications: from telecommunications (92), signal and image processing (93; 94), medical equipment (95; 96), robotics (97; 98; 99; 100) and machine learning (101; 102; 103). Yet, also in other application

fields FPGAs are revolutionizing the way digital signals are handled and processed. Indeed, focusing on LSM and FLIM applications, FPGAs have already been used with success for TD (104; 105; 106; 107) and DFD (73; 79) implementations. This is mainly because FPGA-based circuit implementation, thanks to their architecture scalability, can match current and future challenges of LSM and FLIM approaches.

FPGAs carry along many inherent advantages. First of all, low costs: FPGA design can be molded only on the specific needs of the application to implement shortening the time-to-market. Secondly, VLSI design coupled with FPGAs, allows also for analog interface on FPGAs, thanks to the use of system-on-a-chip (Soc) (108). FPGA-SoC integrates analog and digital capabilities on the same silicon chip, yielding an high application versatility (109; 110). Lastly, thanks to FPGAs parallel architecture computation abilities, tasks execution time is drastically reduced allowing FPGA-based designs to reach speed-performances of analog devices but without their downsides: lack of flexibility, as analog circuits cannot be reprogrammed, and performance drifts due to intrinsic nature of analog signals (111). FPGAs can be included in the wide family of programmable and re-programmable digital-logic components (112).

2.1.1 FPGA system architecture

An FPGA consists of a matrix of customisable logic blocks linked to each other via an interconnection network which is completely reprogrammable. The configuration of the logic blocks and the arrangement of the interconnections, which determine the actual and overall FPGA circuit functionalities, are controlled by memory cells. Several configurable memory technologies exist, the most flexible and used one is the static random access memory (SRAM)-based FPGA technology (113; 114; 115).

The generic architecture of an FPGA, shown in Fig.2.1, is composed of a mosaic of configurable general purpose logic blocks (CLBs). CLBs can be considered as the basic brick of the FPGA. A CLB consists of a look-up table (LUT), which can be configured either as memory element or a combinatorial mathematical function. A carry look-ahead data (CARRY chain) path is also included in a CLB. The CARRY element can be used to build efficient arithmetic operators or it can be used to create controlled-delay paths within the FPGA fabric. Lastly, a D-type flip-flop (DFF), with all its control inputs (synchronous or asynchronous set/reset, enable), allows for correctly registering the output of the logic cell (Fig. 2.2). The CLBs architecture corresponds to the fundamental unit of an FPGA, and it can be seen as a small digital control and processing unit since the registered output

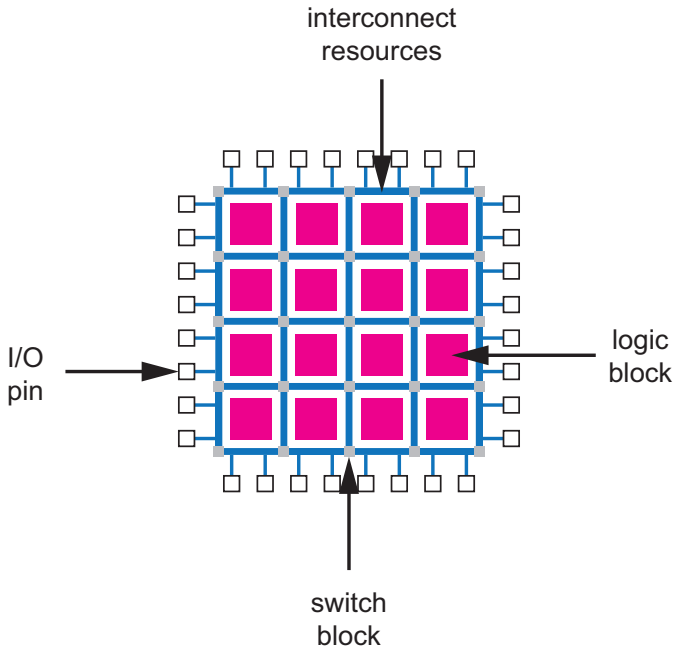

Figure 2.1 **FPGA architecture** I/O pins are used to interface and connect the FPGA with the outer world; the intimate structure of and FPGA is constituted by a mosaic of logic blocks connected with each other via the interconnect resources routed amongst the different logic blocks using switch blocks. A switch block is a routing unit that can couple and connect the interconnect resources.

can be configured as an input of the same CLB. Zooming out from the FPGA architecture: CLBs are surrounded by a ring of configurable input/output pins (IOBs). Modern FPGAs can reach >1000 user IOBs thus yielding the capability of handling multiple I/Os at the same time. CLBs and IOBs communicate each other through a (re)-programmable interconnection network. The way the interconnection network is programmed i.e. the way CLBs and IOBs work together, creates a digital circuit design specifically dedicated to accomplish tasks for a determined end-application (116; 117; 118).

Nowadays Xilinx Inc. (San Jose, CA, United States) and other FPGA manufacture companies have introduced inside this logic blocks mosaic architecture some dedicated and specialized components such as random access memories (RAM), digital signal processing (DSP) accelerators (119; 120), high-speed clock management circuitry (PLL, MCMM) (121), serial transceivers (SerDes) (122), embedded hard processor cores such as ARM (Xilinx UltraScale FPGA family devices) and soft processor cores such as the Microblaze (123; 124) in order to boost FPGAs performances and potentialities. The high performance, together with the lower costs and relatively small time-to-market, turns FPGA-based architectures alluring for TDC implementations within TD-TCSPC applications. FPGA-based TDC,

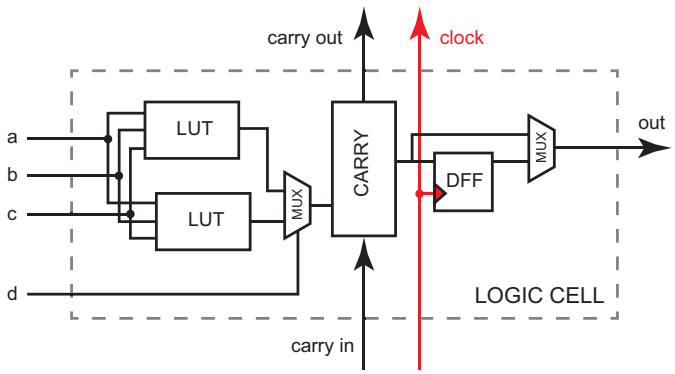

Figure 2.2 **FPGA logic cell structure**

being unconstrained by ASICs downsides, can fully exploits circuit scalability and re-programmability allowing for circuit designs to evolve and adapt over time (125; 126; 127; 128).

2.2 FPGA-based TDCs

In the last two decades, FPGA technology has demonstrated massive improvements, from a technical fabrication perspective to a strengthening and usability of development tools. This rapid growth in performances and capabilities allowed FPGA to close the gap, with ASIC circuits, transforming FPGA-based systems into a no longer prototype-only architectures (129; 130; 131). That is mainly why FPGA have been used also to measure *time* intervals with sub-nanosecond precision, exploiting a specific type of design architectures known as time-to-digital-converters. In the context of FLSM and FLIM applications, FPGA-based TDCs, which recently reached time resolutions of ~10 ps (132) (which is more than precise enough when dealing with τ_{fl} measurements) are getting to the same level as ASICs (133; 134; 135; 136). Moreover, the continuously-increasing number of CLBs available in FPGAs also contributed to the development of multi-channel and sophisticated TDC architectures. Indeed the literature of FPGA-based TDCs is full of different and various approaches, each one characterized by a unique circuit design implementation strategy in order to achieve finer time-resolutions and higher sampling-rates (137; 138; 139). That is also why a homogeneous TDC architecture categorization is hard to draft. Machado et al. (140) proposed a standardized taxonomy for classifying FPGA-based TDC architectures (Fig.2.3). Such taxonomy, was conceived considering the main circuit architecture involved in the overall system design.

From a literature analysis the most used and developed FPGA-based TDC configurations are based on tapped-delay-lines (TDLs) (141; 142). In the next sections the main and most

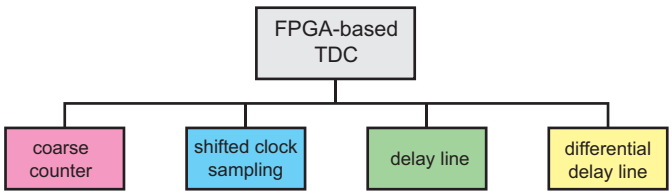

Figure 2.3 **FPGA-based TDC taxonomy**. The main and most used FPGA-based TDC types are the coarse counter approach, the shiftef clock sampling technqie, the delay line method and the differential-delay line architecture.

used FPGA-based TDC architectures, shown in Fig. 2.3 are described putting more accent on TDC-TDLs systems (86; 143).

2.2.1 Coarse counter TDC

The coarse counter is the simplest FPGA-based TDC architecture that can be implemented. The core element is a digital counter that increments its value at a speed which depends on the clock frequency the counter gets supplied with (Fig. 2.4). The frequency value sets consequently the time resolution of the TDC architecture design. With the progress in FPGA development, the maximum operating frequency of a chip has increased reaching hundreds of MHz. Xilinx datasheets report a maximum working limit frequency of ~800 MHz system clock yielding time resolutions as low as ~1.25 ns. In order to achieve resolution below hundreds of picoseconds, a system clock frequency higher than 10GHz is required: at present day, unfortunately, FPGAs are still not feasible for generating such high frequencies, but, other techniques could be used to achieve $<$ 1 ns such as the shifted-clock-sampling architecture (144; 145).

2.2.2 Shifted clock sampling TDC

Another TDC approach that can be pursued using FPGA platforms is the shifted-clock-sampling SCS-TDC (a.k.a. phase detection TDC). Similarly to the coarse counter approach, also starting from an FPGA clock frequency, a SCS-TDC architecture uses intrinsic functions of PLL (phase-locked-loop) & MCMM (mixed-mode clock manager) logic blocks to create multiple replicas of the same input clock signal but having different phase shifts (146; 147; 148; 149; 150). This mechanism ultimately creates a sub-clock-period-short time-windows allowing for sampling the input signal (i.e. the single-photon signals) with a finer resolution with respect to the period of the clock used (Fig. 2.5). Specifically, for a SCS-TDC the time resolution t is equal to:

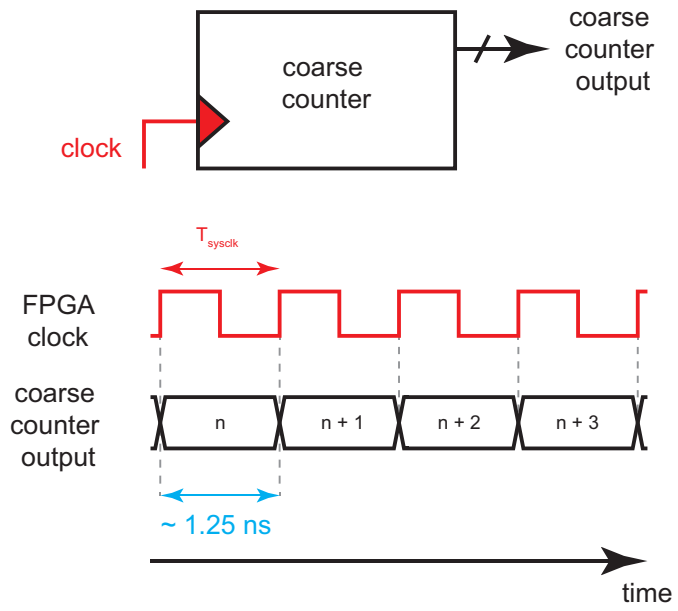

Figure 2.4 **Coarse counter TDC**. Schematic representation of a coarse counter TDC receiving as input a FPGA system clock and returning as output, a digital integer values (top); working principle of a coarse digital counter: at every *rising edge* of the FPGA system clock the counter increments its value over time. Given the actual FPGA technology the maximum operating frequency is around 800MHz yielding a time resolution of about ~1.25 ns (bottom).

$$t = \frac{T_{\text{clk}}}{N_{\text{phases}}} \tag{2.1}$$

where T_{clk} is the period of the clock used in the design and N_{phases} is the number of phase shifts generated by the clock-manager components. SCS-TDC architectures, apart from being of easy implementation, offer great system linearity while being able to achieve resolutions as low as hundreds of ps (151; 152; 153). The main drawback of SCS-TDCs, when compared to other architectures such as delay-line approaches, remains its limited resolution.

2.2.3 Delay line TDC

A delay-line TDC, also called flash TDC or tapped-delay-line TDL-TDC is the most popular FPGA-based TDC architecture because of its simplicity, low latency, reliability and high-temporal resolution (154; 155; 156; 157; 158; 159; 160; 161; 162; 163; 164; 165; 166; 167; 168; 169; 170; 171; 172; 173; 174; 175; 176; 177; 178; 179; 180; 181; 182; 183; 184; 185). The core constituent of a TDL-TDC module is a tapped delay line (TDL) The TDL is made

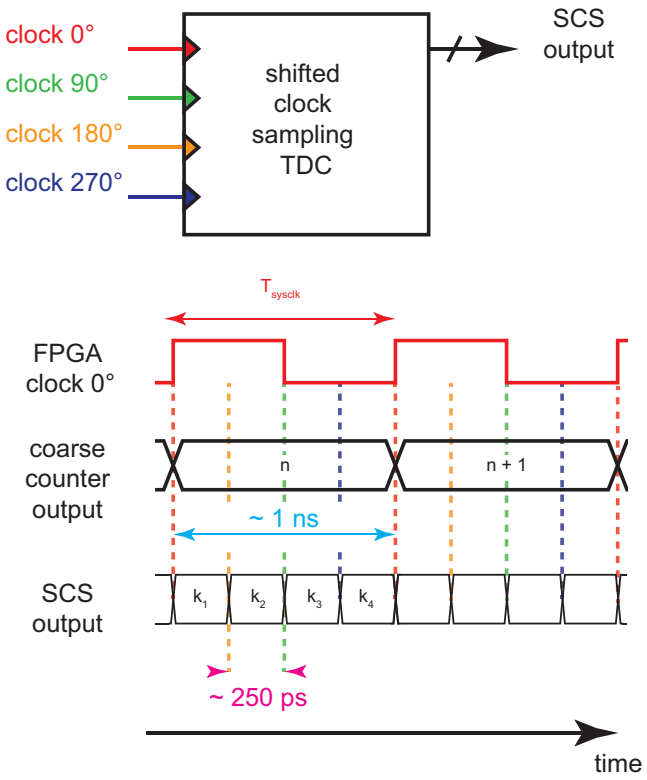

Figure 2.5 **SCS-TDC**. Schematic representation of a coarse counter TDC receiving as input an # 4 shifted FPGA system clocks an returning as output sub-clock-resolved values (top); working principle of an SCS-TDC: the FPGA system clock 0°period is sub-divided in $N_{\text{phases}} = 4$ time intervals ($k_{1\text{-}4}$) exploiting the different phases of the other input clocks (90°, 180°, 270°). Every k_{i} can have a time resolution as low as hundreds of ps (bottom).

up by a series of small delay elements joined in a chain architecture and is used to delay an input signal (usually called START signal i.e. the signal from which the ToF is measured) with respect to a reference-sampling signal (usually called STOP signal i.e. the signal used as a time-reference for measuring the ToF). From the delay characteristics of each delay element, it is possible to match the distance covered by the START signal along the delay line with a specific arrival time (time-tag) with respect to the FPGA clock signal (186; 187). When implementing a TDL on a FPGA, a specific CLB element known as CARRY is used as a fundamental delay block to build the tapped delay line. A TDL is indeed assembled by interconnecting multiple CARRY elements of different logic cells. In a flash TDC, the output of each delay block gets then connected to the CLB flip-flop (DFF) component (Fig. 2.6 top pane). The DFF can retain either a boolean '0' or '1' depending on the digital-data input value.

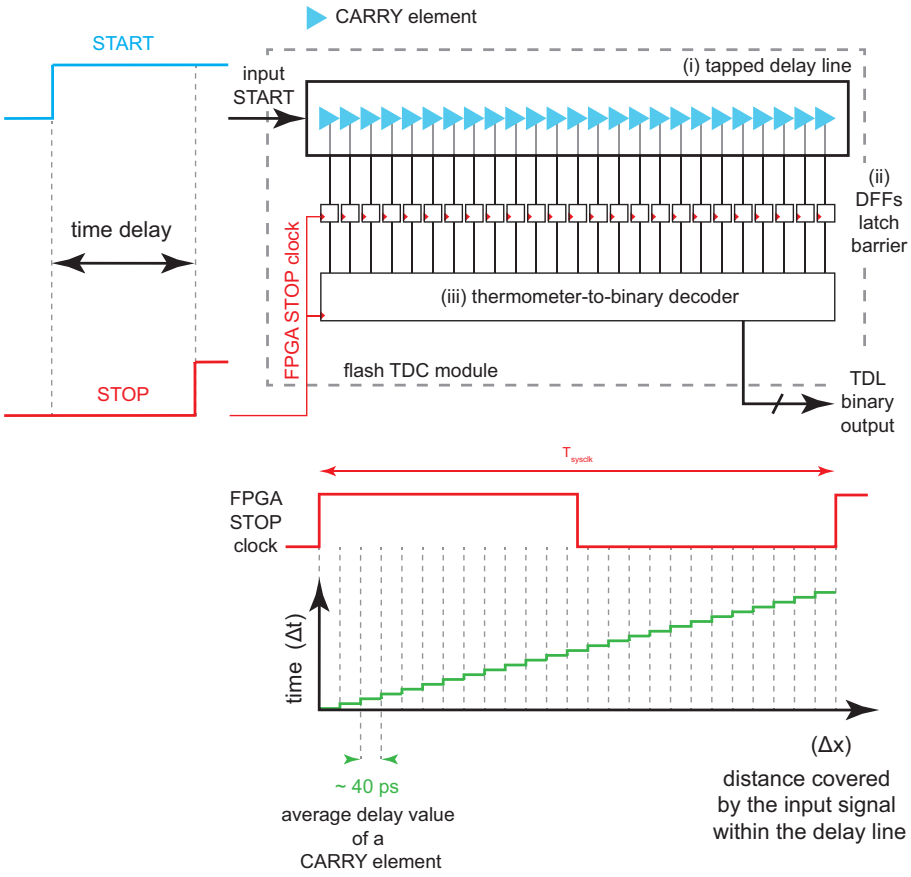

Figure 2.6 **TDL-TDC**. Schematic representation of a delay line TDC constituted by (i) a tapped-delay line, (ii) a DFFs latch barrier and (iii) thermometer-to-binary encoder (top); working principle of an TDL-TDC: the input signal propagates along the TDL until reading event occurs. By knowing the reciprocal relationship between the CARRY delay value and the distance the input signal covered before the STOP event occurred, it is possible to convert the digital measurement of the travelled distance into a time measurement (bottom).

Working principle

Assuming that the START signal holds a boolean '0' (false) at the steady state and '1' (true) after a triggering event (such as the arrival of a single-photon), then the digital-logic high value '1' will propagate through each of the tapped delay line elements. Consequently, the data input of each DFF (bit_n) will also change from '0' to '1'. The START signal continues to propagate freely along the TDL until a reading event occurs. This TDL reading event, known as STOP event, freezes the values of the DFFs barrier connected to the TDL elements giving out a digital reading of how far the START signal travelled along the TDL in respect to the STOP signal (start-stop time). Knowing the reciprocal relation between the CARRY delay value and by counting the number of '1's, it is possible to convert the distance the

START signal covered before the STOP event occurred into a time measurement (188) (Fig. 2.6 bottom pane).

Limitations

TDL-TDCs yield a higher time-resolution when compared to coarse counter and SCS TDCs, but, on the other hand, lack linearity due to the intrinsic and ineradicable irregularities in the FPGA fabric. TDL-TDC nonlinearities are mainly due to: (i) different values of the delay elements used in the TDL have values that greatly differ from each other (ii) the extension of the interconnections amongst the different delay blocks which jeopardize the consistency of the connection path delay (189) (Fig. 2.7). The former effect profoundly interferes with delay-time conversion causing a non-linear TDL-TDC response. The irregularities can be categorised in two groups:

- Ultra-wide time bins (UWB): mainly caused by the TDL crossing adjacent clock regions of the FPGA resulting in a long interconnection path between two consecutive CARRY blocks. This type of alteration corresponds to a longer delay value in the delay line.
- Zero-length time bins (ZLB): caused by the presence of CARRY elements which delay value is negligible.

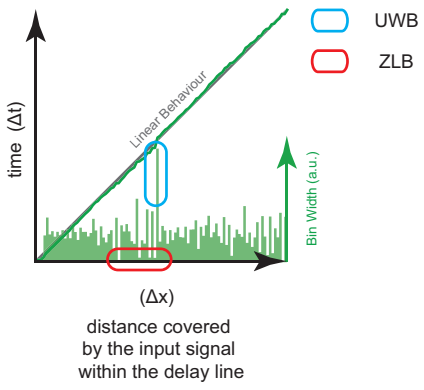

Figure 2.7 **Limitations of the TDL-TDC architecture**. The delay elements used in a TDL have values that greatly differs one to another, moreover the interconnections amongst the different delay blocks extend across adjacent clock regions of the FPGA jeopardizing the consistency of the connection path delay and leading to an uneven time-delay representation which is affected by UWBs and ZLBs.

Another documented issue when working with FPGA-based TDLs is referred as the bit-bubbles implementation problem. Bit-bubbles arises in the TDL readouts due to a non-deterministic sub-shift of the sub-CARRY element output contributions. To compensate for bit-bubbles more FPGA resources need to be deployed yet increasing the overall logic occupancy (190; 191).

The wave union approach

To overcome the TDL-TDC linearity limitations, without increasing the number of delay lines, the Wave-Union (WU) method was proposed by Wu (192). When using WU launchers approach, multiple '0'/'1' transitions per START signal are generated in the TDL input stage. The measurement of these multiple transitions reduces the non-linearities in the delay line, improving the overall TDC's performance. Despite high-time resolutions, linearity does not improve enough to allow the usage of WU-TDCs in LSM-FLIM contexts.

2.2.4 Differential delay-line TDC

Differential delay-line TDC architectures, also known as sliding-scale technique TDC or Nutt method TDC, are based on calculating the ToF using two delay-line structures in combination with a coarse digital counter (193; 194; 195). Such system solves all the linearity problems strictly connected with the TDL-TDC approach, yet yielding same time-resolutions performances. When dealing with FPGA-based TDCs, together with system linearity and time resolution another parameter to take into account is the FPGA resource usage: the differential delay-line approach offers a good compromise between linearity, temporal resolution as well as FPGA-CLBs resource usage.

Working principle

In order to assess the start-stop time, the differential delay-line architecture uses two flash TDC modules (TDL-TDC), one for measuring the ToF of the START signal, and the second one for assessing the time of arrival of the STOP-reference signal. Both the ToFs for the START and the STOP signals are measured in respect to an internal FPGA system clock. These two TDL-TDCs are deployed in the FPGA together with a coarse free-running digital counter for grating the differential delay-line a wider time measuring range (Fig. 2.8).

The key feature of this technique is that the flash TDC readouts and the coarse counter are synchronous with the FPGA internal reference clock, which is totally uncorrelated (asynchronous) with respect to the arrival times of both the START and the STOP signals.

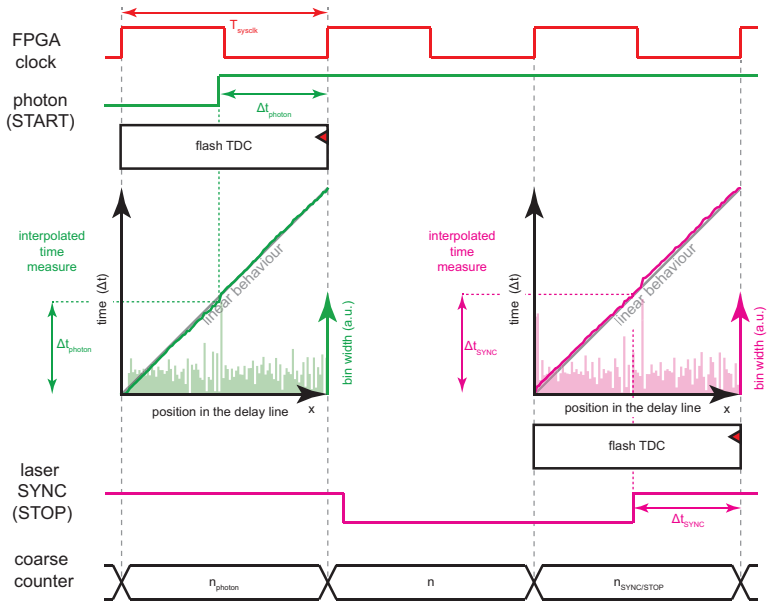

Figure 2.8 **Schematic of the sliding scale technique working principle**. START (photon) arrival time ($\Delta t_{\text{photon}}(ch)$) is computed with respect to the rising-edge of the FPGA clock (top) thanks to a dedicated flash-TDC module of which the time response and the tapped-delay-line bin widths are shown as a function of the bin number (left-middle). As soon as START is detected also the value $n_{\text{photon}}(ch)$ of the coarse counter gets registered (bottom). The STOP (laser sync) arrival time (Δt_{SYNC}) is also recorded on its the dedicated flash-TDC module (time response and bin-widths are show in the right-bottom portion) with respect to the FPGA clock together with the corresponding value of the coarse counter n_{SYNC} (bottom). $\Delta t_{\text{photon}}(ch)$, $n_{\text{photon}}(ch)$ and Δt_{SYNC}, n_{SYNC} are used to compute $\Delta t(ch)$ start-stop time according to Eq. 2.2.

The sliding-scale technique can thus be defined as an asynchronous design (185; 193; 196) where the Δt (start-stop time) gets always measured using different regions of the TDL-TDCs, thus smoothing-out the intrinsic FPGA-fabric non-linearity. Using the sliding scale approach, identical time intervals will therefore yield slightly different TDL-TDC responses averaging out the non-linearities over multiple observations (Fig. 2.9).

Measuring start-stop time Δt

In the sliding scale technique, instead of using a single flash TDC in which the delays between the STARTs and STOP signals are directly measured, two independent tapped-delay line (flash TDC) modules are used in combination with a coarse counter. One flash TDC measures Δt_{photon}, i.e., the arrival time of the photon (START) with respect to an internal FPGA reference clock. The second TDC measures Δt_{SYNC}, i.e., the delay of the laser sync

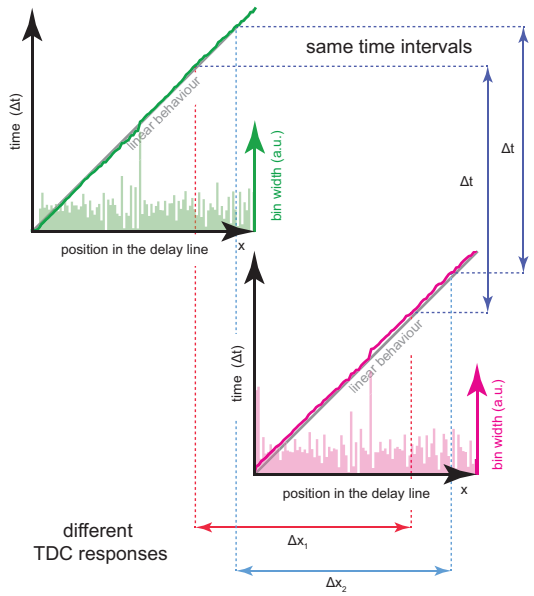

Figure 2.9 **Linearity improvement principle in a differential delay-line TDC**. Because of the START (photon) and STOP (laser sync) signals are asynchronous with respect to the FPGA clock, the same start-stop time interval Δt, is measured at different positions in the flash TDC modules resulting in an improvement of the TDC linear response.

(STOP) with respect to the same FPGA reference clock (Fig. 2.8). The coarse counter is needed to calculate the time difference (Δt) between the photon and the laser pulse, Eq. 2.2:

$$\Delta t = \underbrace{[n_{\text{SYNC}} \cdot \mathscr{T}_{\text{sysclk}} - \Delta t_{\text{SYNC}}]}_{t_{\text{SYNC}}} - \underbrace{[n_{\text{photon}} \cdot \mathscr{T}_{\text{sysclk}} - \Delta t_{\text{photon}}]}_{t_{\text{photon}}} \tag{2.2}$$

Where:

- $n_{\text{photon}}(ch)$ is the number of FPGA clock cycle between the beginning of the experiment and the photon signal. When reported, ch denotes the photon channel.
- n_{SYNC} is the number of FPGA clock cycle between the beginning of the experiment and the laser SYNC signal.
- Δt_{SYNC} is calibrated temporal value representing the time elapsed from the STOP signal, i.e., the laser SYNC signal, and the next active edge of the free-running coarse counter (FPGA clock).
- Δt_{photon} is calibrated temporal value representing the time elapsed from the START signal, i.e., the photon signal, and the next active edge of the free-running coarse counter (FPGA clock).

- $\mathscr{T}_{\text{sysclk}}$ is the period of the FPGA system clock.
- $t_{\text{photon}}(ch)$ is absolute time from the beginning of the experiment for the photon signal with, in principle, picosecond precision.
- t_{SYNC} is absolute time from the beginning of the experiment for the SYNC signal with, in principle, picosecond precision.

The coarse counter also extends the time range of the differential TDL-TDC architecture as Δt_{photon} and Δt_{SYNC} can be measured even if they are tens of microseconds apart.

2.3 Thermometer to binary converter

The digital ToF readout for SCS-TDCs, TDL-TDCs as well as differential TDCs constist of a series of 'ones' and 'zeros' that ultimately have to be converted into a binary value data format for a more efficient representation. Thus, a dedicated circuit is needed to interpret and decode the TDLs and SCSs data. ToF digital readouts are elaborated using a thermometer-to-binary converter (T2B) digital circuit (197; 198; 199). The T2B accepts an array of n-bits as input and returns a binary number that represents how many 'ones' are present in the input latched data. The T2B data conversion (compression) simplifies the handling of TDCs readout, allowing for a more effective data registration in terms of memory resources utilisation (164; 191)(Table 2.1).

Table 2.1 **Thermometer to binary encoder**. The t2b translates the tapped-delay-line readings into a binary form; TDL readings are converted into binary number for a more compact and efficient data representation.

Tapped delay line output	Binary code
0000000	000
0000001	001
0000011	010
0000111	011
0001111	100
0011111	101
0111111	110
1111111	111

2.4 Calibration of a TDC readouts

Although time-resolution is an important parameter to take into account, also TDC linear response has to be characterized (shown in Appendix A) and adjusted to improve the system ultimate precision, thus a time-calibration of TDC readouts is necessary. TDC calibration mechanisms are often required on modern FPGAs. The main techniques used are bin size decimation and bin-by-bin calibration. The aim of a calibration procedure is taking into account the non-linearities of the system in order of being able to correctly estimete the ToFs. The final goal of the calibration process is to assess the actual entity of the systems non-linearities aiming to smooth them out.

2.4.1 Bin size decimation

In bin decimation, the linearity of the TDL can be greatly improved at the cost of time-resolution. This solution also achieves good results when multiple TDL are used, as it does not increase the hardware resources utilization. The principle is based on building larger delay blocks by grouping together several delay elements. This enables the achievement of time-bins with more uniform sizes, increasing the linearity of the chain (165; 166).

2.4.2 Bin-by-bin calibration

Bin-by-bin calibration technique does not have the drawback of reducing the TDL resolution and is more suitable for TDCs with higher linearity and resolution requirements. Since the bin widths (i.e. the delay element values of the tapped delay line) are not all equal due to intrinsic FPGA fabric irregularities, a photon or sync hit is more likely to fall into a wider bin (UWB) than into a narrower bin (ZLB) (192). In order to calibrate the time response of the TTM, the histograms of the photon counts as a function of the arrival bin of each deployed TDL module are used. After having collected a large number of START or STOP events from a measurement, the cumulative event count in each bin is proportional to its width. For example, if a total of N hits are accumulated into the histogram (Fig. 2.10 a), assuming these hits are evenly spread over $\sim$ 4.2 ns, which is the period of the 240 MHz FPGA clock driving the flash TDC, then the width of an N_{i}-count bin is $w_{\mathrm{i}} = N_{\mathrm{i}}{*}(4200ps)/(N)$ (Fig. 2.10 b) (193; 200; 201; 202). In the bin-by-bin calibration procedure, the widths w_{i} of all tapped delay line CARRY elements are measured and stored in an array w_{k}, then the calibrated time responses $_{\mathrm{i}}$, corresponding to the center of i-th bin, can be calculated according to Eq. 2.3 below (203; 204):

$$\Delta t_{\mathrm{i}} = \frac{w_i}{2} + \sum_{k=0}^{i-1} w_k \tag{2.3}$$

In this way, all the different $_{\mathrm{i}}$ time contributions of all the flash TDC module delay elements, can be assessed and used to correctly time-tag both the photons ($\mathrm{START_n}$) and the laser sync line (STOP).

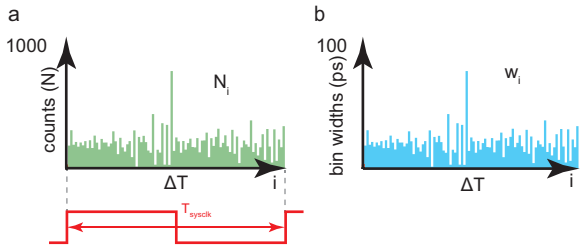

Figure 2.10 **Fundamental steps of the bin-by-bin calibration procedure**. **a** tapped-delay-line histogram of received counts as a function of the arrival tap (delay) number. The range of the maximum arrival tap number depends on the reference FPGA clock period $\mathscr{T}_{\mathrm{sysclk}}$: the tapped-delay-line is dimensioned to have a total delay value of $\mathscr{T}_{\mathrm{sysclk}}$. **b** individual value $\mathrm{w_i}$ of each delay element is estimated (bin time-widths).

In a differential-TDC architecture, in order to further save up on FPGA resources, the calculations and time conversions for computing Δt, $\Delta t_{\mathrm{photon}}$ and Δt_{SYNC} are usually accomplished on a host computing unit in a post-processing phase. Here, the flash-TDC readings and the registered coarse counter values are merged for each channel to reconstruct the history of each photon (see Chapter 4 for data processing).

2.5 Conclusions on FPGA-based TDCs

Within the FPGA-based TDC, the literature reports several different architectures. Each architecture offers a compromise between different specifications. Particularly, the differential delay-line TDC architecture turned out to be the most suitable for this PhD thesis project as it offers an optimal trade-off between temporal precision, temporal range, temporal resolution, dead-time, linearity, and FPGA resources.

Chapter 3

Implementing the BrightEyes-TTM

Amongst the various FPGA-based TDC approaches presented in Chapter 2 the differential delay-line TDC architecture was chosen to be the most suitable for implementing the BrightEyes-TTM project. Differential delay-line TDCs mainly offer a good compromise between time-resolution, system linearity and FPGA resource usages. Thus, differential delay-line TDCs fully match the aim of the project in implementing a time-tagging module capable of operating many independent channels at the same time and, more importantly, on the same FPGA chip.

3.1 Choosing the FPGA platform

BrightEyes-TTM was conceived to work and operate as a standalone DAQ module. In order to enforce the open-accessibility features of the project, BrigthEyes-TTM was implemented on a commercially (worldwide)-available Kintex-7 FPGA evaluation board (KC705 Evaluation Board, Xilinx Inc., San Jose, CA, USA) (Fig. 3.1). Xilinx Kintex-7 FPGA family was chosen over other FPGA chip families (such as the UltraScale and UltraScale+ families) as many of the literature works and projects about implementing FPGA-based TDCs used a family-7 device (150; 153; 180; 200; 203) because of family-7 is one of the most advanced FPGA technology and yet fully documented chip category in terms of CLB primitives and technical application notes (especially for the *bit-bubbles* issue). The KC705 evaluation board was chosen because is a general purpose electronic card having, beyond the mere FPGA chip, a series of built–in peripherals hardware components (e.g., PCI-E and UART serial connectors, FMC expansion connectors, and RAM memories). Precisely, the different serial connectors, when streaming the data out from the FPGA, potentially allow for different data-transfer configurations and speeds, and the I/Os serial expansion connectors allow full compatibility

and interface ability of the evaluation card with the outer world of LSM-FLIM hardware components (PW laser sources, scanning mechanisms and SP-detectors).

Figure 3.1 **KC705 Evaluation Board**.

3.2 Multi-channel time-tagging architecture

The BrightEyes-TTM implements a hybrid structure in which differential TDLs are coupled with coarse counter TDCs. Such system architecture was designed to operate as TD-TCSPC device, working (within LSM-FLIM setups environment) in a time-tagging mode (Fig. 3.2) and thus allowing for the registration of individual events as well as their temporal signature (time-tag). The time-tagging operation mode can resolve and measure different types of time-intervals such as the absolute time of arrival of a photon event, laser sync or REF signal in respect to the beginning of the measurement and, consequently, the (start-stop) time-interval between a photon and a laser sync event (Fig. 3.2). Indeed, the developed TTM architecture is capable to time-tag three different categories of events:

- The single-photon event, i.e., photons recorded by the detection system which delivers an digital signal to the TDC module.
- The sync laser event, i.e., the synchronisation signal delivered by a PW laser source.
- The reference event, i.e., a signal generated by another component of the experimental setup (e.g., sample scanning systems, actuators or laser modulators).

Each category of the fore-mentioned events is recorded with different time resolutions: the absolute ToF timings for the photon (t_{photon}) as well as for the PW laser synchronisation events (t_{SYNC}) have a resolution of ~ 30 ps as they are registered using fast TDLs working

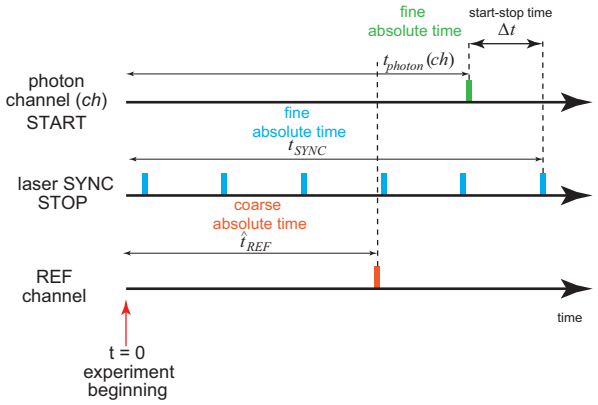

Figure 3.2 **Time-Tagging Principle**. The time-tagging mode allows recording individual events and labelling each one of them with a temporal signature. Typically, this temporal signature denotes the delay time of the events in respect to the beginning of the experiment (absolute time). The BrightEyes-TTM module is able to tag three different classes of events: The photon events, i.e., a photon is registered by the detector which delivers a digital signal to the module; the sync laser events, i.e., the synchronisation signal delivered by the pulsed laser; the reference events, i.e., a signal generated by another component of the experimental setup (e.g., a sample scanning apparatus). Each class of event reports the temporal signature with a different precision: the absolute time for the photon events (t_{photon}) - shown here in green - and the laser synchronisation events (t_{SYNC}) - shown here in blue - have ~ 30 picoseconds precision, and the absolute time for the reference events ($\hat{t}_{\text{REF}}$) - shown here in red - has a ~ 4 nanoseconds precision. Starting from these temporal signatures, it is possible to derive several other different temporal quantities. For example, for each photon event it is possible to calculate the so-called start-stop time (Δt), which describes the delay of the photon event with respect to the successive sync laser event. Together with the temporal signatures, the TTM records also the number of the channels (ch) or inputs (l) associated to the photon or reference event.

in a differential configuration scheme. While the absolute time for the reference events ($\hat{t}_{\text{REF}}$) has ~ 4 ns time-resolution as they are sampled using coarse counter TDCs. Starting from these primary temporal signatures, it is possible to calculate other different temporal quantities. For example, from a TD-TCSPC design perspective, for each photons it is possible to derive the so-called start-stop time (Δt), which describes the delay of the photon event in respect to the next (in time) sync laser pulse event (Fig. 3.2) (tables in Appendix D report the nomenclature used in this thesis work). Ought to say that, being a multi-channel TDC, together with the temporal signatures, the TTM records also the channels (ch) identifiers to associate single photons to different inputs or reference events.

In the next subsections the main (and fundamental) FPGA component design blocks that were developed for engineering the final TTM-TDC architecture are described.

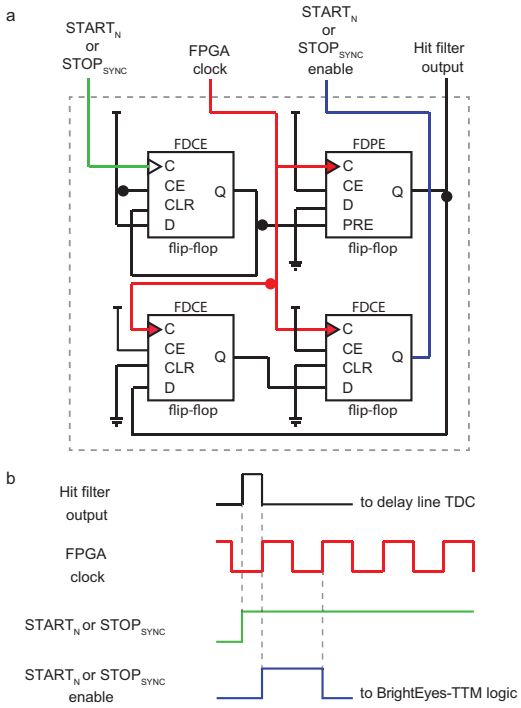

Figure 3.3 **Schematic circuit of the hit filter component (a) and related input-output digital signals (b)** . **a** Hit-filter FPGA digital circuit. The intimate digital-electronic layout of the hit-filter made up by only four flip-flops of FDCE and FDPE types. These four flip-flops are interconnected in a special way so that the hit-filter can shape the incoming photons and sync signal lengths based on the sampling FPGA clock period and, at the same time, for generating a toggle signal event (the photon or sync enable signal) for each detected $START_n$ (photons) and STOP (sync) events. **b** Input and outputs signals of the hit-filter logic. Primary digital hit-filter output (top), sampling FPGA clock (second row), rinsing edge of photon or sync event (third row), photon or sync enable signal that has the duration of an FPGA clock period (bottom).

3.2.1 Hit filter module

The hit-filter is a circuit used to shape and stabilize the input signal before feeding into the TDL architecture. When photon or laser sync event occurs, this circuit keeps the signal high (logical high '1') until it gets sampled by the internal clock and thus recorded by the BrightEyes-TTM in accordance with the implemented time-tagging principle. Here, the hit-filter component guarantees the stability of the TDL input signal for the amount of time it takes (dead time) to correctly sample an incoming event (Fig. 3.3).

The hit-filter logic is also necessary to avoid the clogging of the TDL module and allow for the TDC module to be ready to sample incoming signals thus reducing the dead-time of the architecture which, thanks to the hit-filter, becomes independent from the signal pulse

duration (hold-off). While the hit filter output signal is solely used to activate the TDL module, the photon enable signal is distributed to the entire TTM architecture logic to sample and record the arrival of a photon (or sync pulse) on a specific channel together with their ToFs. In the current architecture a hit-filter module was used for each deployed TDL.

3.2.2 Tapped-delay-line module

A standard TDL architecture was assembled in the FPGA by piling up and interconnecting the CARRY elements built in the Kintex-7 CLBs (CARRY4 elements for the Xilinx family-7 FPGA devices). In order to avoid the documented *bit-bubbles* problem, the TDL output was sampled after each CARRY4 component instead of accessing sub-CARRY delay contributions. In this way, it is still possible to achieve high-time resolution without deploying extra-FPGA resources for compensating the bit-bubble issue. The present BrightEyes-TTM design accommodates 22 independent and parallel TDLs: 21 TDL channels for recording single-photon events and one TDL entirely dedicated to the sampling of the PW laser sync signal events arranged according to the schematic presented in Fig. 3.5.

Thermometer to binary converter module

Each of the TDLs is equipped with a thermometer-to-binary (T2B) circuit encoder which was *ad hoc* developed within this PhD project for decoding the TDL readouts in order to compress the digital tags into an agile and easy-to-handle binary data format. The implemented T2B is essentially a look-up-table (LUT) (Table 2.1) which function is to match the TDL thermometer-like data with their correspondent binary number representation.

3.2.3 Event filter module

The event-filter module is a data-input/output filter that reduces the amount of data the BrightEyes-TTM has to cope with by avoiding to register information when no photons ($START_n$) nor laser sync events ($STOP_{SYNC}$) are detected. Time tagging-data get registered in a first-in-first-out (FIFO) FPGA internal memory only if one of the following conditions is met: (i) a $START_n$ event in one of the photon channels, i.e., a photon event; (ii) a $STOP_{SYNC}$ event following a $START_n$ event, i.e., a laser sync event occurs after a photon event. By discarding $STOP_{SYNC}$ events that do not have a corresponding $START_n$ enable event, the data size can be significantly reduced. Intrinsic working principle of hit-filter component is described in Fig. 3.4.

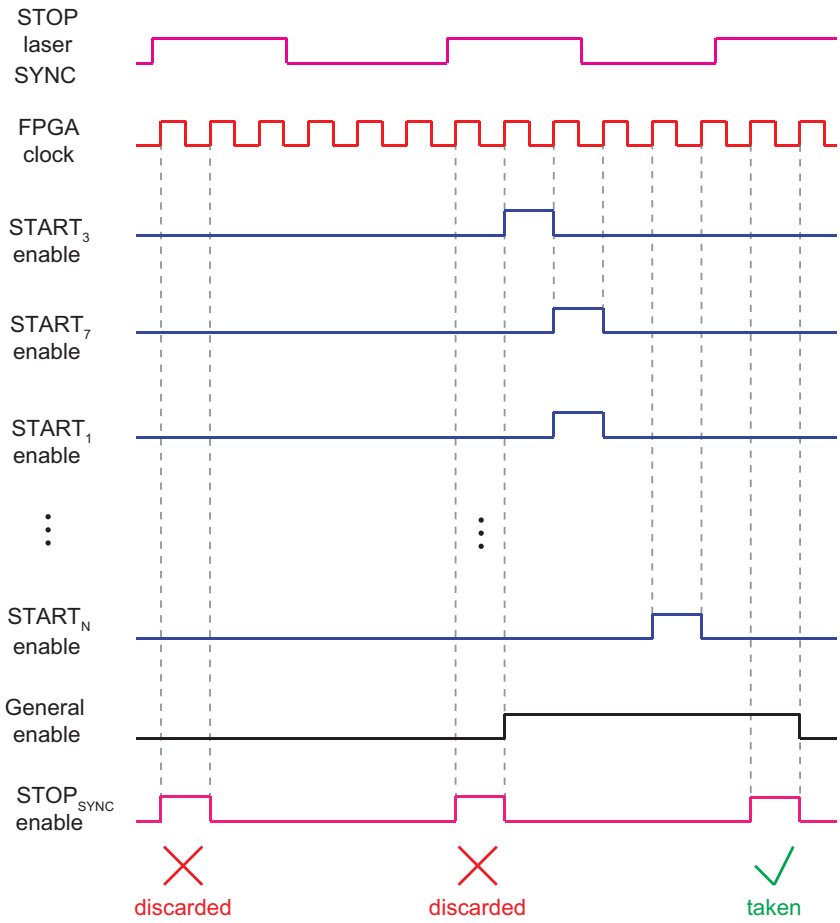

Figure 3.4 **Logic circuit of the event filter component**. All valid photon enables signals (from $START_1$ enable to $START_N$ enable), produced by the hit-filter modules whenever a $START_{photon}$ (or $STOP_{SYNC}$) event is detected, are used to efficiently record the multi-channel data tags. The event filter was designed to optimally handle time-tag data for high repetition rates of the PW laser source (up to 80 MHz) used in single-photon applications. As it is not efficient to sample and tag all the incoming laser pulses (laser SYNC events) and stream the related information together with the data of sampled photons to a processing unit, the event filter circuit works backwards: when a photon is detected in channel i, the corresponding $START_i$ activates a general enable signal. The general enable signal remains active until a successive laser pulse sync signal ($STOP_{SYNC}$ enable) is detected. If the general enable signal is high at the moment of a $STOP_{SYNC}$ pulse, it means that at least one photon has been detected, and only in that case the FPGA circuit tags and registers the $\Delta t(ch)$ start-stop time on a single (or multiple) channel.

3.2.4 General schematic of the BrightEyes-TTM

All the previously described components (e.g. hit-filter, TDL, T2B, event-filter) were connected as macro-blocks in the FPGA with the aim of building a versatile and multi-channel time-tagging module design. The final implemented BrightEyes-TTM architecture hosts 21 independent and parallel delay-line TDC modules yielding picosecond time-resolution for sampling and registering single-photon events. The architecture also implements and uses a 16-bit wide free running coarse counter for accomplishing the differential delay line TDC approach (Nutt method) and, at the same time, for sampling up to 3 external synchronization signals with a nanosecond precision. The 3 external synchronization signals are acquired with the use of edge detector components in combination with counter-based coarse TDC approach (i.e. the free-running counter). In the TTM design there is also a TDL component (hit-filter, delay line TDC module & T2B) which is uniquely dedicated to the acquisition (always yielding picoseconds resolution) of the $\mathrm{START_{SYNC}}$ signal. The contribution of the temporal signature of the $\mathrm{START_{SYNC}}$ is shared by all the 21 $\mathrm{START_N}$ inputs so that they can all be referred to the same laser sync measure. All the data coming from the TDLs, the edge detectors and the digital counter are handled by the event-filter circuit before being processed by a data assembly module. The data assembly module collects a multiplicity of digital input signals and values (i.e. $\Delta T_{\mathrm{START}}(ch)$ and $n_{\mathrm{photon}}(ch)$ as well as valid arrival flags for the photons, ΔT_{STOP} and n_{SYNC} as well as its valid digital flag for the laser sync, and the valid arrival flags for the $\mathrm{REF_M}$ signals) and arranges the digital data tags into a suitable form in order to be stored into a FIFO memory. The FIFO memory buffers incoming data awaiting to be sent over a host-processing unit via a USB 3.0 data interface module (Fig. 3.5).

BrightEyes-TTM TDC

In the BrightEyes-TTM architecture, the combination of separate and independent flash TDC modules for the input (photon) channels and a shared flash-TDC for sampling the laser sync signal, together with a common 16 bit-wide coarse free-running counter (Fig. 3.6) for all the implemented channels not only levels out the non-linearity but also offers the possibility to (i) keep track of the experiment time, allowing the TTM to have a virtually infinite temporal range, and (ii) deal with different laser sync rates. Together with the photons and laser sync arrival times, the wrapping events of the coarse counter are also registered and used to calculate the experiment time by simply combining the number of wraps with the period of the FPGA reference clock (240 MHz i.e. ~4.2 ns). The ability of the TTM to reconstruct the time axis based on the internal FPGA clock also allows the TTM to be used with different

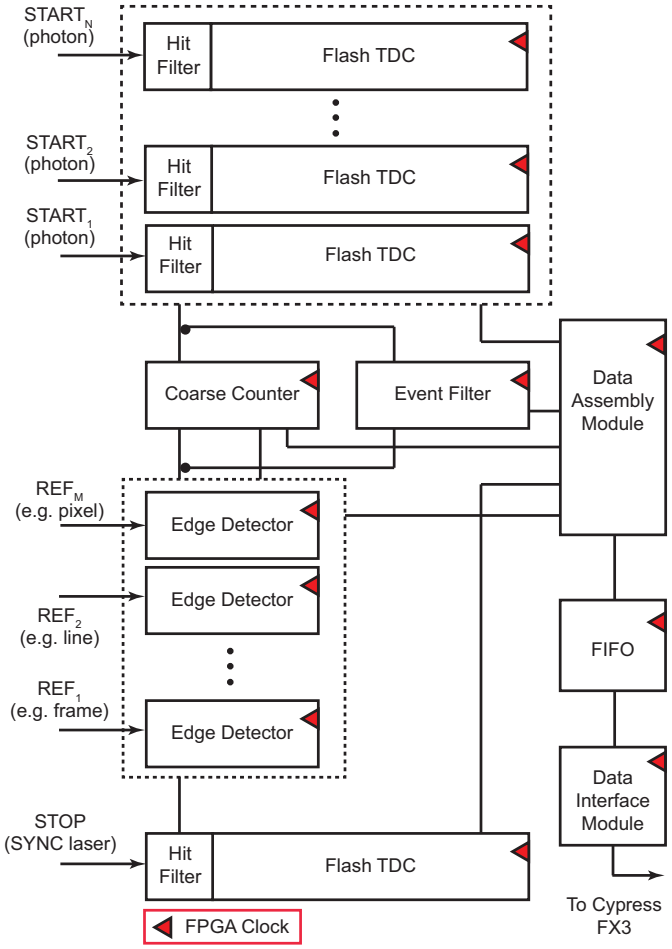

Figure 3.5 **Interpolating TTM-TDC FPGA architecture**. General and simplified circuit architecture of the FPGA-based BrightEyes-TTM. Tapped delay line-based flash TDC modules and relative hit-filters for sampling the $START_N$ (N = 21) signals and the laser SYNC event, with picosecond precision, with respect to the FPGA clock (FPGA clock in red) (top and bottom portion of the figure). Free running coarse counter for implementing the sliding scale TDC technique and for sampling the REF_M (M = 3) synchronization signals with a nanosecond precision (~4.2 ns) thanks to edge detector components. Event-filter circuit to reduce the data throughput by transmitting information only when photons are detected (middle-top portion). The data assembly module arranges the digital data tags into a suitable form in order to be stored into a FIFO memory, FIFO memory to buffer incoming data before sending them over a host-processing unit via the data interface module through the Cypress FX3 chip (right).

laser sync frequencies without needing to change the FPGA firmware. As a result, the TTM can be used to work at different temporal ranges, having always the same linear response.

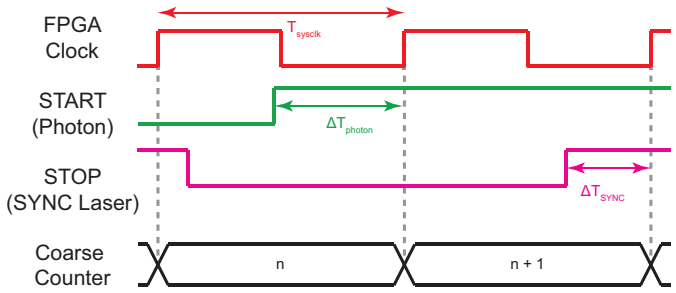

Figure 3.6 **General fundamental concept of the sliding scale approach**. TTM interpolating architecture working principle. FPGA clock used to (i) drive all the TTM architecture components and (ii) as a fundamental reference signal for all the time measurements (top). The TTM circuit architecture tags the START-photon (green) and STOP-sync (pink) signals with respect to the FPGA sampling clock (middle) and saves/computes both the $\Delta T_{\mathrm{START}}$ and ΔT_{SYNC} (i.e. integer values representing the number of tapped-delays - in the delay line - that the signals have travelled through before the arrival of the FPGA clock rising-edge) signals respectively. Coarse free-running counter increasing its value at each FPGA clock rising-edge event for reconstructing, in a post-processing phase, Δt photon start-stop time.

3.2.5 SuperSpeed Explorer Kit - USB 3.0 controller

The TTM architecture uses a USB 3.0 board (Cypress Super-Speed Explorer kit board, CYUSB3KIT equipped with the Cypress FX3 USB 3.0 chip) to transmit the data to an host processing unit (PC) (Fig. 3.7). The CYUSB3KIT is connected through an adapter card (CYUSB3ACC) to LPC-FMC connector present on the Xilinx KC705 evaluation board. The 5 Gbps USB 3.0 protocol, effectively limited at 3 Gbps, was chosen as the most universal plug-n-play method for interfacing the TTM with a PC: nowadays USB3.0 ports are available in most modern PCs, thus assuring an extremely flexible use of the BrighEyes-TTM. In order to use the FX3 chip, a dedicated module in the FPGA was developed.

FX3-VHDL module

The implemented FX3-VHDL module has a simple interface for the data transmission and it manages the FX3 control signals as well as the data-bus. The module was designed to work with the FX3 programmed with the *SF_streamIN* firmware from the AN65974 example provided by Cypress. This module allows ultimately for the acquired data to be transmitted to a host-PC using a simple plug-n-play USB protocol

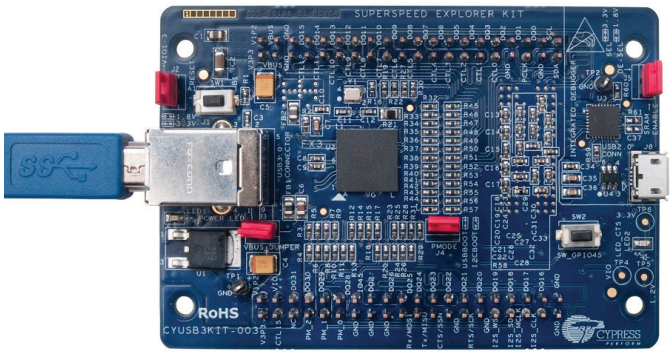

Figure 3.7 **The CYUSB3KIT-003 EZ-USB® FX3™ SuperSpeed Explorer Kit**. The FX3 SuperSpeed Explorer Kit is an development board enabling users to add USB 3.0 device functionality to any system. The FX3 SuperSpeed Explorer Kit is built is powered by a fully accessible ARM9 which pins are completely accessible (top and bottom rows) allowing the FX3 device to be fully configurable and interfaceble to any external hardware device like an FPGA.

3.3 Data transfer

To transfer the data from the TTM to the PC, we designed a simple data protocol, whose major advantage is the scalability to add photon channels, as well as its flexibility. In a nutshell, the protocol together all the TTM inputs in a frame-like format having maximum rate of 240 MHz, i.e., the frequency at which the whole TTM architecture operates. Under this scenario, the data protocol foresees a unique frame-like data structure streamed to the communication port (USB 3.0) in 32-bits long words.

3.3.1 TTM data transmission protocol

Since the current BrightEyes-TTM version can read 21 photon channels, it needs to transmit one header word and seven payload words (3 photon channels *per* payload word), thus 256 bits in total. To check the data receiving order and to avoid misinterpretation, each word includes 4 bits as identifier (ID). The first word (header, ID = 0) includes the following information: (i) three bits used as boolean-flag for the reference (REF) events (in our applications the pixel, line, and frame clocks); (ii) the 8 bits representing the value measured by the tap-delay line of the SYNC channel ΔT_{STOP} (in our application the synchronisation signal from the pulsed laser), and (iii) the SYNC data valid boolean-flag which confirms that a SYNC event has occurred; (iv) the 16 bits representing the number of clock cycles of the free-running 240 MHz counter. The successive payload words (ID > 0) contain the information of three photon channels. For each photon channel the word contains: (i) the 8

bits representing the value measured by the tap-delay line of the respective photon channel $\Delta T_{\mathrm{START}}(ch)$; (ii) the channel data-valid boolean-flag confirming that an event in that channel has occurred. Each payload word contains also a general purpose single bit, which can be used to implement another $\mathrm{REF_N}$ signal (Fig. 3.8.

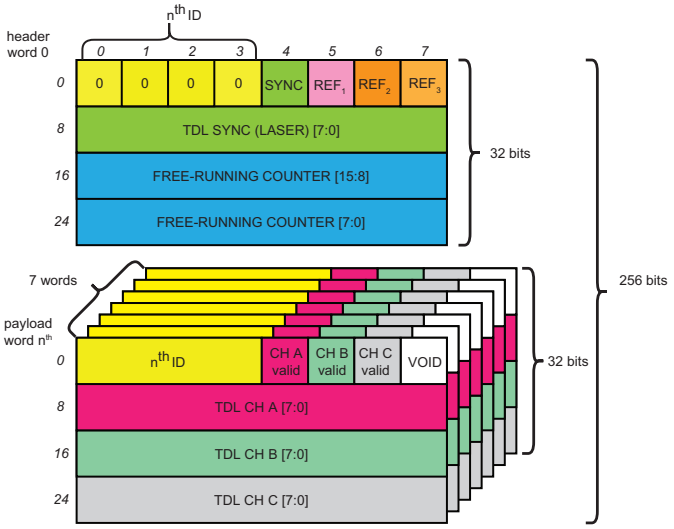

Figure 3.8 **Data structure**. The data structure has an header 32-bit word and, in case of 21 channels, seven payload 32-bits words each one identified with an associated ID number. The channel CH A, B, C are different in each payload word and they are sequential, corresponding to channels 1 . . . 21.

Trigger events for TTM data transmission

Since the data structure is 256 bit long, and, in principle, we have to transmit the structure with a rate of 240 MHz, the data throughput should be 7.68 Gbps. However, the USB 3.0 has an effective bandwidth of 3 Gbps. For this reason, the data structure is transmitted only if one of the following conditions occurs: (i) a START event in one of the photon channels, e.g., a photon event; (ii) a STOP event following a START event, e.g., a laser SYNC event occurs after a photon event (event filter); (iii) a REF event, e.g., a pixel/line/frame event; (iv) a force-write event. The force-write event is fundamental for reconstructing any time measurement (relative or absolute) that requires the coarse counter values. Indeed, since the data structure uses only 16 bit for storing the 240 MHz coarse counter value, the counter needs to reset every 273 μs. To guarantee the possibility to always reconstruct the relative or absolute value for each event, we implemented an internal trigger which forces to transmit the data structure at least once every 17 μs, value that corresponds to one sixteenth of the course counter reset period.

Fail-safe streaming mode

To improve the robustness of the data transfer process, we mitigated the data throughput peaks by buffering the data in a large (512 kB) BRAM-FIFO on the same FPGA. The TTM code contains a mechanism which guarantees that in case the FIFO gets filled over a certain threshold, i.e., the average data throughput exceeds the USB 3.0 data bandwidth, the TTM enters temporarily in a fail-safe mode, giving priority to the REF_M of events. For example, in the case of imaging, the TTM gives priority to the pixel/line/frame flags and to the force-write events. This strategy guarantees the reconstruction of the absolute time of each event (photon or REF) and the image.

3.3.2 TTM new data transmission protocol

The first developed transmission protocol was mainly implemented for validating the BrightEyes-TTM architecture rather then optimizing the data-transmission procedure. Indeed, the 256 bits long data - 8 words in total - , having a frame-like format, get entirely transmitted in bulk to the host-computer. In the earliest development phase this operation mode for data transfer ensured no-data loss but on the other hand lacked any type of optimization in respect with the amount/size of data that was sent to the computer largely impacting the final acquired data size. That is why a new and improved transmission protocol was conceived: the time-tagging data are organized in 16 bit-wide chunks where 3 chunks are dedicated to a data header, which always gets transmitted, while the other chunks, which identify the photon-channels, are optional (Fig. 3.9). A 16 bit photon channel chunk gets transmitted along with the data header only if a photon event or laser sync event (that occurs after a photon event (event filter)) is actually registered. Unlike the initial data transmission protocol where a 256 bit-long data frame was transmitted, upon a trigger event, regardless if a photon-channel entry was actually empty, this new one, being based on compact data-chunks, avoids sending empty data by checking if the value of the channel data-valid boolean-flag confirms that an event in that channel has truly occurred. The new transmission protocol not only allows for data-size shrinking but also for a quick design scalability, being capable of handling up to 128 IDs in parallel i.e. 124 photon channels subtracting the header's and the laser sync IDs.

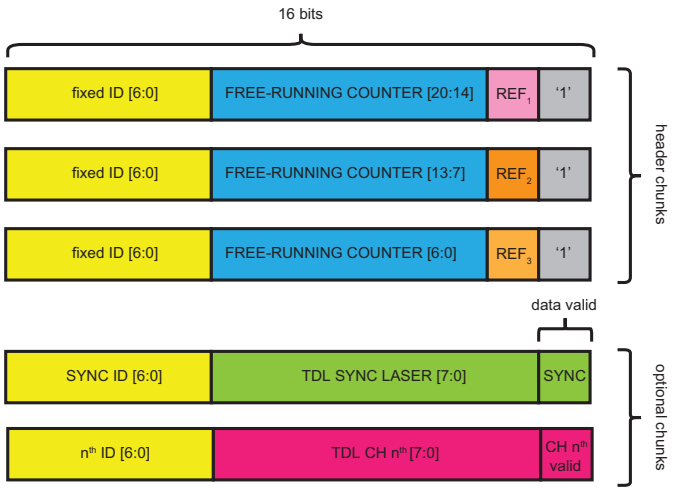

Figure 3.9 **New data structure**. The new data structure is made up by 16 bit-wide chunks. The data header is constituted by 3 chunks in which the free-running counter value and the REFs signals are registered (top). In the optional chuncks (bottom), which get transmitted only if the data-valid flag is equal to '1', the TDL vaues of the laser sync and the photon channel events are stored.

3.3.3 Receiving data from the TTM

In the current BrightEyes-TTM implementation, the USB 3.0 FX3 chip effectively transfers the data to the PC. Here, a data receiver software checks the integrity of the received data stream (i.e. the data chunks IDs must be in correct order), and, if the data structure is properly received, it sequentially write the data to the raw file without any process (raw data). The data receiver uses the *libusb-1.0*, and is developed in C programming language. Two OS-dependent version of the data receiver program were developed. The more used and most tested one is a CLI program *dataReceiver* written in C/C++ developed for Linux OS (Fig 4.1). A second Windows-based version was also developed for extending the compatibility of the BrightEyes-TTM with a variety of host data processing units.

3.4 Custom I/Os SMA-FMC daugther connector card

The BrightEyes-TTM interfaces with the photon-signals thanks to a custom-built I/0s FMC daughter card connected via the FPGA mezzanine connector (FMC-HPC). In principle, if needed, also the I/0s FMC daughter card can be modified, further developed and yet manufactured to adapt the BrightEyes-TTM to any type of LSM signal. The custom-built I/0s FMC daughter card interlocks with the Xilinx KC705 Evaluation kit as shown in Fig. 3.10.

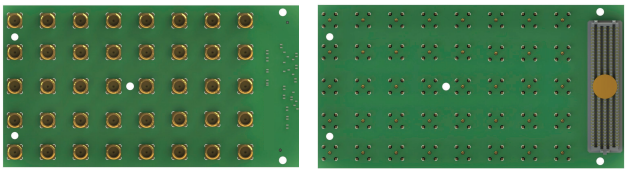

Figure 3.10 **Custom I/Os SMA-FMC daugther connector card**.

3.5 BrightEyes-TTM final assembly

The BrightEyes-TTM is composed by three main parts: the FPGA evaluation board; the FX3 data transmission chip (EZ-USB® FX3™ SuperSpeed Explorer Kit and FMC Interconnect Board for the EZ-USB® FX3™ SuperSpeed Explorer Kit); a custom-made I/Os SMA-FMC daughter connector card. The three hardware components are assembled according to Fig. 3.11. Both the FX3 data transmission chip and the I/Os FMC daugther card easily interlock to the main Xilinx® FPGA board.

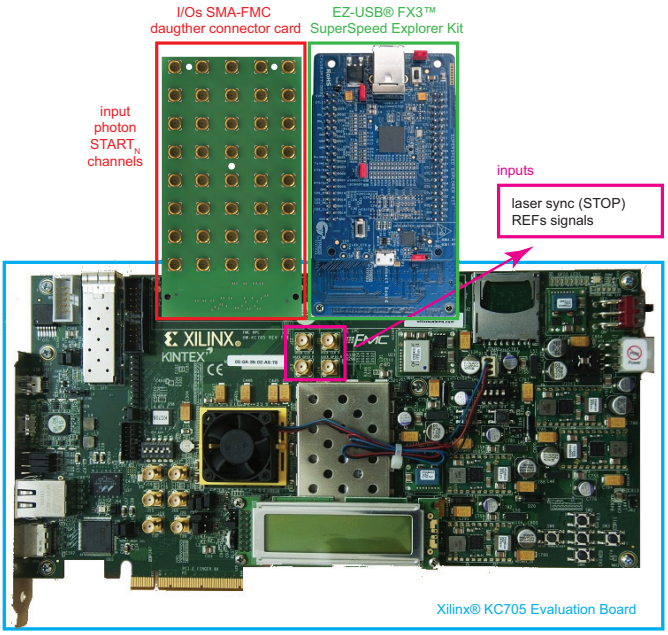

Figure 3.11 **BrightEyes-TTM final assembly**.The Xilinx® KC705 Evaluation board, the Cypress® FX3™ SuperSpeed Explorer Kit and the connector card can be easily stacked together, using FMC connectors which interlock the three components. I/Os connections on the FMC daughter card are labeled for a more intuitive assembly as they receive the input photon channels. REF_M and laser SYNC signals are directly connected to the main board using dedicated SMA connectors.

3.6 Conclusions on implementing the BrightEyes-TTM

The BrigthEyes-TTM was implemented designing a flexible and scalable multi-channel differential delay line TDC approach that offers a trade-off between time-resolution, system linearity, temporal range and FPGA-CLBs resource usages (see specifications in Table 3.1). Moreover, the BrigthEyes-TTM was assembled and developed using commercially available dev-kits thus allowing for the architecture to be easily reproduced and granting open-source features to this project. In addition, compared to multichannel commercially available time-tagging platforms which require, in order to achieve a multi-channel configuration, to stack-up together multiple modules, the BrightEyes-TTM project was carried out on a single-board architecture that can work as a slave USB 3.0 plug-n-play device with pre-existent SP-LSM setups. The host-processing unit requirements to operate the BrightEyes-TTM are reported in Table 3.2.

Table 3.1 **BrightEyes-TTM implementation features**

	No.
Input channels with picoseconds precision	21
Input channels with ~4.2 ns precision	3
Laser sync channels with picoseconds precision	1

Table 3.2 **BrightEyes-TTM operation**

PC interface	USB 3.0 SuperSpeed
PC requirements	min. 1.5 GHz CPU clock, min. 16 GB RAM memory, SSD hard disk
Operating system	Linux (native)

Chapter 4

Python-based data processing software

After BrightEyes-TTM data is transferred to a host-processing unit, it is saved in a low-level data format. If on one side the raw data format assures fast data transfer rates via the USB 3.0 link as well as fast data writing speeds on a ROM support device, on the other, lacks an organized and user-friendly structure. With the aim of creating a convenient and handy data structure, the raw data is pre-processed, refined and organized into a more flexible table-like format provided along with a HDF5 file extension. Ultimately, the pre-processing data phase is followed by a data calibration phase in which bin-by-bin calibration is applied to time-resolved data entries (Fig. 4.1) maintaining the HDF5 extension.

The pre-processing, calibration (and data-reconstruction) phases are carried out in a Python 3 environment in which a specific library - which can be found on GitHub at libttp - was developed in conjunction with dedicated Jupyter notebooks to reconstruct, visualize and analyze time-tagging data. In the lipttp.p library, Cython extension functions were used to achieve C-like speed performance and allow for fast data reconstruction and processing.

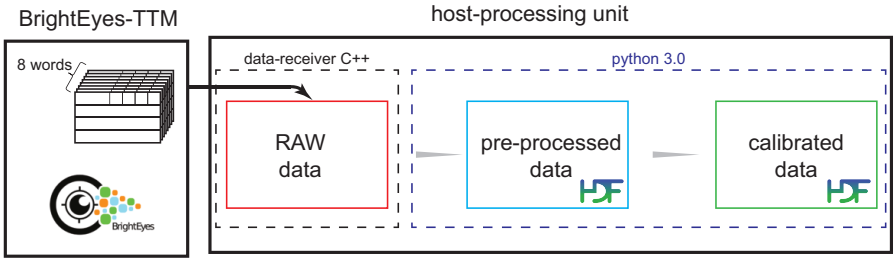

Figure 4.1 **Data processing pipeline**. A low level data-format arranged in 8 words - according to the earliest data transmission protocol - is streamed by the BrightEyes-TTM and saved into a raw-data form using a C++ based software program. Raw data gets pre-processed and refined in a python-based analysis environment for data calibration and further data reconstruction.

RAW DATA

free-running coarse counter	REF_1	REF_2	REF_3	SYNC valid	TDL SYNC	CH 1 valid	TDL CH 1	CH n^{th} valid	TDL CH n^{th}	CH 21 valid	TDL CH 21	
19325				1	41	1	17					1
19326										1	32	
19327						1	54					
19328								1	27			
19329				1	19							2
19330	1			1	29	1	11			1	9	3
19331			1							1	54	
19332				1	37	1	7					4
19333	1			1	13					1	8	5
...	...	...	...	...	...	...	...	...	...	...	...	

Figure 4.2 **Raw data table**.The top table represents the raw data as received. In the top table, the gray cells are the data-valid flags. Each SYNC data-valid flags (in dark gray) is associated to a new unique index (number yellow highlighted).

4.1 Data pre-processing

In the pre-processing phase, raw data is transformed into a table-like organized structure in which all the tagging events are assigned a specific and unique column identifier (*idx*) and saved into a compressed HDF5 file format. The HDF5 file consist of several tables, each single-table-entry *idx* is used to easily access and merge the information stored in the different data-tables to allow for the HDF5 to be used like a database through queries (Fig. 4.2). In order to shape the raw-data into table-like format, Pandas extension was used. Particularly, it offers data structures and operations for manipulating numerical tables as well as time series, that is why it was chosen within this PhD project.

4.1.1 Experiment time

The first effective pre-processing operation involves the use of the coarse counter information, streamed and saved in the raw data-frame together with the single photons, REFs and laser sync events. The value of the coarse counter is used to derive and create a monotonic counter n. With the monotonic counter n, it is possible to calculate (i) the experiment time, (ii) the arrival time of each photon event with respect the SYNC event for TCSPC histogram reconstruction or with respect to a REF event for imaging and FLIM measurements. Since the coarse free-running counter is 16 bits wide, it resets (approximately) every 273 us

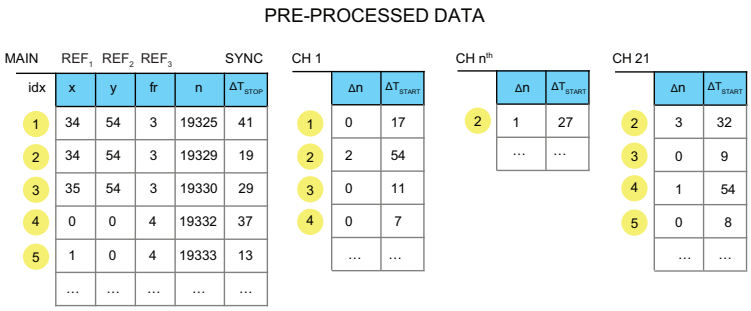

Figure 4.3 **Pre-processed data table**. In the pre-processed data-format all the SYNC events - labelled in yellow - as well as the REF events are stored in a main table. The SYNC events are characterized by two values (i) the value of the monotonic counter and (ii) the digital value of the dedicated TDL readout. For the REF events, here used for imaging reconstruction purposes, the value of the correspondent position in the image (x, y, fr) of the SYNC event is stored. Additional tables, for storing the photon channels data, are also elaborated in the pre-processing phase: for each detected photon the difference (ΔT) of the monotonic counter values in respect with the associated SYNC event is saved together with the TDL digital readout.

(considering an FPGA clock period of ~4.2 ns); therefore, to obtain a consistent monotonic counter n, the 16 bits long free-counter provided by the data structure is constantly updated: when the free-counter value (idx) is lower than the one in the previous data structure ($idx-1$), the value 2^{16} is added to it and added to the following counter (n) values. In addition, the monotonic counter, yields the possibility of having, in theory, an unlimited time range for the BrightEyes-TTM TDC. Indeed, by exploiting the wraps of the coarse counter the time range is not limited by the FPGA hardware.

4.1.2 HDF5 structure

The HDF5 file inner structure is made up of several tables: there is a dedicated table for each active (photon) input channel (at the moment N = 21 tables for the input channels) plus a main table to store the laser sync events as well as the REF events. The main table has a row for each SYNC channel event and contains the monotonic counter n value, the REF signal coordinates in the case the BrightEyes-TTM is used for imaging i.e. x, y, fr, the TDL value ΔT_{STOP} value, and the unique row index idx. While the photon channel tables have a row for each photon: each row contains the TDL value readout $\Delta T_{\text{START(ch)}}$, the elapsed clock cycle $\Delta n(ch)$ (i.e. the value of the monotonic counter difference between the photon and the associated laser sync event), and the index idx of the row of the corresponding sync event (Fig. 4.3).

4.1.3 Image reconstruction

To simplify the reconstruction of the image, in this pre-processing phase the REF information for the pixel/line/frame is elaborated. As described, pixel/line/frame REF events are included in the table the columns x, y and fr. Namely, the pixel event increases the x counter; in case of the line event, the x counter resets and the line counter y increases; in case of the frame event, both the x, y counters reset, and the fr counter increases. In this way it is possible to match each photon (or laser sync) event to a specific pixel, within a specific line of a specific frame (see Main table in Fig. 4.3).

4.2 Data calibration

Remarkably, the HDF5 file contains all the information as received by the TTM, but structured in a way that is much easier to access. However, this information still contains numbers of coarse counter (FPGA clock cycles) or raw tapped-delay line readouts. Therefore, an offline calibration phase is needed to transform this digital information in temporal information. In particular, the bin-by-bin calibration, transforms each TDL readout value $\Delta T_{\mathrm{START}}(ch)$ or ΔT_{SYNC} in a temporal value $\Delta T_{\mathrm{START}}(ch)$ or Δt_{SYNC}, which can be used to calculate all (both relative and absolute) temporal signatures of each event. The output of the calibration is again an HDF5 file, with a structure similar to the non-calibrated (pre-processed) file. The main table has a row for each SYNC channel event. Each row contains the absolute SYNC time $t_{\mathrm{SYNC}} = n_{\mathrm{SYNC}} \cdot \mathscr{T}_{\mathrm{sysclk}} + \Delta t_{\mathrm{SYNC}}$ (where $\mathscr{T}_{\mathrm{sysclk}}$ is the value in ps of the FPGA system clock), the coordinates x, y, fr and a unique row index idx. The photon channel tables have for each row the start-stop time $\Delta t(ch)$, and the index idx of the row of the corresponding SYNC event.

4.3 TCSPC histogram reconstruction

Since the TTM architecture uses a start-stop reverse strategy to reconstruct the photon start-stop time for a given channel ch, as per the even-filter circuit mechanism where a laser-sync is captured only if a photon was previously detected, it is necessary to recover the information about successive SYNC laser events. The pre-processing step-phase identifies for each STOP (SYNC - laser sync) event the corresponding START (photon) event and creates a table that accounts for the detected photons. Each table row contains a STOP (SYNC) event, and includes: (i) the relative monotonic counter n_{SYNC}; (ii) the relative TDL value ΔT_{STOP}; an

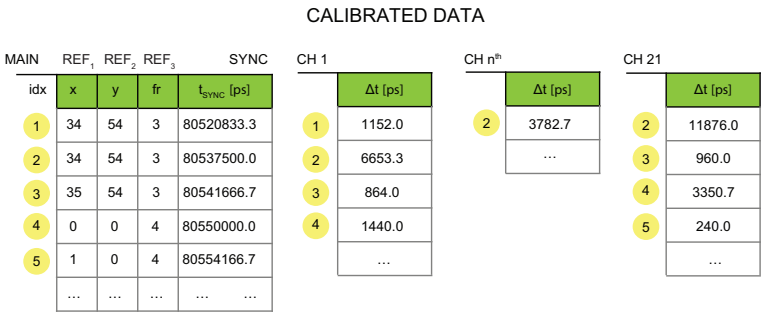

Figure 4.4 **Calibrated data table**. In the calibrated data format the information of the monotonic counter and of the TDLs readouts are fused together using the Eq. 2.2 and applying the bin-to-bin calibration procedure. Similarly to the pre-processed data, the calibrated data shows a multi-table structure: a main table is dedicated to $\mathrm{REF_M}$ and SYNC events while photo-channel data are stored in individual and separate tables.

entry for each photon event linked to this specific STOP (SYNC) event. In particular, each entry contains: the number of elapsed clock cycles $\Delta n(ch) = n_{\mathrm{SYNC}} - n_{\mathrm{photon}}(ch)$ and the TDL value $\Delta T_{\mathrm{START}}(ch)$. With such information it is possible, for each acquired channel, to build the histogram of the overall calibrated $\Delta t(ch)$ start-stop time for all the tagged photon events thus allowing for the TCSPC histogram reconstruction.

4.3.1 TCSPC histogram time bin width

Thanks to the use the differential delay-line TDC method to implement the fine TDC, and an off-line (post-acquisition) bin-by-bin calibration, the final bin time-width of the start-stop (TCSPC) histogram can be arbitrarily chosen. In the current work the same bin width value, 43 ps was always used. This corresponds to the average of the calculated bin widths for all the deployed flash-TDC modules. In conclusion, since we use a sliding scale differential TDC module and off-line post-acquisition calibration, the bin width can be virtually chosen to be any value greater than 43 ps (see Chapter 5.6).

4.4 Conclusions

In an effort to keep the project a true open-source , the whole data reconstruction and processing was developed using a free-software environment such as Python 3. Python and its libraries, allow for future modifications and changes of the developed software analysis giving future users the possibility of rebuilding the entire data processing and calibration procedure.

Chapter 5

BrightEyes-TTM characterization and validation

In order to characterize BrightEyes-TTM performances and, at the same time, validate the developed architecture, the TTM was firstly tested on a *bench* and then integrated to a LSM environment for further validate the system performing: (i) fluorescence spectroscopy measurements and (ii) comparison measurements with a commercially available multi-channel time-tagging card.

5.1 BrightEyes-TTM testbench performances

To assess the linearity of the TTM time-response, a statistical code-density test was firstly performed (Appendix A), by connecting the BrightEyes-TTM to a dedicated signal generator, named SYLAP (Appendix B), and an APD detector. With SYLAP, single-shot precision (SSP) assessment was carried out for all the BrightEyes-TTM (N = 21) deployed input channels (Appendix A).

To perform both the code-density tests and the SSP experiments for all photon input channels of the TTM, the flexibility of the BrightEyes-TTM FPGA-based architecture was exploited, and in particular, the possibility to reprogram the FPGA according to different requests. Indeed, physical switches were implemented within the FPGA architecture which allow simultaneously connecting (mirroring) a single input channel of the board to all 21 photon channels. This feature gives the possibility to measure the same event on all photon channels.

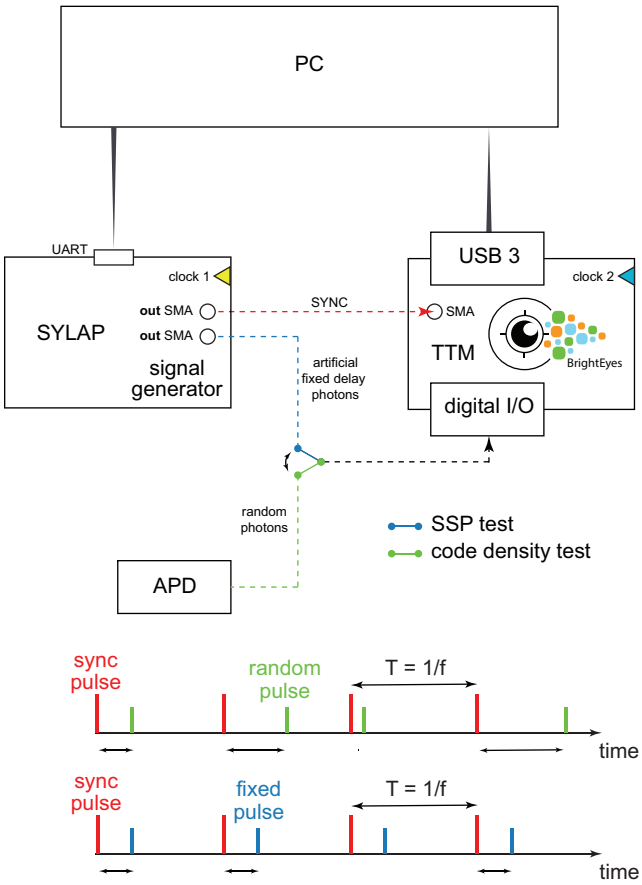

Figure 5.1 **Test bench system configuration**. The setup used for the BrightEyes-TTM tests and characterisations. The TTM STOP (laser sync) is connected to a clock generated by SYLAP. The TTM start input can be connected the APD for generating random unsynchronized pulses **(green)** to accomplish the statistical code-density test; or can be connected to SYLAP to generate pulses with a fixed delay respect to the clock **(blue)** that mimic single-photons for assessing the single-shot precision.

5.1.1 Statistical Code density test

To begin with, a code-density test (Appendix A) was carried out using, as SYNC signal, the clock source from SYLAP (i.e. 50 MHz frequency yielding a time period of $\mathscr{T}$ = 20 ns) and as random photon signal (i.e., temporally uncorrelated with the SYNC signal), a TTL output from an APD detector (APD, SPCM-AQRH-13-FC, Perkin Elmer, Waltham, Massachusetts, USA). A schematic configuration of the code-density test is depicted in Fig. 5.1. The APD was illuminated with natural light, maintaining a photon-flux well below the saturation value of the detector. With such connection scheme the TCSPC histogram, after

a bin-by-bin calibration procedure (Chapter 2.4.2), was reconstructed for all the deployed channels, here in Fig. 5.2 the TCSPC histogram for photon channel #11 is reported.

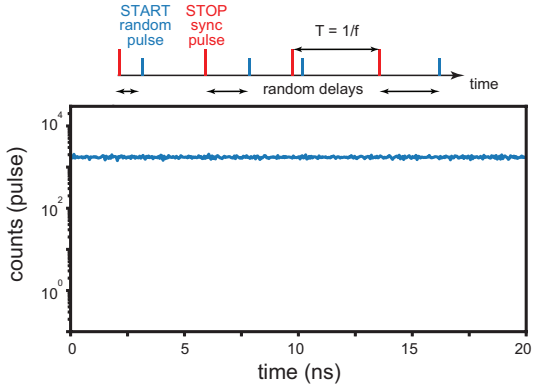

Figure 5.2 **Statistical code density test**. Temporal schematic representation of the signals involved in the experiment: a fixed frequency SYNC (STOP) clock signal f = 50 MHz and a random train of pulses (START) (top). The reconstructed start-stop TCSPC histogram, i.e., counts versus time (lower).

Differential non-linearity

The aim of computing the DNL is to understand to which degree the difference in time widths of all the possible time bins deviates from a common average value which, ideally, should be a constant flat line, indicating that every time-bin has an equal time-width within the measured temporal range. Having set the LSB to 43 ps, and after having computed the differential non-linearity (DNL) - Fig. 5.3 - (according to Eq. A.1 in Appendix A) over the reconstructed code density TCSPC histogram, the σ_{DNL} was calculated to be 6 % of the LSB, yielding an RMS value of 2.58 ps: the time-response in the tested range (i.e. 20 ns) can be considered linear and equal to 43.00 ± 2.58 ps. This means that all the time-bins of the TCSPC histogram, on average, differ only by 2.58 ps from each other.

Integral non-linearity

The integral non-linearity (INL), which is a figure of merit used to determine to which degree the response of a time-tagging system differs from the ideal linear behaviour, was then computed (according to Eq. A.2 in Appendix A) on top of the DNL results. The INL gives an estimate of the difference between a TTM measurement and the actual time of arrival of a photon-event. If the TTM is linear, the INL should hold constant around the zero. The σ_{INL}

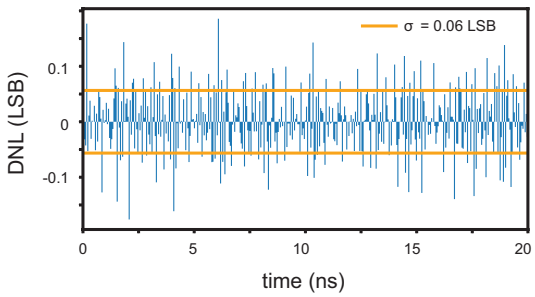

Figure 5.3 **Differential non-linearity**. LSB values as a function of time. The standard deviation of LSB values holds a value of 6 % for a tested range of 20 ns. Within the 20 ns periodiocity the maximum LSB value is 17 % and the minimum is 0.03 %.

for all the TTM channels was assessed to be 8 % of the LSB, which corresponds to an RMS value of 3.44 ps - Fig. 5.4.

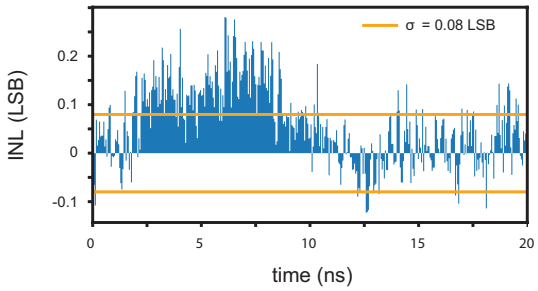

Figure 5.4 **Integral non-linearity**. LSB values as a function of time: the standard deviation of LSB values holds a value of 8 % for a tested range of 20 ns indicating working conditions for the TTM.

5.1.2 Single shot precision

The single-shot precision (SSP) of the BrightEyes-TTM TDCs was assessed by measuring repeatedly a constant start-stop time interval according to the SSP connections scheme depicted in blue in Fig. 5.1. A fixed-frequency (50 MHz) signal was fed into the SYNC channel and a synchronised second signal – with a fixed but tunable delay, thanks to SYLAP – into one of the input photon channels (Fig. 5.5 top pane). After accumulating several millions of sync-photon pairs, the start-stop time histogram was built (Fig. 5.5 lower pane). By fitting the start-stop time histogram with a Gaussian function, a SSP of σ = 30 ps was estimated (Appendix A). Notably, by tuning the delay between the two signals across the whole probe temporal range of the fine TDC (for this experiment 20 ns) similar precision values were observed (Fig. 5.6), confirming the excellent performances of the fine TTM architecture.

The same SPP experiment was carried out for all the photon channels obtaining a similar precision (diagonal values on matrix of Fig. 5.7).

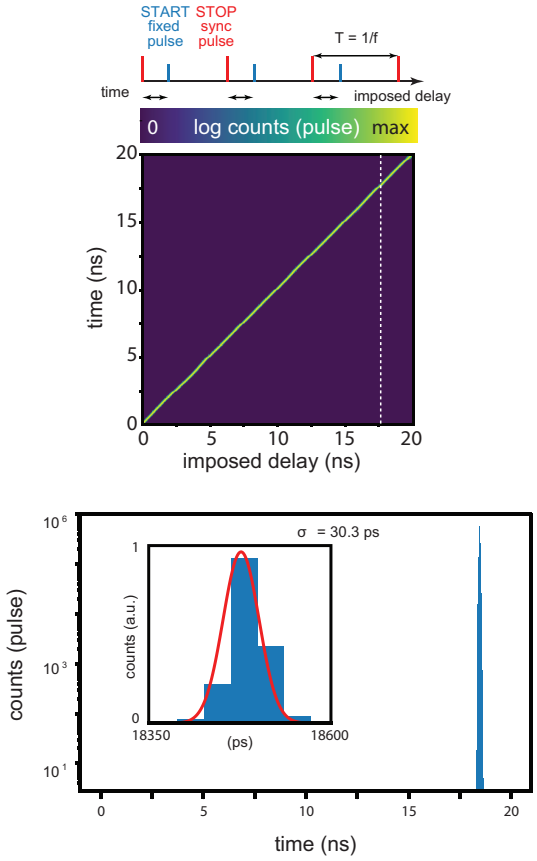

Figure 5.5 **Single-shot precision experiment**. Temporal schematic representation: a fixed frequency SYNC clock signal and a synchronised but delayed signal (top). Unified representation of the start-stop time histograms as a function of the imposed delay between the two signals (middle). Single start-stop time histogram for the delay denoted by the dotted white line in the middle pane (lower). The inset shows a magnification of the histogram for a selected temporal interval, superimposed with the Gaussian fit for SSP estimation (red line). All these measurements refer to channel #11 of the TTM.

5.1.3 Dual channel single shot precision

Having implemented a multi-channel time-tagging platform, when dealing with FLSM & FLIM applications, it could be of interest not only measuring the start-stop time between a sync-photon events, but also assessing the time of arrival of a photon on a specific channel (channel$_A$) in respect to the time of arrival of a second photon on a second channel (channel$_B$). Thus, to confirm the ability of the 21 channels to record photons in parallel, the SSP

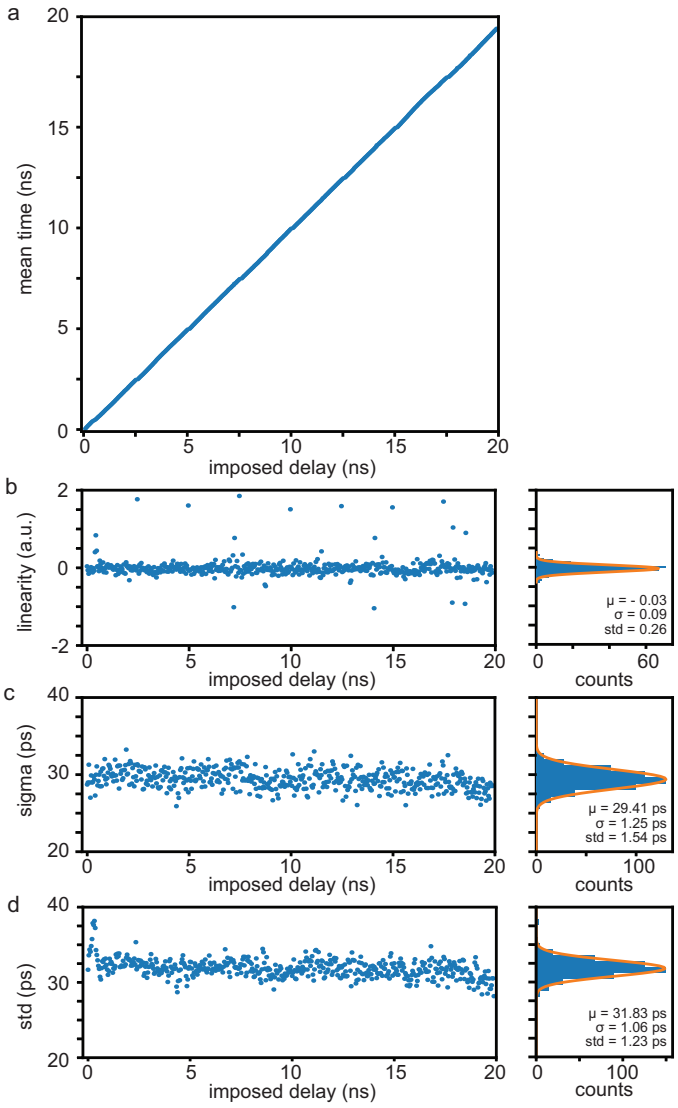

Figure 5.6 **Single shot precision measurement**. Considering the fitting model in Eq. A.3 in Appendix A: **a** the mean value μ as a function of the imposed delay. **b** The difference between the imposed delay and the mean value obtained as function of the imposed delay. **c** The standard deviation σ value as function of the imposed delay. **d** Calculated standard deviation of the start-stop time histogram as a function of the imposed delay. The similar values between the Gaussian standard deviation σ and the calculated standard deviation demonstrates the normal distribution of the start-stop time histogram. One the right-side of each graph the correspondent statistics is reported. All these measurements refer to channel #11 of the TTM.

experiment was repeated by feeding the same signal also into a second photon channel. In this case, the delays between all three signals (channel$_A$, channel$_B$, and SYNC) were kept fixed, and the TTM measured the delay between the two photon channel signals (Fig. 5.7

top pane). Similarly to the start-stop time histogram, a histogram that reports the elapsed time between the two photon channel signals (channel$_A$ vs. channel$_B$) was then built and fitted with a Gaussian function. The experiment was performed for all the possible channel pairs obtaining a precision values of $\sigma = 25 \div 35$ ps, depending on the channels pair (Fig. 5.7 bottom pane).

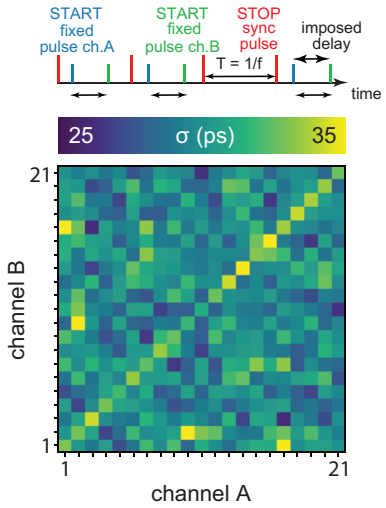

Figure 5.7 **Dual-channel single-shot precision experiment**. Temporal schematic representation: a fixed frequency SYNC clock signal and a pair of synchronised signals (channel$_A$ &. channel$_B$). The delays between all three signals are fixed (top). Jitter timing map for each pair of channels, i.e., error in the time-difference estimation between any two channels, measured as the standard deviation of a Gaussian fit of the error distribution. The diagonal of the map represents the sigma of the single-channel single-shot precision experiment (lower).

5.2 Integrating the BrightEyes-TTM into a FLSM setup

As the BrightEyes-TTM works as a passive plug-n-play device it can be integrated in any pre-existent setup. Thus, in order to validate the TDC architecture with actual fluorescence measurements, it was incorporated into a custom-built (pre-existent) single-photon laser scanning microscope equipped with a bi-dimensional 21-element SPAD array detector and a picosecond pulsed diode laser source (488 nm LDH Series Picosecond Laser Diode Head & Sepia PDL 828, Multichannel Picosecond Diode Laser Driver, PicoQuant, Berlin, Germany) (Fig. 5.8).

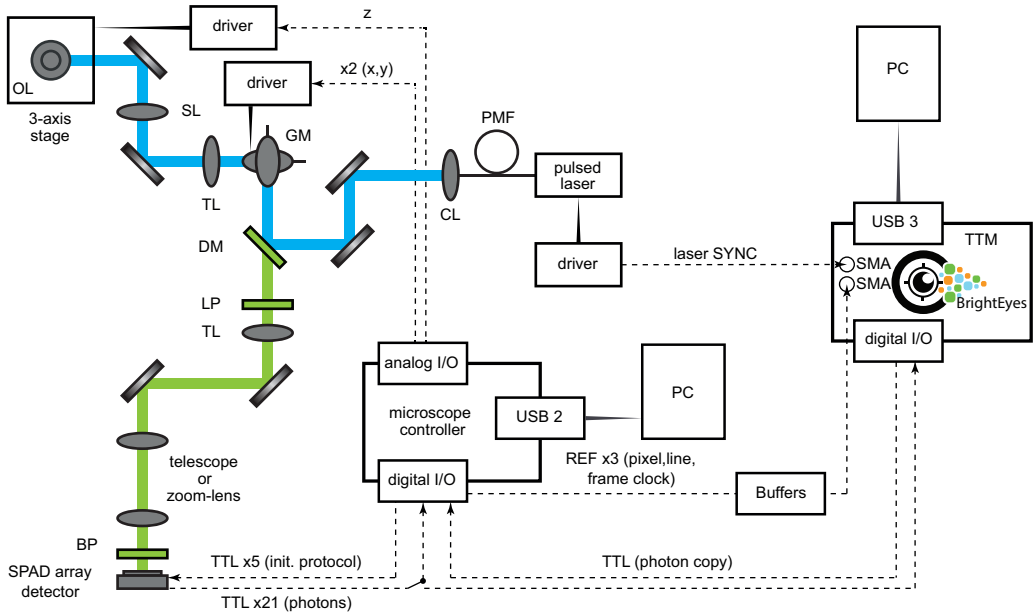

Figure 5.8 **Single-photon laser scanning microscope**. Schematic representation of the optical architecture and the data-acquisition and control system. Digital and analogue single-cable connections are represented by dashed lines. DM: dichroic mirror, GM: galvanometric scan mirrors, SL: scan lens, TL:tube lens, OL: objective lens, LP: long pass filter, BP: band pass filter, CL: collimating lens, PMF: polarising maintaining fibre. The pixel, line, and frame reference signals and the laser sync signal are plugged directly to the FPGA-development board using the SMA user I/Os, whilst the photon signals are plugged to the board by using the I/Os daughter card. The board duplicates the photon signal from the central element of the SPAD array detector and send to the microscope controller via a TTL digital signal.

5.3 Instrument response function and fluorescence decay measurements

Once integrated into the FLSM setup, in order to validate the BrightEyes-TTM performances, a quenched solution of fluorescein in water, saturated with potassium iodide was used to measure the impulse-response function (IRF) of the system (205). The computed FWHM of the IRF was ~240 ps. This relatively large value, in respect with SSP measurement, is due to the convolution of the single-shot response ($\sim$ 30 ps) with the laser pulse-width ($>$ 100 ps), the SPAD photon jitters ($\sim$ 120 ps) and the jitters/dispersion introduced by the optical system (Fig. 5.9). The IRF measured with the BrightEyes-TTM was compared with the IRF acquired with a DPC-230 multi-channel commercial time-tagging card (Becker&Hickl, Berlin, Germany). Notably, because of the poor time resolution (164 ps from the data-sheet),

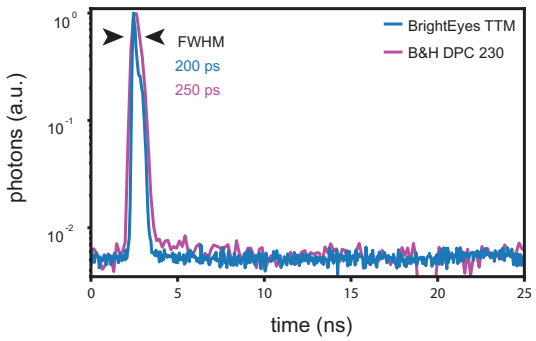

Figure 5.9 **Instrument response function**. Normalised impulse response functions (and FWHM values) for the BrightEyes-TTM and the B&H DPC-230 multi-channel card. The IRF represents the response of the whole architecture (microscope and DAQ) to a fast (sub-nanosecond) fluorescent emission.

the DPC-230 is not able to reveal the typical cross-talk effect of the SPAD array detector (2), which is visible in the BrightEyes-TTM as an additional bump (Fig. 5.9).

The two time-tagging systems were then further compared, by measuring the decay distributions of a pure solution of fluorescein dissolved in water. The two TCSPC histograms show very similar shapes, which is confirmed by fitting them with a single exponential decay model (τ_{fl} = 3.97 ± 0.04 ns and τ_{fl} = 3.99 ± 0.01 ns, for the BrightEyes-TTM and the DPC-230, respectively) (Fig. 5.10).

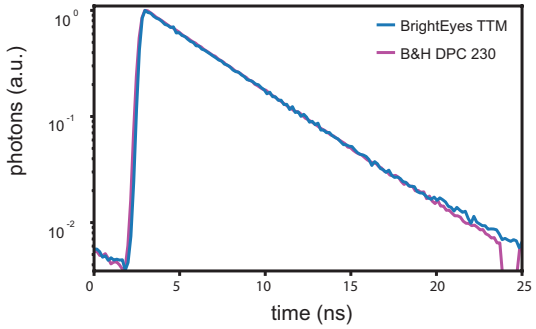

Figure 5.10 **Fluorescence decay histogram of fluorescein**. Normalised fluorescence decay histogram (i.e., TCSPC histogram) for a fluorescein-water solution measured with the BrightEyes-TTM and the DPC-230 card.

5.4 BrighEyes-TTM validation tests

To test the ability of the BrightEyes-TTM of reconstructiong the TCSPC histogram for different fluorescence lifetime values, the decay distributions of quenched fluorescein solution

for increasing concentrations of potassium iodide were measured (Fig. 5.11 left). The higher the potassium iodide concentration is, the higher the quenching will be, thus the longer the measurement time needed to accumulate good photon statistic. For this reason, in Fig. 5.11 it is possible to appreciate how the dark-noise (which appears as an uncorrelated background in the TCSPC histogram) increases with increasing quencher concentration. The same effect appears on the phasor-plot (shown in Fig. 5.11 right): because the decays follow a single-exponential function, all points, regardless of the concentration, should lie on the universal semicircle. However, the uncorrelated background shifts the points towards the origin because a lower signal-to-background ratio yields an higher demodulation (Fig. 5.11 right).

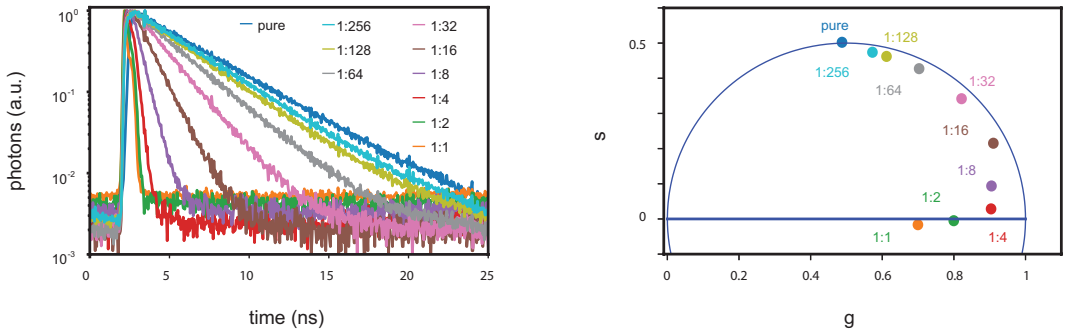

Figure 5.11 **Fluorescence decay curves for quenched fluorescein solution for increasing concentrations of potassium iodide**. Normalised fluorescence lifetime decay histograms of quenched fluorescein solutions for increasing concentrations of quencher (potassium iodide) (left), phasor representation of quenched fluorescein solutions (right). All single-channel measurements were done with TTM channel #11, which received the photon signal from the central element of the SPAD array detector.

5.5 Temporal range measurements

To demonstrate the ability of the BrightEyes-TTM to work at different temporal ranges, we repeated the fluorescein measurements for different laser frequencies (80, 40, 20, 10 and 5 MHz yielding ranges of 12.5, 25, 50 and 100 ns respectively). The TCSPC histograms do not show relevant differences (Fig. 5.12) thus confirming the flexibility of the developed architecture in working with different laser sync rates.

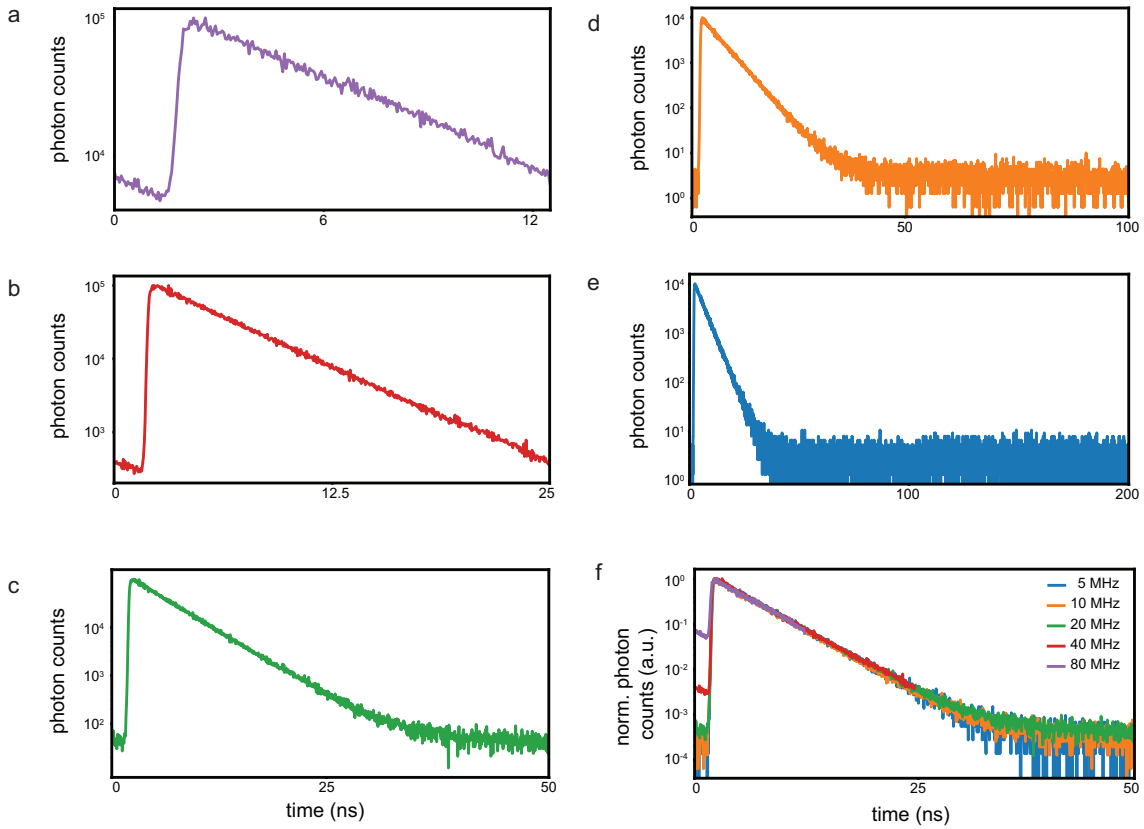

Figure 5.12 **TCSPC histograms of pure fluorescein-water solution for different temporal ranges (a-e) and comparison of the obtained results (f)**. Fluorescence decay histogram, photon counts as a function of time, of a fluorescein-water solution for **a** 80 MHz, **b** 40 MHz, **c** 20 MHz, **d** 10 MHz and **e** 5 MHz laser repetition rates. **f** cumulative view, normalized photon counts versus time, of the reconstructed fluorescein decay histograms for all the probed temporal ranges. 40 MHz and 80 MHz curves show an higher offset when compared with 5, 10, and 20 MHz plots, due to a not complete relaxation of the fluorescein molecules from the excited state that occurs with shorter laser excitation periods. All these measurements refer to channel #11 of the TTM.

5.6 TCSPC histogram binning

As specified in Chapter 4.3.1, since the sliding-scale differential method employed to implement the TDC was used in combination with an off-line (post-acquisition) bin-by-bin calibration procedure (Chapter 2.4.2), the user can arbitrary choose the bin width of the start-stop (TCSPC) histogram (Fig. 5.13). In this PhD work the same bin width value, i.e., 43 ps was used for the code density test, and for all the experimental measurements. 43 ps is the average time-width value calculated for all the deployed delay lines in the BrightEyes-TTM architecture (Fig. 5.14).

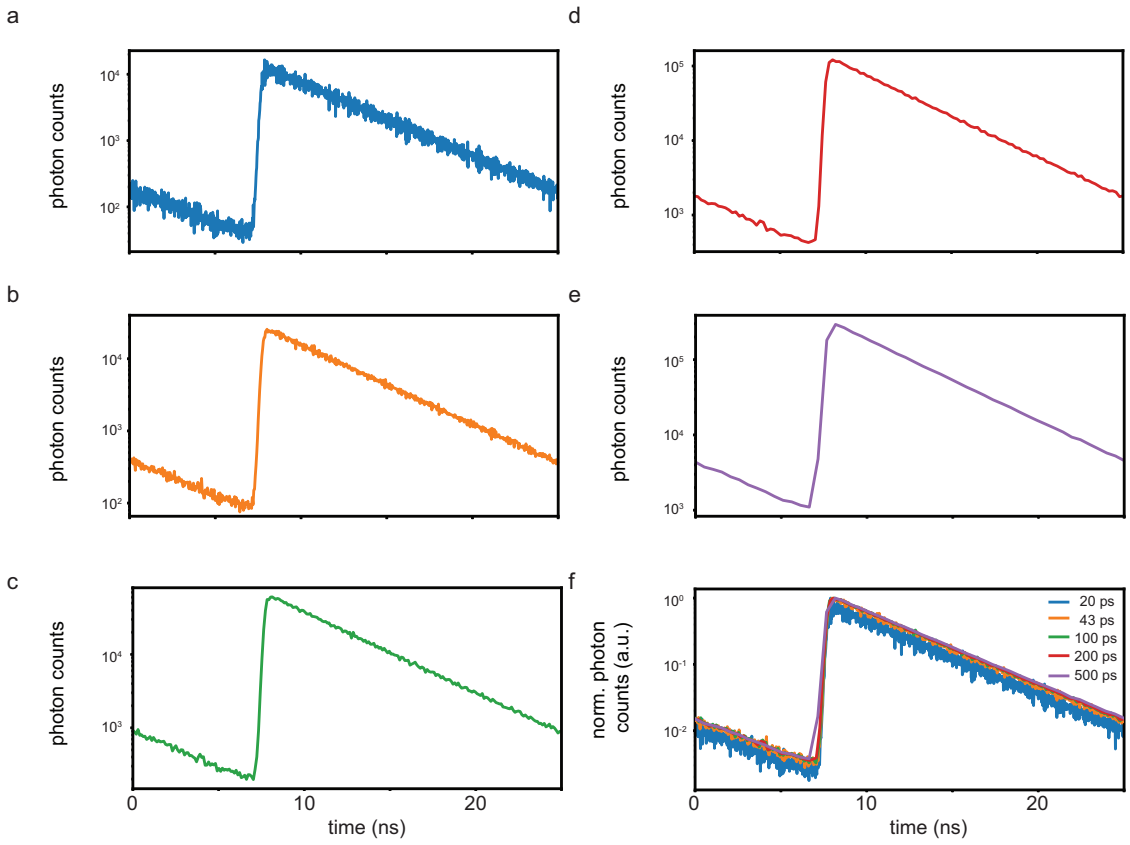

Figure 5.13 **TCSCP histograms of a fluorescein solution reconstructed using different time bin widths (a-e) and superposition of the obtained results (f)**. Fluorescence decay histogram, photon counts as a function of time, of a fluorescein-water solution reconstructed with bin-width of **a** 20 ps, **b** 43 ps, **c** 100 ps, **d** 200 ps and **e** 500 ps. **f** cumulative view, normalized photon counts versus time, of the reconstructed fluorescein decay histograms for all the different tested time bin-widths. The smaller the time bin-width the higher the SNR, for this reason the 20 ps curve shows a noisier profile when compared to 43, 100, 200 and 500 ps curves, due to an undersampling of the actual bin-width for the reconstructed TCSPC histograms. All these measurements refer to channel #11 of the TTM.

5.7 Conclusions

The BrightEyes-TTM showed (i) linearity performances (ii) SSP precision, (iii) dual SPP precision that allows for the TTM to be employed in ToF measurement experiments. Moreover, when connected to a single-photon LSM setup, the BrightEyes-TTM is able to accomplish IRF and fluorescence decay measurements showing results that overlap with those obtained with a commercial multi-channel DAQ card, proving also great versatility when dealing with different time measurement ranges. In summary, the BrightEyes-TTM performances are

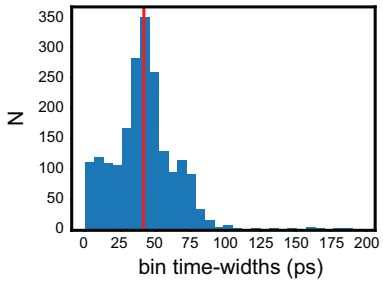

Figure 5.14 **Histogram of the time-bin widths (w_i) of all the deployed TDLs in the TTM architecture**. Cumulative histogram, number (N) as a function of time-bin widths, of all the calculated w_i for all the TTM delay lines. The histogram mean value (red line) is w_{avg} = 42 ± 25 ps.

reported in Table 5.1. The next chapter reports the imaging and spectroscopy results of the BrightEyes-TTM when integrated into a FLSM equipped with a SPAD array detector.

Table 5.1 **BrightEyes-TTM specifications**

Single shot precision*	30 ps
Time bin width	user defined (default 43 ps)
Time range**	not limited by hardware
Maximum laser sync rate	80MHz
Dead time	1/240 Mhz = ~ 4.2 ns
Differential non-linearity	~ 6 % RMS
*	Gaussian fitting sigma value
**	Tested at 200 ns (5 MHz), 100 ns (10 MHz), 50 ns (20 MHz), 25 ns (40 MHz), 12.5 ns (80 MHz)

Chapter 6

Fluorescence lifetime image scanning microscopy with BrightEyes-TTM

DAQ modules are capable of acquiring data at high speeds. The BrightEyes-TTM, which can acquire data from many channels in parallel, is therefore ideally suited to be integrated into a FLSM equipped with a SPAD array detector to perform fluorescence imaging and spectroscopy on biological systems. This chapter reports, first, the data processing in order to perform imaging with the BrightEyes-TTM and, second, some results obtained by the BrightEyes-TTM in the context of fluorescence imaging and spectroscopy, on fluorescent beads samples and on biological samples.

6.1 Data processing for imaging

As with all FLSM imaging techniques, FLISM requires the fluorescence photons to be recorded in synchronisation with the scanning system. Such synchronisation is commonly obtained by measuring the photon arrival times with respect to the imaging clock signals typically provided by the scanning system. Since the scanning synchronisation does not require high precision, the pixel, line and frame clocks are connected to the reference (REF) channels of the TTM, which use a digital coarse counter TDC with nanosecond precision ($\sim$4.2 ns).

Thanks to the synchronisation signals, each acquired image is a 4D photon-counting $(ch, x, y, \Delta t)$ data set. In fact, for each 2D position of the scanning laser beam (given by the dimensions (x, y), in all these imaging experiments a single frame was recorded), ch is the dimension describing the element of the SPAD array detector (Fig. 6.1, top), and time (Δt) is

the dimension of the TCSPC histogram (Fig. 6.1, middle) i.e. the time difference between the photon and the laser sync events (Tables in Appendix D.1).

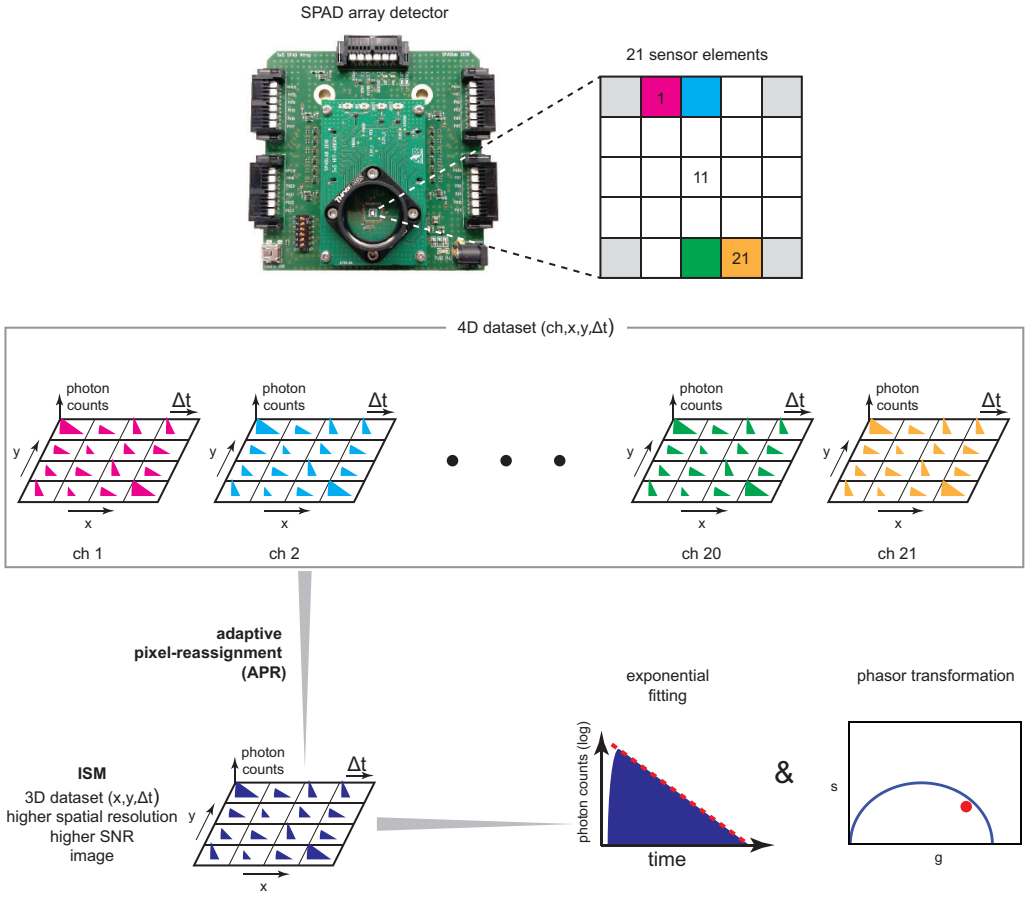

Figure 6.1 **4D imaging dataset processing**. By sampling the photon flux coming from the 21 elements of the SPAD array in combination with the REFs signals, the BrightEyes-TTM is able to reconstruct, in a post-processing phase, a 4D photon dataset $(ch, x, y, \Delta t)$. The 4D dataset is transformed into a 3D $(x, y, \Delta t)$ ISM intensity image which is fitted with an exponential model and phasor-transformed in order to extract the lifetime information.

This configuration enables several fluorescence imaging (and spectroscopy) techniques. For example, the photon spatial information (x, y) of all channels of the SPAD array detector (ch) can be combined with the adaptive pixel-reassignment (APR) algorithm in order to achieve super-resolved ISM images (33; 66). Furthermore, the temporal information (Δt) can be used to quantify the fluorescence lifetime for each pixel of the image, leading to super-resolved FLIM and phasor analysis (Fig. 6.1, bottom). In addition, fluorescence lifetime fluctuation spectroscopy (FLFS), a new family of fluorescence spectroscopy techniques, can be implemented, further opening up the possibilities to analyze the enriched dataset provided by the BrightEyes-TTM on a LSM with a SPAD array detector.

The huge amount of data that is collected and processed by the BrightEyes-TTM makes real-time plotting and analysis challenging. In order to obtain a real-time intensity-based image to use it as a guideline during FLISM experiments, one of the BrightEyes-TTM detection channels (here, the photon channel of the central element of the SPAD array) was duplicated (TTL photon copy) and sent to the control system of the microscope, as shown in Fig. 5.8). This approach, having the SPAD array detector connected to both the TTM and to the microscope controlling system (based on a National Instrument (NI) card), allows the simultaneous reconstruction of the same image on both the BrightEyes-TTM and the NI acquisition card. Thus, we can further validate the imaging capabilities of the BrightEyes-TTM system by comparing it with the well-tested NI acquisition card (206). For this, we imaged α-tubulin immunolabelled Hela cells with both systems. Fig. 6.2 (a) shows the intensity-based confocal image acquired by the BrightEyes-TTM, while Fig. 6.2 (b) shows the intensity-based confocal image acquired with the NI acquisition card. Both images

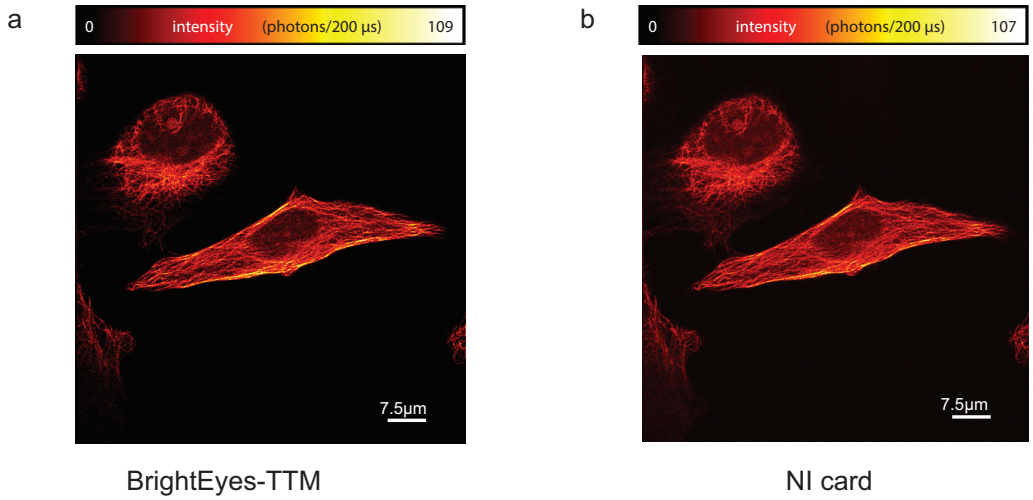

Figure 6.2 **Imaging with the off-line BrightEyes-TTM and the real-time NI-DAQ systems**. Side-by-side comparison of CLSM (0.2 AU) images obtained with the TTM (**a**) and the NI card (**b**). The images, which represent a α-tubulin immunolabelled Hela cell, were collected simultaneously: the BrightEyes-TTM received the signal from the central element of the SPAD array detector, duplicated it, and sent one copy to the NI-DAQ system. Scale bars 7.5 μm.

show the same features, confirming thus the validity of the BrightEyes-TTM to reliably acquire intensity-based images of biological samples.

To reconstruct the super-resolved intensity images with the BrightEyes-TTM data, the 4D dataset is first integrated $(ch, x, y, \Delta t)$ along the Δt dimension, after which phase-correlation registration based on the adaptive-pixel reassignment (APR-ISM) method (33; 66; 207) is

applied to register all the *ch* images with respect to the central channel. After reassignment, all images are simply summed to obtain one super-resolved intensity image.

However, thanks to its timing precision, the data acquired with the BrightEyes-TTM on SPAD array detectors can do more than only imaging the fluorescence intensity. E.g. in FLISM, super-resolved APR-ISM is combined with fluorescence lifetime imaging. To obtain the lifetime-based ISM image, starting from the 4D dataset $(ch, x, y, \Delta t)$, for each Δt value the same shift-vector fingerprint to shift the relative 2D image is used, and the result is integrated along the *ch* dimension. Finally, the resulting 3D dataset $(x, y, \Delta t)$ is imported into the FLIMJ analysis plug-in software for IMAGEJ (208) to obtain the τ_{fl} map (here, obtained by fitting the images with a single-exponential decay model) and thus, the final FLISM image.

Alternatively, phasor analysis can also be performed on the same 3D ISM dataset by computing the phasor coordinates (g, s) using cosine and sine summations (76; 209). In order to avoid artefacts in the phasor plot calculation the *MOD* mathematical operation was carried out on the TCSPC histograms with the laser repetition period value (209) before computing the g, s coordinates. Phasor plot analysis measurements were referenced to a fluorescein-water solution which was used to phasor-calibrate the entire acquisition system and thus accounting for the instrument response function of the complete acquisition setup (microscope, detector and TTM).

Besides imaging, the same BrightEyes-TTM can also be used to measure sample dynamics through fluorescence fluctuation spectroscopy measurements (206). Compared to single-element fluorescence correlation spectroscopy, the spatial information coming from the different positions of the detector elements in the image plane reveals additional information on the molecular dynamics at play, e.g., the diffusion modality or anisotropy in the diffusion dynamics can be quantified with FFS. In addition, having access to the arrival time of each photon opens up possibilities to correlate the diffusion mode of the investigated molecules with their microenvironment or structural changes. For example, by using probes whose lifetime depends on the specific environment of the probe or on its molecular structure, measuring variations in the fluorescence lifetime during the FFS measurement can be linked to changes in the microenvironment or in the molecular structure and directly correlated to the molecular mobility.

In the following sections, some examples of applications of the BrightEyes-TTM are presented.

6.1.1 BrightEyes-TTM applications

Fluorescent nanobeads

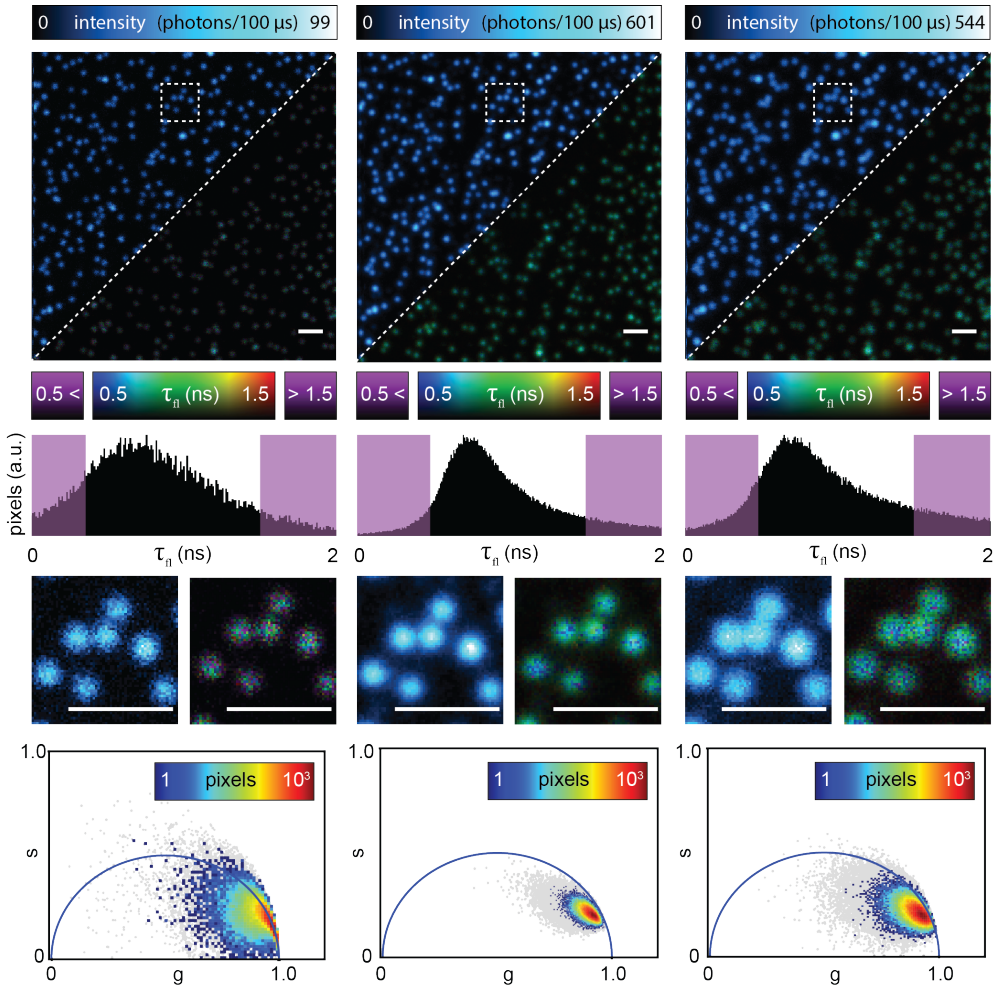

Figure 6.3 **Imaging and FLIM analysis of 100 nm fluorescent nanobeads**. Side-by-side comparison (top row) of CLSM (left, pinhole 0.2 AU), adaptive pixel-reassignment ISM (center), and FLSM (right, pinhole 1.4). Each imaging modality shows both the intensity-based image (top-left corner) and the lifetime image (bottom-right corner). A bi-dimensional look-up-table is able to represent in the lifetime images both the intensity values (i.e., photon counts) and the lifetime values (i.e., τ_{fl}). Histogram distributions of the imaging lifetimes values (middle-top row), number of pixels versus lifetime values, - in violet lifetime values which falls out of the selected lifetime representation interval. The lifetime images report in violet the pixels whose lifetime belong to this interval. Zoomed regions in the white-dash boxes, re-normalised to the maximum and minimum intensity values (middle-bottom). Pixel intensity thresholded phasor plots (5% and 10% thresholds respectively in gray and color). Phasor-plots were referenced using a fluorescein calibration sample. Scale bars 2 μm.

In order to fully test the optical enhancement of the APR-ISM reconstruction algorithm with the BrightEyes-TTM, a sample of fixed 100 nm fluorescent nanobeads (Appendix C) was imaged with the SPAD array detector. In this case, a 40 MHz laser repetition rate and 100 ns of detector hold-off were used. The side-by-side comparison of the intensity-based images clearly shows the optical resolution enhancement of ISM with respect to conventional FLSM imaging and the higher SNR with respect to CLSM imaging, shown on the top row of Fig. 6.3 and, more clearly, in the zoomed region. In the context of FLISM, higher SNRs lead to a higher lifetime precision, as depicted by the lifetime histograms and the phasor plots in the bottom panes of Fig. 6.3.The lifetimes value were calculated, as explained in the previous section, by either fitting the TCSPC histograms with a single-component exponential decay, or by phasor-plotting.

Vimentin cytoskeleton network in fixed cells

To further test the resolution improvement and the flexibility of the BrightEyes-TTM platform, a sample of fixed mammalian cells with stained vimentin cytoskeleton network was imaged with the same settings for the SPAD array detector as for the nanobeads sample (Appendix C). Vimentin is a protein of the family of intermediate filaments and is, together with microtubules and actin filaments, a component of the cellular cytoskeletal network. The cytoskeletal network contributes to several processes in biological cells, as it helps, for example, in maintaining cell shape and in providing mechanical resistance. Cytoskeletal filaments, due to their geometry, are often used in the microscopy field as "markers" to compare optical resolution and SNR between different optical approaches.

Similarly to the fluorescent beads, the dataset was processed with the APR-ISM algorithm to improve the resolution, and with both the phasor approach and TCSPC histogram fitting approach, to quantify the fluorescence lifetime. As expected, equivalent findings are found also in the case of biological samples. The comparison of the intensity-based images clearly shows the optical resolution enhancement of ISM with respect to conventional FLSM imaging and higher SNR with respect to CLSM imaging (Fig. 6.4, top row). Also here, the higher SNR of FLISM yields a higher lifetime estimation precision, as shown by the lifetime histograms and phasor plots of Fig. 6.4. This example is a further confirmation of both the effectiveness and the capability of the BrightEyes-TTM in dealing with FLISM and fluorescence intensity-based imaging.

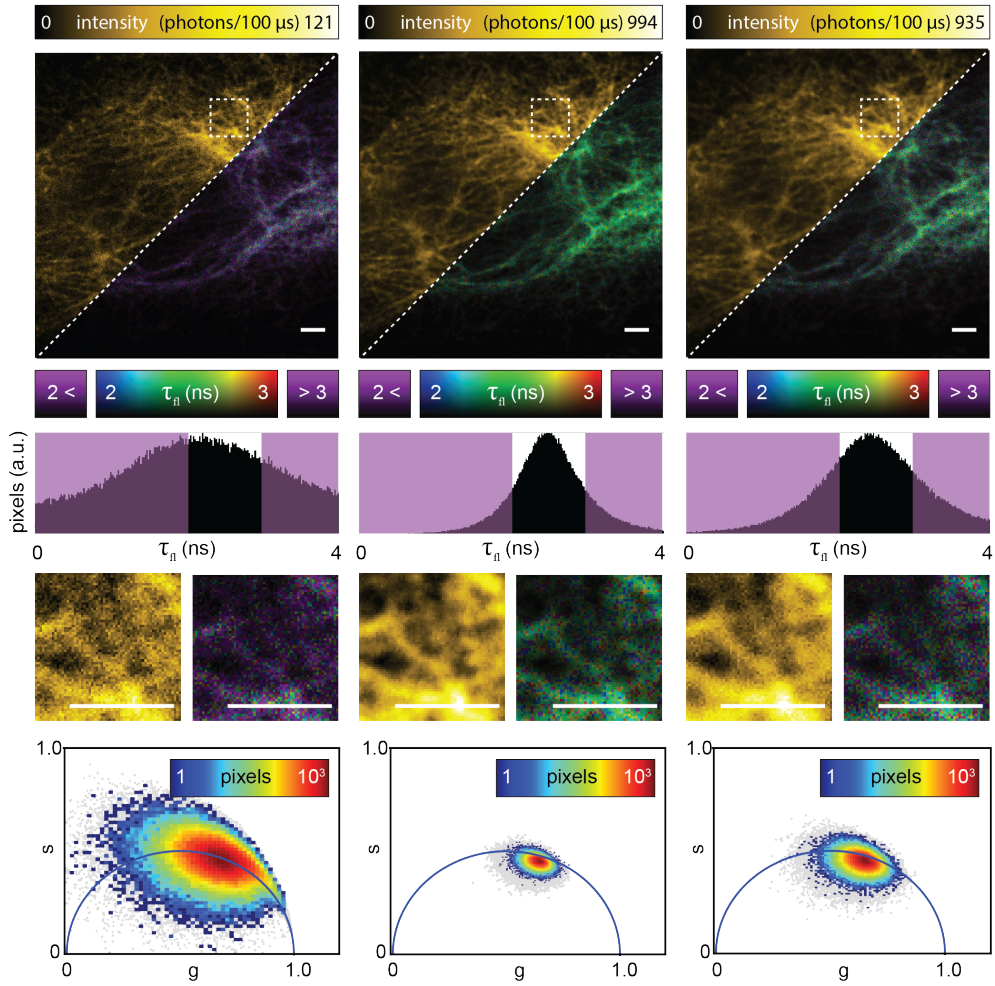

Figure 6.4 **Imaging and analysis of fluorescent labelled vimentin in fixed cell**. Side-by-side comparison (top row) of CLSM (left, pinhole 0.2 AU), adaptive pixel-reassignment ISM (center), and FLSM (right, pinhole 1.4). Each imaging modality shows both the intensity-based image (top-left corner) and the lifetime image (bottom-right corner). A bi-dimensional look-up-table represents both the lifetime values and the intensity values (i.e., photon counts) and the excited-state lifetime values (i.e., τ_{fl}). The intensity-based images integrate the relative 3D data $(x, y, \Delta t)$ along the start-stop time dimension Δt. The lifetime-based images obtains the excited-state lifetime values by fitting the TCSPC histogram of each pixel with a single-exponential decay model. Histogram distributions of the imaging lifetimes values (middle-top row), number of pixels versus lifetime values, - in violet lifetime values which fall out of the selected lifetime representation interval. The lifetime images report in violet the pixels whose lifetime belongs to this interval. Zoomed regions in the white-dash boxes, re-normalised to the maximum and minimum intensity values (middle-bottom). Pixel intensity thresholded phasor plots (5% and 10% thresholds respectively in gray and color). Phasor-plots were referenced using a fluorescein calibration sample. Scale bars 2 μm.

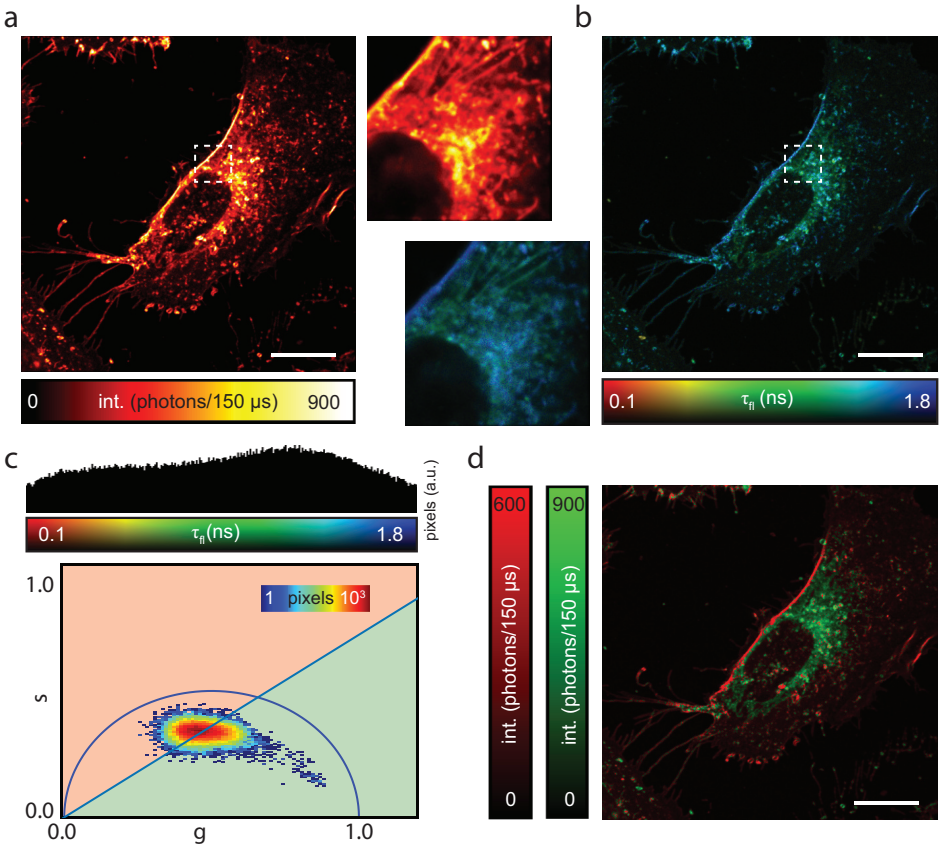

Figure 6.5 **FLISM imaging of Hela cells stained with ANEP. a,b** Intensity-based ISM image (left) and lifetime-based image (b) of live HeLa cells stained with the polarity-sensitive fluorescent probe di-4-ANEPPDHQ. Side images depict the areas within the dashed white boxes. **c** Histogram distribution of the imaging lifetimes values (top): number of pixels versus lifetime values. Pixel intensity thresholded phasor plots (bottom): number of pixel versus the polar coordinate (10% thresholds). **d** Phasor-based segmentation. Images are obtained by back-projection of the points within the red (long lifetime, ordered membrane) and green (short lifetime, disordered membrane) semi-planes in the phasor-plot (c). Scale bars 5 μm.

Hela cells stained with ANEP

To demonstrate the importance of the BrightEyes-TTM in a realistic biological application, we used the platform to perform FLISM on living cells to resolve their complex microenvironmental variation. In particular, the use of the fluorescent polarity-sensitive membrane dye di-4-ANEPPDHQ allows monitoring the ordered/disordered-phase membrane domains (66; 210); an important biophysical property which regulates many cellular membrane processes, such as cell division and cell movement. While the intensity-based images don't show any difference between the two lipid-phase of the membrane (Fig. 6.5 a), the fluorescence

lifetime allows use to directly probe changes in the cellular microenvironment. While the fluorescent dyes in the plasma membrane show relatively long fluorescence lifetimes, denoting a high membrane order, dye molecules in the intracellular membrane show a shorter fluorescence lifetime, denoting a high membrane disorder (Fig. 6.5 d).The difference between the two microenvironmental conditions is further highlighted by implementing a phasor-based segmentation 6.5 c,d). The images were acquired using an 80 MHz laser repetition rate and a 50 ns SPAD array detector hold-off timing.

6.2 Conclusions

Thanks to the versatility of the BrightEyes-TTM, fluorescent-labelled samples can be imaged by simply connecting the REFs signal to the pixel,line and frame clocks of a pre-existent microscopy setup. This allows every CLSM with a single photon detector to be upgraded into a system able to perform high timing precision fluorescence spectroscopy and imaging techniques. In particular, here, the usage of the BrightEyes-TTM with the SPAD array detector, allows us to combine the high temporal-precision of the DAQ platform with the enriched-information datasets provided by the SPAD array detector. We showed some of the microscopy techniques granted by the BrightEyes-TTM. We performed FLISM, proving the improvement in resolution and SNR granted by the platform combined with our detector, on both a fluorescent nanobead and a fixed-cell sample. Moreover, we validated the BrightEyes-TTM in the contest of microenvironment-sensing for cellular application, by measuring the fluorescence lifetime of living cells stained with a polarity-sensitive membrane. Indeed, BrightEyes-TTM proved its versatility in dealing with fluorescence imaging as well as fluorescence lifetime assessment with various and different types of samples. While in this work, the BrightEyes-TTM has been mainly employed in imaging, a first proof-of-principle FFS experiment, in combination with fluorescence lifetime, has been already performed (41). Combining fluorescence lifetime with fluorescence fluctuation spectroscopy provides information about molecular dynamics, granted by the FFS analysis, linked with structural-functional information, granted by the lifetime. We are positive that the introduction of the BrightEyes-TTM will allow biological laboratory to perform several microscopy and spectroscopy techniques, helping to answer new questions.

Chapter 7

Conclusions and future perspectives for the BrightEyes-TTM

7.1 Conclusions

During this 3-year-long PhD project the BrightEyes time-tagging architecture was conceived, designed, implemented and fully tested both on the bench and in a relevant spectroscopy & microscopy environment. The TTM platform proved its functioning demonstrating a very high timing precision ($\sim$ 30 ps) combined with multi-channel capabilities (21 photon input channels in the current implementation) within a single-board and standalone electronic device. In addition, the TTM was assembled using commercial available electronic parts and programmed with license-free coding languages thus ensuring the open-source feasibility of the time-tagging architecture.

Indeed, as output of the PhD work, the BrightEyes-TTM was released as a fully open-source project with two aims. The principal aim is to give to any microscopy and life science laboratory the possibility to implement and further develop single-photon-based time-resolved microscopy techniques. The second aim is to trigger the interest of the microscopy community, and establish the BrigthEyes-TTM as a new standard for single-photon FLSM and FLIM experiments.

I expect the BrightEyes-TTM main fall-out to go beyond current implementation state and applications usage. The TTM can in fact, potentially collect single-photons in synchronisation with a plethora of many different external devices that could potentially encode in the photon other information content, directly on indirectly. For example, polarisation modulators and/or analysers can help tagging photons with an excitation and emission polarisation signature.

Acoustic tunable filters and spectrometers can provide an excitation and emission wavelength signature, thus significantly extending the field of usage of the TTM device.

Code availability

The FPGA firmware, already compiled as a .bit file and ready to be downloaded in the KC705, as well as the VHDL/Verilog source code for implementing the BrightEyes-TTM on the Xilinx KC705 evaluation board, the data-receiver software to install on the personal computer, and the operational softwares for data processing, are accessible through the Vicidomini Lab GitHub repository https://github.com/VicidominiLab/BrightEyes-TTM.

Data availability

Raw time-tagged data that can be used with the processing softwares in the GitHub repository, are publicly available from Zenodo, https://doi.org/10.5281/zenodo.4912656.

7.2 Future prospects

The BrightEyes-TTM architecture was implemented on a FPGA, mounted on a readily and commercially available development kit, thus providing design flexibility and upgradability, and also allowing fast prototyping and testing of new potential BrightEyes-TTM release versions. For example, the current design accomodates only 21 input channels but, as the FPGA resources 7.1 Figure shows, less than ~50 % of the CLBs are effectively used allowing for future implementations to increase the number of input channels both for the TDLs and for the REFs signals. The new data transmission protocols allows indeed for handling and streaming out of the TTM architecture a maximum of 124 photon channel readings.

To the expenses of the FPGA occupation, it would also be possible to access sub-CARRY4 signals further boosting the time resolution of the TDLs and together with it the timing precision of the entire architecture.

Moreover, for most of the typical fluorescence applications, it is unlikely of having multiple photon events within the same laser period. Thus, the size of the data that is transferred from the TTM to the PC could be significantly reduced by performing part of the data analysis and the reconstruction directly on the TTM, by leveraging a novel class of FPGAs equipped with a micro-processor. Indeed, many of FPGA manufacturers fit, within

the same silicon environment, multi-core ARM-based processors together with FPGAs. The combination of these two types of logic units allows for unprecedented signal processing as the FPGA is directly and physically joint with a micro-processor that can run an OS (operative system) and take care of data-processing and analysis in a real-time manner. Thus time-resolved data calibration and reconstruction (TCSPC as well as imaging) for instance, could potentially take place on the very same silicon chip without the need of streaming single-photons out of the TTM device to a secondary host-processing unit.

Focusing again on the current TTM implementation and talking about data transmission, another pursuable approach that can be followed would be to buffer the data on the peripheral DDR-RAM (double data rate synchronous-random access memory) memory block present onboard of the KC705 development card in order to avoid the fail-safe mode intervention, having the aim of prioritizing the REFs signals, rejecting incoming photons. Data could indeed be, at first, temporarily stored in a larger RAM memory that can keep up with high photon fluxes without the need of discarding single-photon information, and then, when the USB link is ready to transmit a stream, switched to the host-processing unit for further elaboration.

Another upgrade that I envisage is to stream data to an host-processing unit using the inbuilt PCI-e interface rather than USB 3.0 FX3 Cypress chip bridge. The PCI-e yields higher data bandwidth and transfer rate that could mitigate (or potentially void), together with the RAM data-buffering, the failsafe transmission mode.

Regarding future measurement types that can be pursued, thanks to the BrightEyes-TTM device, I envisage the use of the TTM for combining fluorescence lifetime into fluorescence fluctuation spectroscopy (FFS) (206) for studying fast biomolecular processes in living cells. Fluorescence fluctuation spectroscopy (FFS) is toolset of techniques that allow biomolecular dynamics, interactions, and structural changes to be measured in living cells analyzing both temporal and spatial fluctuations in the fluorescence intensity. Amongst FFS, fluorescence correlation spectroscpy (FCS) is one of the well-known and used approach to calculate the diffusion coefficient of molecules withing a living-cell environment. Having simultaneous access to the lifetime and to the diffusion information would yield the ability of correlating the mobility mode of the investigated molecules with its microenvironment or its structural changes. Moreover, by using specific probe constructs within the sample, TTM acquired-data can also be used for fluorescence resonance energy transfer (FRET) experiments (211), linking the variation of the fluorescence lifetime o changes in the microenvironment or in the molecular structure for tackling, for example, cancer diagnosis and treatment monitoring (212). Thanks to its multi-channel capabilities, the TTM could also be used in revealing

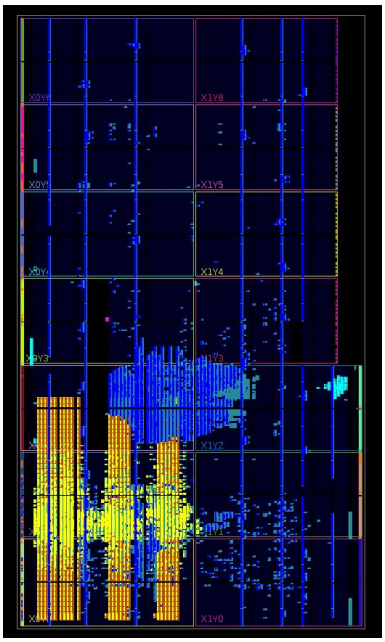

Figure 7.1 **FPGA resource utilisation**. 20% of slice look-up-tables (LUT) are used for the delay lines (TDLs) (orange) and thermomemer-to-binary encorders (t2b) in yellow; FIFO (98 % of inbuilt BRAM) and 5% of LUT for FX3 module in blue; SYLAP (only for test purpose) in light blue - 2% LUT.

and exploiting photons coincidences within photon anti-bunching measurements for further boosting, beyond ISM, the lateral resolution power of a LSM setup as demonstrated by (213; 214) using a technique called quantum-ISM (Q-ISM).

References

[1] Ilie, M. *et al.* Current and future applications of confocal laser scanning microscopy imaging in skin oncology (review). *Oncology Letters* **17**, 4102–4111 (2019).

[2] Buttafava, M. *et al.* SPAD-based asynchronous-readout array detectors for image-scanning microscopy. *Optica* **7**, 755 (2020).

[3] Zhang, C., Lindner, S., Antolovic, I., Wolf, M. & Charbon, E. A CMOS SPAD imager with collision detection and 128 dynamically reallocating TDCs for single-photon counting and 3d time-of-flight imaging. *Sensors* **18**, 4016 (2018).

[4] Williams, G. O. S. *et al.* Full spectrum fluorescence lifetime imaging with 0.5 nm spectral and 50 ps temporal resolution. *Nature Communications* **12** (2021).

[5] Bohn, S. *et al.* Multiwavelength confocal laser scanning microscopy of the cornea **11**, 5689 (2020).

[6] Zhang, Y. *et al.* A new multichannel spectral imaging laser scanning confocal microscope **2013**, 1–8 (2013).

[7] Callegari, F. *et al.* Polarization label-free microscopy imaging of biological samples by exploiting the zeeman laser emission **9** (2021).

[8] Sandison, D. R., Williams, R. M., Wells, K. S., Strickler, J. & Webb, W. W. Quantitative fluorescence confocal laser scanning microscopy (CLSM). 39–53 (Springer US, 1995).

[9] Boi, S. A method of quantitative measurement of fluorescence intensity by confocal laser scanning microscopy. *Journal of Computer-Assisted Microscopy* **10**, 163–166 (1998).

[10] Renz, M. Fluorescence microscopy-a historical and technical perspective **83**, 767–779 (2013).

[11] Ceredig, R. George gabriel stokes as a biologist **378**, 20200105 (2020).

[12] Ploem, J. S. Laser scanning fluorescence microscopy **26**, 3226 (1987).

[13] McConnell, G. Confocal laser scanning fluorescence microscopy with a visible continuum source **12**, 2844 (2004).

[14] Hansen, E. W., Zelten, J. & Wiseman, B. A. Laser scanning fluorescence microscope (SPIE, 1988).

[15] Paddock, S. W. Confocal laser scanning microscopy. *BioTechniques* **27**, 992–1004 (1999).

[16] Schneckenburger, H. & Richter, V. Laser scanning versus wide-field—choosing the appropriate microscope in life sciences **11**, 733 (2021).

[17] Kihm, K. D. Confocal laser scanning microscopy (CLSM). 55–79 (Springer Berlin Heidelberg, 2011).

[18] Sanderson, M. J., Smith, I., Parker, I. & Bootman, M. D. Fluorescence microscopy. *Cold Spring Harbor Protocols* **2014**, 1042–1065 (2014).

[19] Minsky. Microscopy apparatus (1957).

[20] Sheppard, C. & Choudhury, A. Image formation in the scanning microscope **24**, 1051–1073 (1977).

[21] Cristina, F., Vieira, L. & Bentley, M. V. L. B. Confocal laser scanning microscopy as a tool for the investigation of skin drug delivery systems and diagnosis of skin disorders (InTech, 2013).

[22] Paddock, S. W. Principles and practices of laser scanning confocal microscopy **16**, 127–150 (2000).

[23] Amos, W. & White, J. How the confocal laser scanning microscope entered biological research **95**, 335–342 (2003).

[24] Croix, C. M. S., Shand, S. H. & Watkins, S. C. Confocal microscopy: comparisons, applications, and problems **39**, S2–S5 (2005).

[25] Wang, L., Frei, M. S., Salim, A. & Johnsson, K. Small-molecule fluorescent probes for live-cell super-resolution microscopy **141**, 2770–2781 (2018).

[26] Waters, J. C. Accuracy and precision in quantitative fluorescence microscopy **185**, 1135–1148 (2009).

[27] Elliott, A. D. Confocal microscopy: Principles and modern practices **92** (2019).

[28] Abbe, E. Beiträge zur theorie des mikroskops und der mikroskopischen wahrnehmung **9**, 413–468 (1873).

[29] Sheppard, C. J., Gan, X., Gu, M. & Roy, M. Signal-to-noise in confocal microscopes. In Pawley, J. B. (ed.) *Handbook of Biological Confocal Microscopy*, 363–371 (Springer US, 1995).

[30] Müller, C. B. & Enderlein, J. Image scanning microscopy. *Phys. Rev. Lett.* **104**, 198101 (2010).

[31] Castello, M., Sheppard, C. J. R., Diaspro, A. & Vicidomini, G. Image scanning microscopy with a quadrant detector. *Opt. Lett.* **40**, 5355 (2015).

[32] WARD, E. & PAL, R. Image scanning microscopy: an overview **266**, 221–228 (2017).

[33] Sheppard, C. J. R. *et al.* Pixel reassignment in image scanning microscopy: a re-evaluation **37**, 154 (2019).

[34] Allen, J. S. The detection of single positive ions, electrons and photons by a secondary electron multiplier **55**, 966–971 (1939).

[35] Wiley, W. C. & Hendee, C. F. Electron multipliers utilizing continuous strip surfaces **9**, 103–106 (1962).

[36] Wen, L. *et al.* A quantitative approach to select PMTs for large detectors **947**, 162766 (2019).

[37] Giacomelli, M. G. Evaluation of silicon photomultipliers for multiphoton and laser scanning microscopy **24**, 1 (2019).

[38] Yokota, H., Fukasawa, A., Hirano, M. & Ide, T. Low-light photodetectors for fluorescence microscopy **11**, 2773 (2021).

[39] Gregor, I. & Enderlein, J. Image scanning microscopy. *Curr. Opin. Chem. Biol.* **51**, 74–83 (2019).

[40] Weisshart, K. The basic principle of airyscanning. Tech. Rep., Zeiss (2014).

[41] Slenders, E. *et al.* Cooled SPAD array detector for low light-dose fluorescence laser scanning microscopy **1**, 100025 (2021).

[42] Herman, B. *et al.* Fluorescence lifetime imaging microscopy. 491–507 (Springer Berlin Heidelberg, 1999).

[43] Berezin, M. Y. & Achilefu, S. Fluorescence lifetime measurements and biological imaging **110**, 2641–2684 (2010).

[44] Gerritsen, H. C., Sanders, R., Draaijer, A., Ince, C. & Levine, Y. K. Fluorescence lifetime imaging of oxygen in living cells **7**, 11–15 (1997).

[45] Hartmann, P., Ziegler, W., Holst, G. & Lübbers, D. W. Oxygen flux fluorescence lifetime imaging **38**, 110–115 (1997).

[46] Lin, H.-J., Herman, P. & Lakowicz, J. R. Fluorescence lifetime-resolved pH imaging of living cells **52A**, 77–89 (2003).

[47] Nakabayashi, T. *et al.* pH dependence of the fluorescence lifetime of enhanced yellow fluorescent protein in solution and cells **235**, 65–71 (2012).

[48] Ranjit, S., Malacrida, L., Stakic, M. & Gratton, E. Determination of the metabolic index using the fluorescence lifetime of free and bound nicotinamide adenine dinucleotide using the phasor approach **12** (2019).

[49] Suhling, K. *et al.* Fluorescence lifetime imaging for viscosity and diffusion measurements (SPIE, 2019).

[50] Gerritsen, H. C., Sanders, R. & Draaijer, A. Confocal fluorescence lifetime imaging of ion concentrations (SPIE, 1995).

[51] Benninger, R. K. P. *et al.* Quantitative 3d mapping of fluidic temperatures within microchannel networks using fluorescence lifetime imaging **78**, 2272–2278 (2006).

[52] Suhling, K. *et al.* Fluorescence lifetime imaging (FLIM): Basic concepts and some recent developments **27**, 3–40 (2015).

[53] Chang, C.-W., Sud, D. & Mycek, M.-A. Fluorescence lifetime imaging microscopy. 495–524 (Elsevier, 2007).

[54] Bastiaens, P. Fluorescence lifetime imaging microscopy: spatial resolution of biochemical processes in the cell **9**, 48–52 (1999).

[55] van Munster, E. B. & Gadella, T. W. J. Fluorescence lifetime imaging microscopy (FLIM). 143–175 (Springer Berlin Heidelberg, 2005).

[56] Borst, J. W. & Visser, A. J. W. G. Fluorescence lifetime imaging microscopy in life sciences **21**, 102002 (2010).

[57] Hatami, N. Fluorescence lifetime imaging microscopy for brain tumor image-guided surgery **15**, 056022 (2010).

[58] Unger, J. *et al.* Real-time diagnosis and visualization of tumor margins in excised breast specimens using fluorescence lifetime imaging and machine learning **11**, 1216 (2020).

[59] Zhou, T., Luo, T., Song, J. & Qu, J. Phasor–fluorescence lifetime imaging microscopy analysis to monitor intercellular drug release from a pH-sensitive polymeric nanocarrier **90**, 2170–2177 (2018).

[60] Jeong, S. *et al.* Time-resolved fluorescence microscopy with phasor analysis for visualizing multicomponent topical drug distribution within human skin **10** (2020).

[61] Rao, C., Patel, S. K., Prasad, A., Garg, N. & Nandi, C. K. Effect of protein corona on the drug delivery of carbogenic nanodots and their mapping by fluorescence lifetime imaging microscopy **4**, 5776–5785 (2021).

[62] Schuyler, R. & Isenberg, I. A monophoton fluorometer with energy discrimination **42**, 813–817 (1971).

[63] Charbon, E., Fishburn, M., Walker, R., Henderson, R. K. & Niclass, C. SPAD-based sensors. 11–38 (Springer Berlin Heidelberg, 2013).

[64] Hirvonen, L. M., Jiggins, S., Sergent, N., Zanda, G. & Suhling, K. Photon counting imaging with an electron-bombarded CCD: Towards a parallel-processing photoelectronic time-to-amplitude converter **85**, 123102 (2014).

[65] Gol'tsman, G. N. *et al.* Picosecond superconducting single-photon optical detector **79**, 705–707 (2001).

[66] Castello, M. *et al.* A robust and versatile platform for image scanning microscopy enabling super-resolution FLIM. *Nat. Methods* **16**, 175–178 (2019). (preprint on bioRxiv).

[67] Phillips, D., Drake, R., O'Connor, D. & Christensen, R. Time correlated single-photon counting (tcspc) using laser excitation **14**, 267–292 (1985).

[68] Becker, W. *et al.* Fluorescence lifetime imaging by time-correlated single-photon counting **63**, 58–66 (2003).

[69] Suhling, K., French, P. M. W. & Phillips, D. Time-resolved fluorescence microscopy **4**, 13 (2005).

[70] Feddersen, B. A., Piston, D. W. & Gratton, E. Digital parallel acquisition in frequency domain fluorimetry **60**, 2929–2936 (1989).

[71] Alcala, J. R., Yu, C. & Yeh, G. J. Digital phosphorimeter with frequency domain signal processing: Application to real-time fiber-optic oxygen sensing **64**, 1554–1560 (1993).

[72] Gratton, E. Fluorescence lifetime imaging for the two-photon microscope: time-domain and frequency-domain methods **8**, 381 (2003).

[73] Colyer, R. A., Lee, C. & Gratton, E. A novel fluorescence lifetime imaging system that optimizes photon efficiency. *Microscopy Research and Technique* **71**, 201–213 (2008).

[74] Moon, S., Park, B. & Won, Y. Digital implementation of TCSPC **45**, 1615 (2020).

[75] Datta, R., Heaster, T. M., Sharick, J. T., Gillette, A. A. & Skala, M. C. Fluorescence lifetime imaging microscopy: fundamentals and advances in instrumentation, analysis, and applications. *Journal of Biomedical Optics* **25**, 1 (2020).

[76] Digman, M. A., Caiolfa, V. R., Zamai, M. & Gratton, E. The phasor approach to fluorescence lifetime imaging analysis. *Biophys. J.* **94**, L14–L16 (2008).

[77] Gratton, E., Digman, M. A., Stringari, C. & Arnesano, C. Flim phasor analysis for time-domain and frequency-domain data **104**, 347a (2013).

[78] Arnesano, C., Santoro, Y. & Gratton, E. Digital parallel frequency-domain spectroscopy for tissue imaging **17**, 0960141 (2012).

[79] Scipioni, L., Rossetta, A., Tedeschi, G. & Gratton, E. Phasor s-FLIM: a new paradigm for fast and robust spectral fluorescence lifetime imaging. *Nat. Methods* (2021).

[80] Liu, X. *et al.* Fast fluorescence lifetime imaging techniques: A review on challenge and development. *Journal of Innovative Optical Health Sciences* **12**, 1930003 (2019).

[81] Trinh, A. L. & Esposito, A. Biochemical resolving power of fluorescence lifetime imaging: untangling the roles of the instrument response function and photon-statistics. *Biomedical Optics Express* **12**, 3775 (2021).

[82] Wahl, M. Modern TCSPC electronics: Principles and acquisition modes. 1–21 (Springer International Publishing, 2014).

[83] Mota, M. & Christiansen, J. A high-resolution time interpolator based on a delay locked loop and an RC delay line **34**, 1360–1366 (1999).

[84] Becker, W. (ed.) *Advanced Time-Correlated Single Photon Counting Applications* (Springer International Publishing, 2015).

[85] Hirvonen, L. M. & Suhling, K. Fast timing techniques in FLIM applications **8** (2020).

[86] Garzetti, F., Corna, N., Lusardi, N. & Geraci, A. Time-to-digital converter IP-core for FPGA at state of the art **9**, 85515–85528 (2021).

[87] M. N. Cirstea, J. K., A. Dinu & McCormick, M. *Neural and Fuzzy Logic Control of Drives and Power Systems* (2002).

[88] Monmasson, E. & Cirstea, M. FPGA design methodology for industrial control systems—a review **54**, 1824–1842 (2007).

[89] Brown, S. FPGA architectural research: a survey **13**, 9–15 (1996).

[90] Grout, I. *Digital Systems Design with FPGAs and CPLDs* (2008).

[91] Trimberger, S. M. Three ages of FPGAs: A retrospective on the first thirty years of FPGA technology **103**, 318–331 (2015).

[92] Lee, D.-H., Choi, A., Koo, J.-M., Lee, J.-I. & Kim, B. M. A wideband DS-CDMA modem for a mobile station **45**, 1259–1269 (1999).

[93] Pirsch, P., Demassieux, N. & Gehrke, W. VLSI architectures for video compression-a survey **83**, 220–246 (1995).

[94] Ovaska, S. & Vainio, O. Evolutionary-programming-based optimization of reduced-rank adaptive filters for reference generation in active power filters **51**, 910–916 (2004).

[95] Chen, R.-X., Chen, L.-G. & Chen, L. System design consideration for digital wheelchair controller **47**, 898–907 (2000).

[96] Artem, P. & Dmitry, S. FPGA technologies in medical equipment: Electrical impedance tomography (IEEE, 2013).

[97] Wolf, D. F., Holanda, J. A., Bonato, V., Peron, R. & Marques, E. An FPGA-based mobile robot controller (IEEE, 2007).

[98] Moctezuma Eugenio, J. C. & Arias Estrada, M. Hardware/software fpga architecture for robotics applications. In Becker, J., Woods, R., Athanas, P. & Morgan, F. (eds.) *Reconfigurable Computing: Architectures, Tools and Applications*, 27–38 (Springer Berlin Heidelberg, Berlin, Heidelberg, 2009).

[99] Jeppesen, B. P., Roy, N., Moro, L. & Baronti, F. An FPGA-based controller for collaborative robotics (IEEE, 2017).

[100] Wan, Z. *et al.* A survey of fpga-based robotic computing (2020).

[101] Kara, K., Alistarh, D., Alonso, G., Mutlu, O. & Zhang, C. FPGA-accelerated dense linear machine learning: A precision-convergence trade-off (IEEE, 2017).

[102] Duarte, J. *et al.* FPGA-accelerated machine learning inference as a service for particle physics computing **3** (2019).

[103] Shawahna, A., Sait, S. M. & El-Maleh, A. FPGA-based accelerators of deep learning networks for learning and classification: A review **7**, 7823–7859 (2019).

[104] Kalisz, J., Szplet, R., Pasierbinski, J. & Poniecki, A. Field-programmable-gate-array-based time-to-digital converter with 200-ps resolution **46**, 51–55 (1997).

[105] Szplet, R., Kalisz, J. & Szymanowski, R. Interpolating time counter with 100 ps resolution on a single FPGA device **49**, 879–883 (2000).

[106] Song, J., An, Q. & Liu, S. A high-resolution time-to-digital converter implemented in field-programmable-gate-arrays **53**, 236–241 (2006).

[107] Franch, N. *et al.* A low cost fluorescence lifetime measurement system based on SPAD detectors and FPGA processing (IEEE, 2016).

[108] Abdelkrim, H., Othman, S. B. & Saoud, S. B. Reconfigurable SoC FPGA based: Overview and trends (IEEE, 2017).

[109] Dhote, S. *et al.* Using FPGA-SoC interface for low cost IoT based image processing (IEEE, 2016).

[110] Bravo-Muñoz, I., Gardel-Vicente, A. & Lázaro-Galilea, J. L. New applications and architectures based on FPGA/SoC **9**, 1789 (2020).

[111] Al-Mahmood, A. & Opoku, M. A study of FPGA-based system-on-chip designs for real-time industrial application **163**, 9–19 (2017).

[112] Rössler, P. & Höller, R. Programmable logic devices – key components for today's and tomorrow's electronic-based systems **137**, 45–51 (2019).

[113] Chow, P. *et al.* The design of a SRAM-based field-programmable gate array-part II: Circuit design and layout **7**, 321–330 (1999).

[114] Asadi, G. & Tahoori, M. B. Soft error rate estimation and mitigation for SRAM-based FPGAs (ACM Press, 2005).

[115] Bernardeschi, C., Cassano, L. & Domenici, A. SRAM-based FPGA systems for safety-critical applications: A survey on design standards and proposed methodologies **30**, 373–390 (2015).

[116] Kuon, I., Egier, A. & Rose, J. Design, layout and verification of an FPGA using automated tools (ACM Press, 2005).

[117] Yang, H., Zhang, J., Sun, J. & Yu, L. Review of advanced FPGA architectures and technologies **31**, 371–393 (2014).

[118] Asghar, A. *et al.* Exploring shared SRAM tables in FPGAs for larger LUTs and higher degree of sharing **2017**, 1–9 (2017).

[119] German-Sallo, Z. Signal processing using FPGA structures **12**, 112–118 (2014).

[120] Unnikrishnan, K. S. & Madhavan, S. Parallel computation using DSP slices in FPGA **24**, 1127–1134 (2016).

[121] Yang, M., Chen, L., Li, X. & Zhang, Y. A dynamically reconfigurable multi-functional PLL for SRAM-based FPGA in 65nm CMOS technology (Author(s), 2018).

[122] Chen, Z. J., Zhong, G. H. & Bi, Z. A high speed 8b/10b encoder/decoder design based on low cost FPGA **462**, 361–367 (2012).

[123] Tanabe, S., Nagashima, T. & Yamaguchi, Y. A study of an FPGA based flexible SIMD processor **39**, 86–89 (2011).

[124] kumar, D. & Ganesh, R. FPGA implementation of real time data acquisition system using micro blaze processor. **02**, 151–154 (2013).

[125] SALEM, R., SALAH, Y., BENNOUR, I. & ATRI, M. FPGA prototyping and design evaluation of a NoC-based MPSoC **8** (2017).

[126] de Fine Licht, J., Blott, M. & Hoefler, T. Designing scalable FPGA architectures using high-level synthesis (ACM, 2018).

[127] Mencer, O. *et al.* The history, status, and future of FPGAs **18**, 71–82 (2020).

[128] Pirzada, S. J. H., , Murtaza, A., Xu, T. & Jianwei, L. A reconfigurable model-based design for rapid prototyping on FPGA **12**, 80–84 (2020).

[129] Chen, P., Hsiao, Y.-Y., Chung, Y.-S., Tsai, W. X. & Lin, J.-M. A 2.5-ps bin size and 6.7-ps resolution FPGA time-to-digital converter based on delay wrapping and averaging **25**, 114–124 (2017).

[130] Wang, Y., Cao, Q. & Liu, C. A multi-chain merged tapped delay line for high precision time-to-digital converters in FPGAs **65**, 96–100 (2018).

[131] Chen, H. & Li, D. D.-U. Multichannel, low nonlinearity time-to-digital converters based on 20 and 28 nm FPGAs **66**, 3265–3274 (2019).

[132] Menninga, H., Favi, C., Fishburn, M. W. & Charbon, E. A multi-channel, 10ps resolution, FPGA-based TDC with 300ms/s throughput for open-source PET applications (IEEE, 2011).

[133] Maxfield, C. M. FPGA vs. ASIC designs. 61–73 (Elsevier, 2008).

[134] Shen, Q. *et al.* A multi-chain measurements averaging TDC implemented in a 40 nm FPGA (IEEE, 2014).

[135] Shen, Q. *et al.* A 1.7 ps equivalent bin size and 4.2 ps RMS FPGA TDC based on multichain measurements averaging method **62**, 947–954 (2015).

[136] Qin, X. *et al.* A 1.15-ps bin size and 3.5-ps single-shot precision time-to-digital converter with on-board offset correction in an FPGA **64**, 2951–2957 (2017).

[137] Liu, C., Wang, Y., Kuang, P., Li, D. & Cheng, X. A 3.9 ps RMS resolution time-to-digital converter using dual-sampling method on kintex UltraScale FPGA (IEEE, 2016).

[138] Wang, Y. & Liu, C. A 3.9 ps time-interval RMS precision time-to-digital converter using a dual-sampling method in an UltraScale FPGA **63**, 2617–2621 (2016).

[139] Wang, Y. & Liu, C. A 4.2 ps time-interval RMS resolution time-to-digital converter using a bin decimation method in an UltraScale FPGA **63**, 2632–2638 (2016).

[140] Machado, R., Cabral, J. & Alves, F. S. Recent developments and challenges in FPGA-based time-to-digital converters **68**, 4205–4221 (2019).

[141] Abbas, M. & Khalil, K. A 23ps resolution time-to-digital converter implemented on low-cost FPGA platform (IEEE, 2015).

[142] Lusardi, N. & Geraci, A. 8-channels high-resolution TDC in FPGA (IEEE, 2015).

[143] Parsakordasiabi, M., Vornicu, I., Carmona-Galán, R. & Rodríguez-Vázquez, Á. A survey on FPGA-based high-resolution TDCs (ACM, 2019).

[144] Arkani, M. A high performance digital time interval spectrometer: An embedded, FPGA-based system with reduced dead time behaviour **22**, 601–619 (2015).

[145] Guo, Q., Feng, R., Wu, Y. & Yu, N. Measurement of the AFDX switch latency based on FPGA (IEEE, 2016).

[146] Calvo, D. 1 ns time to digital converters for the KM3net data readout system (AIP Publishing LLC, 2014).

[147] Balla, A. *et al.* The characterization and application of a low resource FPGA-based time to digital converter **739**, 75–82 (2014).

[148] Grigoriev, D., Kasyanenko, P., Kravchenko, E., Shamov, A. & Talyshev, A. A 32-channel 840msps TDC based on altera cyclone III FPGA **12**, C08025–C08025 (2017).

[149] Li, Z. *et al.* Development of an integrated four-channel fast avalanche-photodiode detector system with nanosecond time resolution **870**, 43–49 (2017).

[150] Sano, Y. *et al.* Subnanosecond time-to-digital converter implemented in a kintex-7 FPGA **874**, 50–56 (2017).

[151] Yonggang, W., Xinyi, C., Deng, L., Wensong, Z. & Chong, L. A linear time-over-threshold digitizing scheme and its 64-channel DAQ prototype design on FPGA for a continuous crystal PET detector **61**, 99–106 (2014).

[152] Fan, H.-H., Cao, P., Liu, S.-B. & An, Q. TOT measurement implemented in FPGA TDC **39**, 116101 (2015).

[153] Wang, Y., Kuang, P. & Liu, C. A 256-channel multi-phase clock sampling-based time-to-digital converter implemented in a kintex-7 FPGA (IEEE, 2016).

[154] Wang, P. *et al.* Far-field imaging of non-fluorescent species with subdiffraction resolution. *Nat. Photon.* **7**, 449–453 (2013). URL http://dx.doi.org/10.1038/nphoton.2013.97.

[155] Pan, W., Gong, G., Du, Q., Li, H. & Li, J. High resolution distributed time-to-digital converter (TDC) in a white rabbit network **738**, 13–19 (2014).

[156] Aguilar, A. *et al.* Time of flight measurements based on FPGA using a breast dedicated PET **9**, C05012–C05012 (2014).

[157] Aguilar, A. *et al.* Time of flight measurements based on FPGA and SiPMs for PET–MR **734**, 127–131 (2014).

[158] Torres, J. *et al.* Time-to-digital converter based on FPGA with multiple channel capability **61**, 107–114 (2014).

[159] Nogrette, F. *et al.* Characterization of a detector chain using a FPGA-based time-to-digital converter to reconstruct the three-dimensional coordinates of single particles at high flux **86**, 113105 (2015).

[160] Szplet, R., Kwiatkowski, P., Jachna, Z. & Rozyc, K. Precise three-channel integrated time counter (IEEE, 2015).

[161] Wang, Y., Liu, C., Cheng, X. & Li, D. Spartan-6 FPGA based 8-channel time-to-digital converters for TOF-PET systems (IEEE, 2015).

[162] Narasimman, R., Prabhakar, A. & Chandrachoodan, N. Implementation of a 30 ps resolution time to digital converter in FPGA (IEEE, 2015).

[163] Aguilar, A. *et al.* Timing results using an FPGA-based TDC with large arrays of 144 SiPMs **62**, 12–18 (2015).

[164] Homulle, H., Regazzoni, F. & Charbon, E. 200 MS/s ADC implemented in a FPGA employing TDCs. In *Proceedings of the 2015 ACM/SIGDA International Symposium on Field-Programmable Gate Arrays* (ACM, 2015).

[165] Hsu, L.-Y. & Huang, J.-L. A multi-channel FPGA-based time-to-digital converter (IEEE, 2016).

[166] Burri, S., Homulle, H., Bruschini, C. & Charbon, E. LinoSPAD: a time-resolved 256×1 CMOS SPAD line sensor system featuring 64 FPGA-based TDC channels running at up to 8.5 giga-events per second (SPIE, 2016).

[167] Chaberski, D., Frankowski, R., Zieliński, M. & Zaworski, Ł. Multiple-tapped-delay-line hardware-linearisation technique based on wire load regulation **92**, 103–113 (2016).

[168] Won, J. Y. *et al.* Dual-phase tapped-delay-line time-to-digital converter with on-the-fly calibration implemented in 40 nm FPGA **10**, 231–242 (2016).

[169] Lusardi, N., Palmucci, A. & Geraci, A. Fully-migratable TDC architecture for FPGA devices (IEEE, 2016).

[170] Chen, P., Hsiao, Y.-Y. & Chung, Y.-S. A high resolution FPGA TDC converter with 2.5 ps bin size and -3.79∼6.53 LSB integral nonlinearity (IEEE, 2016).

[171] Chaberski, D. Time-to-digital-converter based on multiple-tapped-delay-line **89**, 87–96 (2016).

[172] Cao, Q., Wang, Y. & Liu, C. A combination of multiple channels of FPGA based time-to-digital converter for high time precision (IEEE, 2016).

[173] Lusardi, N., Geraci, A., Marjanovic, J. & Gustin, M. High-resolution TDL-TDC system for MTCA.4 standard (IEEE, 2016).

[174] Lusardi, N. *et al.* Single photon counting through multi-channel TDC in programmable logic (IEEE, 2016).

[175] Pałka, M. *et al.* Multichannel FPGA based MVT system for high precision time (20 ps RMS) and charge measurement **12**, P08001–P08001 (2017).

[176] Lusardi, N., Los, J. W. N., Gourgues, R. B. M., Bulgarini, G. & Geraci, A. Photon counting with photon number resolution through superconducting nanowires coupled to a multi-channel TDC in FPGA **88**, 035003 (2017).

[177] Arabul, E., Girach, A., Rarity, J. & Dahnoun, N. Precise multi-channel timing analysis system for multi-stop LIDAR correlation (IEEE, 2017).

[178] Zheng, J., Cao, P., Jiang, D. & An, Q. Low-cost FPGA TDC with high resolution and density **64**, 1401–1408 (2017).

[179] Wang, Y., Kuang, J., Liu, C., Cao, Q. & Li, D. A flexible 32-channel time-to-digital converter implemented in a xilinx zynq-7000 field programmable gate array **847**, 61–66 (2017).

[180] Wang, Y., Kuang, J., Liu, C. & Cao, Q. A 3.9-ps RMS precision time-to-digital converter using ones-counter encoding scheme in a kintex-7 FPGA **64**, 2713–2718 (2017).

[181] Chen, H., Zhang, Y. & Li, D. D.-U. A low nonlinearity, missing-code free time-to-digital converter based on 28-nm FPGAs with embedded bin-width calibrations **66**, 1912–1921 (2017).

[182] Dinh, V. L., Nguyen, X. T. & Lee, H.-J. A new FPGA implementation of a time-to-digital converter supporting run-time estimation of operating condition variation (IEEE, 2018).

[183] Cao, G., Xia, H. & Dong, N. An 18-ps TDC using timing adjustment and bin realignment methods in a cyclone-IV FPGA **89**, 054707 (2018).

[184] Arabul, E., Rarity, J. & Dahnoun, N. FPGA based fast integrated real-time multi coincidence counter using a time-to-digital converter (IEEE, 2018).

[185] Tontini, A., Gasparini, L., Pancheri, L. & Passerone, R. Design and characterization of a low-cost FPGA-based TDC **65**, 680–690 (2018).

[186] Klär, H., Schulz, M., Steffen, P. & Düllmann, D. The flash-TDC. *Nuclear Instruments and Methods in Physics Research Section A: Accelerators, Spectrometers, Detectors and Associated Equipment* **275**, 197–198 (1989).

[187] Parsakordasiabi, M., Vornicu, I., Rodríguez-Vázquez, Á. & Carmona-Galán, R. A low-resources TDC for multi-channel direct ToF readout based on a 28-nm FPGA. *Sensors* **21**, 308 (2021).

[188] Favi, C. & Charbon, E. A 17ps time-to-digital converter implemented in 65nm FPGA technology. In *Proceeding of the ACM/SIGDA international symposium on Field programmable gate arrays - FPGA '09* (ACM Press, 2009).

[189] Wu, J. Several key issues on implementing delay line based TDCs using FPGAs. *IEEE Transactions on Nuclear Science* **57**, 1543–1548 (2010).

[190] Shen, Q. *et al.* A fast improved fat tree encoder for wave union TDC in an FPGA **37**, 106102 (2013).

[191] Jaworski, Z. Verilog HDL model based thermometer-to-binary encoder with bubble error correction (IEEE, 2016).

[192] Wu, J. & Shi, Z. The 10-ps wave union TDC: Improving FPGA TDC resolution beyond its cell delay. In *2008 IEEE Nuclear Science Symposium Conference Record* (IEEE, 2008).

[193] Bayer, E. & Traxler, M. A high-resolution (<10ps rms) 48-channel time-to-digital converter (tdc) implemented in a field programmable gate array (fpga). *IEEE Transactions on Nuclear Science* **58**, 1547–1552 (2011).

[194] Machado, R., Rocha, L. A. & Cabral, J. A novel synchronizer for a 17.9ps nutt time-to-digital converter implemented on FPGA (IEEE, 2018).

[195] Wu, J. *et al.* A hybrid time-to-digital converter based on sliding scale technique suitable for random time-of-flight measurement **99**, 277–285 (2018).

[196] Tancock, S., Arabul, E. & Dahnoun, N. A review of new time-to-digital conversion techniques. *IEEE Transactions on Instrumentation and Measurement* **68**, 3406–3417 (2019).

[197] Sall, E. & Vesterbacka, M. Comparison of two thermometer-to-binary decoders for high-performance flash ADCs (IEEE, 2005).

[198] Sall, E. & Vesterbacka, M. Thermometer-to-binary decoders for flash analog-to-digital converters (IEEE, 2007).

[199] Ajanya, M. & Varghese, G. T. Thermometer code to binary code converter for flash ADC - a review (IEEE, 2018).

[200] Kuang, J., Wang, Y., Cao, Q. & Liu, C. Implementation of a high precision multi-measurement time-to-digital convertor on a kintex-7 FPGA **891**, 37–41 (2018).

[201] Cui, K., Li, X., Liu, Z. & Zhu, R. Toward implementing multichannels, ring-oscillator-based, vernier time-to-digital converter in FPGAs: Key design points and construction method **1**, 391–399 (2017).

[202] Szplet, R., Kwiatkowski, P., Jachna, Z. & Rozyc, K. An eight-channel 4.5-ps precision timestamps-based time interval counter in FPGA chip **65**, 2088–2100 (2016).

[203] Liu, C. & Wang, Y. A 128-channel, 710 m samples/second, and less than 10 ps RMS resolution time-to-digital converter implemented in a kintex-7 FPGA. *IEEE Transactions on Nuclear Science* **62**, 773–783 (2015).

[204] Carra, P. *et al.* Auto-calibrating TDC for an SoC-FPGA data acquisition system. *IEEE Transactions on Radiation and Plasma Medical Sciences* **3**, 549–556 (2019).

[205] Liu, M. *et al.* Instrument response standard in time-resolved fluorescence spectroscopy at visible wavelength: Quenched fluorescein sodium. *Applied Spectroscopy* **68**, 577–583 (2014).

[206] Slenders, E. *et al.* Confocal-based fluorescence fluctuation spectroscopy with a SPAD array detector. *Light Sci. Appl.* **10** (2021).

[207] Koho, S. V. *et al.* Two-photon image-scanning microscopy with SPAD array and blind image reconstruction. *Biomed. Opt. Express* **11**, 2905 (2020).

[208] Gao, D. *et al.* FLIMJ: An open-source ImageJ toolkit for fluorescence lifetime image data analysis. *PLOS One* **15**, e0238327 (2020).

[209] Ranjit, S., Malacrida, L., Jameson, D. M. & Gratton, E. Fit-free analysis of fluorescence lifetime imaging data using the phasor approach. *Nature Protocols* **13**, 1979–2004 (2018).

[210] Owen, D. M. *et al.* Fluorescence lifetime imaging provides enhanced contrast when imaging the phase-sensitive dye di-4-ANEPPDHQ in model membranes and live cells. *Biophys. J.* **90**, L80–L82 (2006).

[211] Sekar, R. B. & Periasamy, A. Fluorescence resonance energy transfer (FRET) microscopy imaging of live cell protein localizations. *Journal of Cell Biology* **160**, 629–633 (2003).

[212] Ouyang, Y., Liu, Y., Wang, Z. M., Liu, Z. & Wu, M. FLIM as a promising tool for cancer diagnosis and treatment monitoring **13** (2021).

[213] Tenne, R. *et al.* Super-resolution enhancement by quantum image scanning microscopy. *Nat. Photonics* **13**, 116–122 (2018).

[214] Lubin, G. *et al.* Quantum correlation measurement with single photon avalanche diode arrays. *Optics Express* **27**, 32863 (2019).

[215] Villa, F. *et al.* CMOS SPADs with up to 500 μm diameter and 55% detection efficiency at 420 nm. *Journal of Modern Optics* **61**, 102–115 (2014).

Appendix A

Assessing the performances of a TDC

TDCs are used to measure time intervals and pure FPGA-based TDC research contributions mainly focused on increasing TDC time-resolution. Despite resolution is an important parameter to take into account, the TDC non-linearities have also to be improved as they will directly affect the overall measurement precision. Thus, when dealing with FPGA-based TDC architectures it is importat to look after not only the time-resolution but also TDC linear response.

Statistical code density test

In this supplementary section, we explain the statistical code density test used to characterize the linearity of the BrightEyes-TTM. The code density test allows measuring (i) the time response of each time-bin of the TDC and (ii) the deviation of TTM measurement readouts from the actual time of arrival of a photon. One of the most important parameters to analyse in order to asses the system response of a time-tagging device is the system linearity. A statistical code density test consist of feeding the TTM random (uncorrelated) photons with respect to the sync reference signal. Here, we generated random photons by connecting an avalanche photodiode (APD) to the TTM (Fig 5.1). After having reconstructed the histogram $H_{(i)}$ of the collected random events (using bin-by-bin auto-calibrated data), $H_{(i)}$ histogram data was used to compute two benchmark indicators of a system's linearity: the differential non-linearity (DNL) and the integral non-linearity (INL) (Fig. 5.3 & Fig. 5.4). The DNL and INL may seem counter-intuitive indices as the DNL describes the non-linearity amongst the different time-bins of $H_{(i)}$ (i.e., how much all the bin widths in the temporal range differ from each other) and the INL to what extent the system is non-linear (i.e., to what extent the system is capable of precisely measuring time with respect to an ideal time-tagging

device). The relevant values are the standard deviations of the DNL and INL, which are expressed in LSB. In agreement with the Xilinx Kintex-7 XC7K325T-2FFG900C datasheet and with measurement findings (Chapter 5.6), an LSB of 43 ps, corresponding to the time delay associated with the coarseness of the CARRY4 element (employed as the fundamental unit in the flash TDC module) was used to reconstruct $H_{(i)}$ and compute σ_{DNL} and σ_{INL} (215).

Differential non-linearity - DNL

When performing a statistical code density test, the reconstructed time histogram $H_{(i)}$ should ideally be a constant flat line, indicating that every time-bin has an equal time-width within the measured temporal range. In reality, due to intrinsic FPGA fabric inconsistencies, $H_{(i)}$ shows a ripple that needs to be characterised in order to maximise the timing precision and accuracy. The aim of computing the DNL is to understand to which degree the difference in time widths of all the possible time bins (which is the cause of the ripple) deviates from a common average value. In other words, the DNL is used to understand the relative contribution of all the time bins when reconstructing times of arrival of photons in the TDC temporal range. The DNL is calculated according to Eq. A.1:

$$DNL_{(i)} = \frac{H_{(i)} - H_{\mathrm{avg}}}{H_{\mathrm{avg}}} \tag{A.1}$$

Here, $H_{(i)}$ is the reconstructed histogram of the dark counts and H_{avg} its average value. $DNL_{(i)}$ represents the deviation of the i-th time bin from the H_{avg} value: the lower this deviation, the flatter the $DNL_{(i)}$ plot will be. If the DNL is constant, all time-bins have the same width and the system is perfectly linear.

Integral non-linearity - INL

The INL is used to determine to which degree the response of a time-tagging system differs from the ideal linear behaviour. The INL gives an estimate of the difference between a TTM measurement and the actual time of arrival of a photon. If the TTM is linear, the INL should hold constant around the zero.

The $INL_{(i)}$ is computed as the cumulative sum of all the $\mathrm{DNL}_{(i)}$ contributions, Eq. A.2:

$$INL_{(i)} = \sum_{k=1}^{i} DNL_{(i)} \tag{A.2}$$

Single shot precision

Single-shot precision (SSP) of a TDC is defined as the standard deviation of the distribution of the measurement results around the mean value, when a constant time interval (start-stop time interval) is measured repeatedly. In a SSP experiment, a fixed time delay between the SYNC signal, and a synchronised second signal, that mimics a photon signal, is measured multiple times. Then, the measurement is repeated for all possible imposed delay values within the repetition rate of the SYNC signal. For each imposed delay value, the TTM collects several millions of sync-photon pairs (start-stop time), and builds up the start-stop time histograms (TCSPC histograms). Each single histogram is fitted with a normal (Gaussian) distribution, Eq. A.3:

$$H_{(t)} = A \exp\{-((t-\mu)/\sigma)^2/2\} \tag{A.3}$$

Being $H_{(t)}$ the fitting result, the mean μ and the standard deviation σ values can be extrapolated. σ is used as SSP measurement.

Appendix B

Simulate your own laser and photons - Sylap

In order to perform the testbench measurements and thus accomplish the code-density-test, DNL & INL assessment and to compute SSP over the temporal range and for all the deployed channels toghether with the dual channel SSP, a specific FPGA firmware that allows to 'simulate your own laser and photons' (SYLAP) component was developed by IIT - Molecular Microscopy and Spectroscopy lab for this specific project.

SYLAP was implemented on an FPGA-evaluation board identical to the one used for the BrigthEyes-TTM (i.e., KC705 Evaluation Board, Xilinx). The SYLAP architecture generates a fixed frequency clock, which was used to simulated the laser SYNC signal, and a synchronised pulse train, which was used to mimic the photon signals. Key features of the SYLAP are (i) the possibility to adjust the delay from the clock and the pulse with a granularity of 39.0625 ps; (ii) the possibility to set the clock period and the pulse duration with a granularity of 2.5 ns. The native USB 2.0 serial port (UART port) of the evaluation board allows configuring the SYLAP. The timing jitter between the clock and the pulse is 13 ps, measured with Keysight DSO9404A 4 GHz bandwidth oscilloscope.

Since both the BrightEyes-TTM and the SYLAP signal generator use the same type of board, both systems were deployed on the very same FPGA board. For more information on the SYLAP firmware and its implementation refer to https://github.com/VicidominiLab/SYLAP.

Appendix C

Sample preparation

TTM characterisation and validation

For TTM characterisation and validation, Fluorescein (46955, free acid, Sigma-Aldrich) and potassium iodide (60399-100G-F, BioUltra, >= 99.5% (AT), Sigma-Aldrich) was used. The Fluorescein was dissolved from powder into DMSO and then we further diluted to a 1:1000 v/ concentration by adding ultrapure water. For the Fluorescein quenching experiments, the 1:1000 Fluorescein solution was diluted at different ratio with the potassium iodide (KI) quencher (from 1:2 to 1:256). All samples were made at room temperature. A fresh sample solution was prepared for each measurement.

Imaging and FLIM experiments

Fluorescent nanobeads

For imaging experiments a sample of 100 nm fluorescent beads (yellow-green FluoSpheres Q7 Carboxylate-Modified Microspheres, F8803; Invitrogen) was used. The glass coverslips were treated with poly-L-lysine (P8920; Sigma-Aldrich) for 20 min at room temperature, and then the beads were diluted in Milli-Q water by 1:10,000 v/v. The beads were drop-casted onto the coverslips, and, after 10 min, the coverslips were washed with Milli-Q water and dried under nitrogen flow; overnight the slides were mounted with Invitrogen ProLong Diamond Antifade Mounting Medium (P36965);

Fixed mammalian cells

An already prepared microscope slide (IG-4011 Imaging Set, Abberior) containing fixed mammalian cells was used. The vimentin within the cells was stained with the STAR-GREEN dye.

HeLa cells

A fresh prepared microscope slide containing fixed HeLa cells stained for α-tubulin was used. HeLa cells were cultured in Dulbecco's Modified Eagle Medium (DMEM, Gibco, ThermoFisher Scientific, Wilmington) supplemented with 10% fetal bovine serum (Sigma-Aldrich) and 1% penicillin/streptomycin (Sigma-Aldrich) at 37 °C in 5% CO2. One day before immunostaining, HeLa cells were seeded onto coverslips in a 12-well plate (Corning Inc., Corning, NY) and incubated in a solution of 0.3% Triton X-100 (Sigma-Aldrich) and 0.1% glutaraldehyde (Sigma-Aldrich) in the BRB80 buffer (80 mM Pipes, 1 mM EGTA, 4 mM MgCl, pH 6.8, Sigma-Aldrich) for 1 min. Then, HeLa cells were fixed with a solution of 4% paraformaldehyde (Sigma-Aldrich) and 4% sucrose (Sigma-Aldrich) in the BRB80 buffer for 10 min and washed three times for 15 min in phosphate-buffered saline (PBS, Gibco™, ThermoFisher). Next, the cells were treated with a solution of 0.25% Triton-X100 in the blocking buffer for 10 min and washed three times for 15 min in PBS. After 1 h in blocking buffer (3% bovine serum albumin (BSA, Sigma-Aldrich) in BRB80 buffer), the cells were incubated with monoclonal mouse anti-α-tubulin antibody (Sigma-Aldrich) diluted in the blocking buffer for 1 h at room temperature. The alpha-tubulin goat anti-mouse antibody was revealed by Alexa Fluor 488 goat anti-mouse (Invitrogen, ThermoFisher Scientific) incubated for 1 h in BRB80 buffer. HeLa cells were then rinsed three times in PBS for 15 min. Finally, the cover slips were mounted onto microscope slides (Avantor, VWR International) with ProLong Diamond Antifade Mountant (Invitrogen, ThermoFisher Scientific).

CellBrite™Green Cytoplasmic Membrane Dye

Live HeLa cells stained for CellBrite™Green Cytoplasmic Membrane Dye (Biotium Inc., Fremont, CA) were imaged. One day before live cell imaging, HeLa cells were seeded onto a μ-Slide 8 plate (Ibidi, Grafelfing, Germany). The day after, cells were labeled with CellBrite™Green Cytoplasmic Membrane Dye according to manufacturer's protocol. Measurements were performed in Live Cell Imaging Solution (Thermo Fisher Scientific) at RT.

di-4-ANEPPDHQ

Live HeLa cells stained for di-4-ANEPPDHQ. One day before live cell imaging, HeLa cells were seeded onto a μ-Slide 8 plate (Ibidi). The day after, cells were incubated with DMEM (Gibco, Thermo Fisher Scientific) supplemented with 5 μ-uM di-4-ANEPPDHQ (Invitrogen, ThermoFisher Scientific) at 37 °C in 5% CO2 for 30 min. Cells were washed three times with DMEM. Measurements were performed in Live Cell Imaging Solution (Thermo Fisher Scientific) at RT.

Appendix D

Nomenclature table

Table D.1 **Nomenclature A**

$\Delta T_{\text{START}}(ch)$	integer value representing the number of tapped-delays (in the START tapped-delay line) that the START signal, i.e., the photon signal, already travel through before the arrival of the FPGA clock signal. When reported, *ch* denotes the photon channel.
$\Delta t_{\text{START}}(ch)$	calibrated temporal value representing the time elapsed from the START signal, i.e., the photon signal, and the next active edge of the free-running coarse counter (FPGA clock). When reported, *ch* denotes the photon channel.
ΔT_{STOP}	integer value representing the number of tapped-delays (in the STOP tapped-delay line) that the STOP signal, i.e., the laser SYNC signal, already travel through before the arrival of the FPGA clock signal.
Δt_{STOP}	calibrated temporal value representing the time elapsed from the STOP signal, i.e., the laser SYNC signal, and the next active edge of the free-running coarse counter (FPGA clock).
$\Delta t(ch)$	photon start-stop time, i.e., the photon arrival-time in reference to the excitation event. When reported, *ch* denotes the photon channel.
$\hat{t}_{\text{photon}}(ch)$	photon-arrival time with respect to the beginning of the experiment measured with nanosecond precision (by using only the free-running course counter). When reported, *ch* denotes the photon channel.
$\hat{t}_{\text{SYNC}}(ch)$	SYNC-arrival time with respect to the beginning of the experiment measured with nanosecond precision (by using only the free-running course counter).
$\hat{t}_{\text{REF}}(l)$	REF-arrival time with respect to the beginning of the experiment measured with nanosecond precision (by using only the free-running course counter).

Table D.2 **Nomenclature B**

$\Delta\hat{t}^{\,\text{photon}}_{\text{REF}_l}(ch)$	photon-arrival time with respect to the l-th reference event measured with nanosecond precision (by using only the free-running course counter). When reported, *ch* denotes the photon channel.
$n_{\text{photon}}(ch)$	the number of FPGA clock cycle between the beginning of the experiment and the photon signal. When reported, *ch* denotes the photon channel.
n_{SYNC}	the number of FPGA clock cycle between the beginning of the experiment and the laser SYNC signal.
n_{REF_l}	the number of FPGA clock cycle between the beginning of the experiment and the l-th reference signal.
$\Delta n(ch)$	the number of elapsed FPGA clock cycle from the START photon event and the relative STOP laser SYNC event. When reported, *ch* denotes the photon channel.
$\mathscr{T}_{\text{sysclk}}$	the period of the FPGA system clock.
f_{sysclk}	frequency of the FPGA system clock.
$t_{\text{photon}}(ch)$	absolute time from the beginning of the experiment for the photon signal with, in principle, picosecond precision.
t_{SYNC}	absolute time from the beginning of the experiment for the SYNC signal with, in principle, picosecond precision.
(x,y,z)	spatial coordinate for the scanning system.
fr	frame.
τ_{fl}	fluorescence excited-state lifetime, i.e., average time that a fluorophore spend in the excited state. Assuming a single exponential decay it represent the inverse of the decay rate.
$\mathscr{T}$	the period of the pulsed excitation laser.
f	the frequency of the pulsed excitation laser.